2018

CHARACTERIZATION OF ROTARY BELL ATOMIZERS THROUGH IMAGE ANALYSIS TECHNIQUES

Jacob E. Wilson
University of Kentucky, jwilson.0411@gmail.com
Author ORCID Identifier:
https://orcid.org/0000-0002-0143-6995
Digital Object Identifier: https://doi.org/10.13023/ETD.2018.205

Right click to open a feedback form in a new tab to let us know how this document benefits you.

CHARACTERIZATION OF ROTARY BELL ATOMIZERS THROUGH IMAGE
ANALYSIS TECHNIQUES

_____

THESIS

_____

A thesis submitted in partial fulfillment of the requirements for the degree of Master of
Science in Mechanical Engineering in the College of Engineering at the University of
Kentucky

By

Jacob Edward Wilson

Lexington, Kentucky

Director: Dr. Michael Renfro, Professor of Mechanical Engineering

Lexington, KY

2018

ABSTRACT OF THESIS

CHARACTERIZATION OF ROTARY BELL ATOMIZERS THROUGH IMAGE ANALYSIS TECHNIQUES

Three methods were developed to better understand and characterize the near-field dynamic processes of rotary bell atomization. The methods were developed with the goal of possible integration into industry to identify equipment changes through changes in the primary atomization of the bell. The first technique utilized high-speed imaging to capture qualitative ligament breakup and, in combination with a developed image processing technique and PIV software, was able to gain statistical size and velocity information about both ligaments and droplets in the image data. A second technique, using an Nd:YAG laser with an optical filter, was used to capture size statistics at even higher rotational speeds than the first technique, and was utilized to find differences between serrated and unserrated bell ligament and droplet data. The final technique was incorporating proper orthogonal decomposition (POD) into image data of a side-profile view of a damaged and undamaged bell during operation. This was done to capture differences between the data sets to come up with a characterization for identifying if a bell is damaged or not for future industrial integration.

KEYWORDS: rotary bell atomization; high-speed imaging; shadowgraphy; serrations; proper orthogonal decomposition;

Jacob Edward Wilson

Signature

April 25, 2018

Date

CHARACTERIZATION OF ROTARY BELL ATOMIZERS THROUGH IMAGE ANALYSIS TECHNIQUES

By

Jacob Edward Wilson

Michael Renfro
Director of Thesis

Haluk Karaca
Director of Graduate Studies

April 25, 2018
Date

ACKNOWLEDGEMENTS

The following thesis was an individual work, but could not have been completed without the varying and unique contributions of family, friends, colleagues, and mentors. I would first like to thank my family for their unconditional love and support over the course of this project and for everything that they have done for me during all of my time preceding this project. I have truly been fortunate to have been born from and lived under two amazing human beings and great parents.

Next, I would like to thank all of the friends that supported me along the way. The experiences and conversations that we have shared and their continued friendship has greatly improved my well-being and taught me a great many things about a wide variety of topics. I can only hope that I was able to provide some of the same for them in return.

Additionally, I would like to thank my colleagues. To those I had small collaborations with, or shared classes with, I wish to thank you for your help in further understanding some of the more challenging aspects of the mechanical engineering discipline and easing the burden that often accompanies performing repeated complex problem solving by yourself. To my lab mates, I extend thanks for all of the aid in experimentation and development of a variety of engineering skills that will serve me well in the future. I also thank you for the many fun experiences and fond memories.

I would like to thank my mentors. Along the way, I have had many professors, I thank you all for both the knowledge of the content, and how to apply it, that you provided me. To my co-advisor, Dr. Ahmad Salaimeh, I thank you for all of the guidance, encouragement, and for all of the opportunities that you introduced to me. Lastly, thank you to my primary advisor, Dr. Michael Renfro. You gave me the opportunity to begin the work for this thesis, provided resources, funding, guidance and presented new modes of thinking that helped to expand the ways that I approach engineering problems.

TABLE OF CONTENTS

LIST OF TABLES

LIST OF FIGURES

CHAPTER ONE: STUDY OF NEAR-CUP WATER DROPLET BREAKUP OF A

ROTARY BELL ATOMIZER USING HIGH-SPEED SHADOWGRAPH IMAGING

1.1 Introduction

Rotary bell applicators (see Fig. 1.1 for an example) are one class of spray atomizers that use centrifugal forces to break up fluid closer to the cup. This system is used in various applications such as coating applicators, fuel injectors, mass spectroscopy, drug delivery, and pesticide application[1,2]. However, one challenging application is in automotive painting due to the production rate, size of the vehicle, environmental impact, fluid properties and the importance of uniformity on the appearance and finish of the vehicle[3,4]. Rotary bell (or cup) applicators operate by releasing fluid along the center of a rotating cup, which forms a thin liquid film over the inner surface of the cup. When the film reaches the edge of the cup, ligaments (connected liquid threads) are formed. Air flow around the outside of the cup, referred to as shaping air, contributes to additional liquid breakup into droplets and directs the droplets towards the target, thus resulting in the application of the fluid to a substrate. In the automotive industry, the paint is often electrostatically charged to enhance the transfer of the paint to the target[3,5].
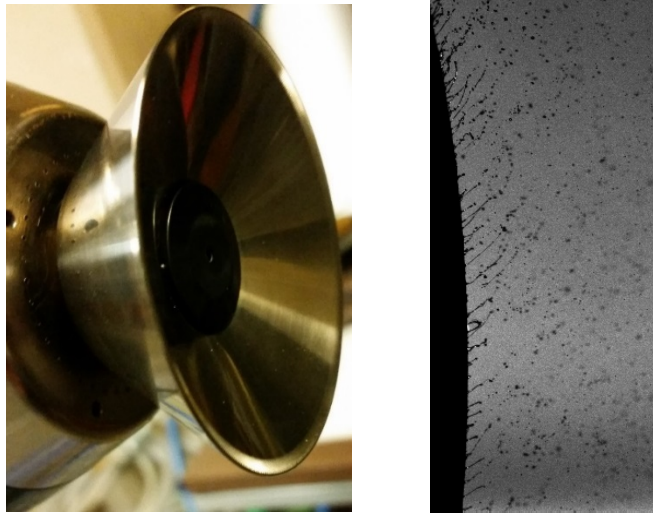
Figure 1.1. Photograph of the bell-cup of a Dürr EcoBellv2 rotary bell atomizer (left) and a shadowgraph image of the bell during operation (right), showing ligaments undergoing primary atomization into droplets.

Rotary bell atomizers have been the primary method of paint application for many manufacturers due to the increased paint transfer efficiency over the alternative of air spray guns, such as air blast sprayers. However, the devices leave room for improvement since over-coating is often necessary to ensure sufficient finish quality[5,6]. Since its inception into the industry, rotating disk, and later rotary bell, applicators have been studied in an attempt to understand and improve the paint application process, but further improvements would continue to reduce costs and waste in industrial processes. Currently, automotive paint shops amount to 30%-50% of the total cost to manufacture automobiles and up to 70% of the total energy costs in an assembly plant[3,5]. Thus, even small improvements to any aspect of the process are important, since it can result in large cost savings and waste reduction.

One of the most often-studied aspects of the rotary bell and rotating disk applicators has been the atomization process. Early studies led to the fundamental physical interpretation of liquid atomization in these systems[7–10], where it was found that the atomization process begins with thin ligaments forming at the edge of the bell that eventually breakup into droplets. Particle size distributions for droplets were also found to be Gaussian with a slight skew toward smaller sizes. Liquid breakup from the ligaments has also been described, including the laminar breakup of single jet ligament length[11], jet breakup time characterization[12], and liquid ligament detachment/elongation characterization[13].

Spinning disk applicators have similar flowfield characteristics as the bell spray process, clearly showing the ligament and droplet formation. Many studies have been conducted with regards to the critical parameters and characteristics of spinning disk and wheel applications, such as ligament and droplet formation and droplet size distributions[14–19]. One notable observations from spinning disk literature is that the Sauter mean diameter increases with decreased rotational speed[15]. Sauter mean diameter, for context, refers to the theoretical droplet diameter of a perfectly homogeneous spray having the same surface area and volume as the actual heterogeneous spray the parameter is applied to[20], and is defined as:

$$D_{32} = \frac{\sum nD^3}{\sum nD^2} \qquad\qquad (1)$$

where n is the frequency of occurrence of a global diameter D. Another notable observation is that velocity slip of the liquid film flowing over a rotating wheel is

significant when the wheel rotation is slow but is negligible at high Weber numbers[17]. Weber number, for context, is a non-dimensional number that represents the ratio between the inertial and surface tension forces in a system. Additionally, spinning disks with teeth or serrations[18] had a characteristic bimodal droplet size distribution, which was notably different from the typical polydispersed distribution for flat-rimmed rotating atomizers[15].

Many studies have been performed to characterize the effects of various parameter changes on atomization, including flowrate, rotational speed, and cup geometry with regards to bell atomizers[21]. Experimental[6,16] and simulated parametrization[22] have both been conducted which found that increasing the flowrate of rotary atomizers leads to a transition from aerodynamic (or jet) disintegration to turbulent disintegration of the ligaments, whereby there is a transition of ligament formation to sheet formation at the cup edge[4,23]. Increasing rotational speed was observed to result in less homogeneous break up[4]. Additionally, the droplet size distribution near the cup showed multi-modal shapes at low rotational speeds with[6] and without[23] electrostatic forces being included. It has been suggested that the spray is dominated by main and satellite drop sizes, corresponding to the peaks in the number distributions. Such bimodal distributions affect the final appearance[24] of the paint coating and the transfer efficiency[3]. The bimodal distributions have been shown to converge to a single mode with increasing rotational speed as well.

There have also been varieties of techniques used in imaging and determining droplet sizes for general sprays. Laser diffraction (LD) is the most common form of droplet sizing in sprays[25]. The method quantifies the droplet size distribution over a wide range

4

through the spray flowfield (plume). Though it does not give other flow properties such as velocity, other methods such as Phase Doppler Anemometry (PDA) and Phase-Doppler Particle Analyzer (PDPA) systems overcame that flaw, and they give properties such as droplet-size distribution, velocity, density and mass flux[15]. Another viable imaging technique is shadowgraph imaging, where captured images require further processing to determine the sizes of droplets and ligaments[26–28], but provide accurate statistics after calibration.

In addition to droplet and ligament size information, velocities of the fluid particles are of particular interest in understanding the transfer of the droplet cloud to the substrate. Particle image velocimetry (PIV) is a technique which can be used to determine velocity fields and has been investigated in previous spray studies to measure the velocity of flow fields and individual droplet velocities[29,30]. However, this technique does require two consecutive frames in time so that the particles can be correlated to produce the velocity vectors. This can be done through laser-pulse imaging and with high-speed cameras.

It is worth noting that PIV and micro-PIV have been used in rotary bell atomization to measure the shaping air velocity and the droplet velocity in the flow field[31–34]. To our knowledge, there are no archival articles that reported the near cup droplet and ligament velocities using PIV methods. Thus, measured velocity statistics could provide meaningful new data. PIV in conjunction with particle tracking velocimetry (PTV) was used in the present work, with a high-speed camera, to calculate the near-cup ligament and droplet velocities.

Direct droplet and ligament formation, as well as droplet sizing, have been investigated in various capacities for rotary bell applicators. However, these studies were

not conducted with the inclusion of shaping airflow[23,24,35,36], which is used in the automotive industry for paint application. While general research into pulsed airflow breakup effects[37] and specific study of rotary bell atomization characteristics with shaping air[38] have been conducted, the combination of studying droplet and ligament size evolution with changing parameters in the near field has not been reported. Additionally, many studies examine the atomization process with the inclusion of electrostatic forces[7,39], which show droplet size distributions are bimodal.

The experiments reported in this thesis examine a rotary bell applicator near the cup with shaping air using a high-speed shadowgraph imaging setup. While the technique itself has been used, its use for near-field imaging of rotary bell applicators to capture fluid particle size and simultaneous velocity measurements has not been reported in the literature. The purpose of this work was to develop an imaging technique that could examine the physical breakup mechanisms at high rotational speeds, gain meaningful size and velocity statistics, and correlate the size and velocity data from individual fluid particles, all from a single data set. This was accomplished by utilizing high-speed shadowgraph imaging and several image processing techniques to eliminate some of the inherent background noise that accompanies this type of atomization. Ultimately, this work adds valuable insight into the study of the atomization process and aids in increasing paint transfer efficiency by demonstrating a new measurement technique for studying near-field atomization and presenting meaningful fluid particle data by using this technique.

1.2 Materials and Methods

1.2.1 Experimental Setup
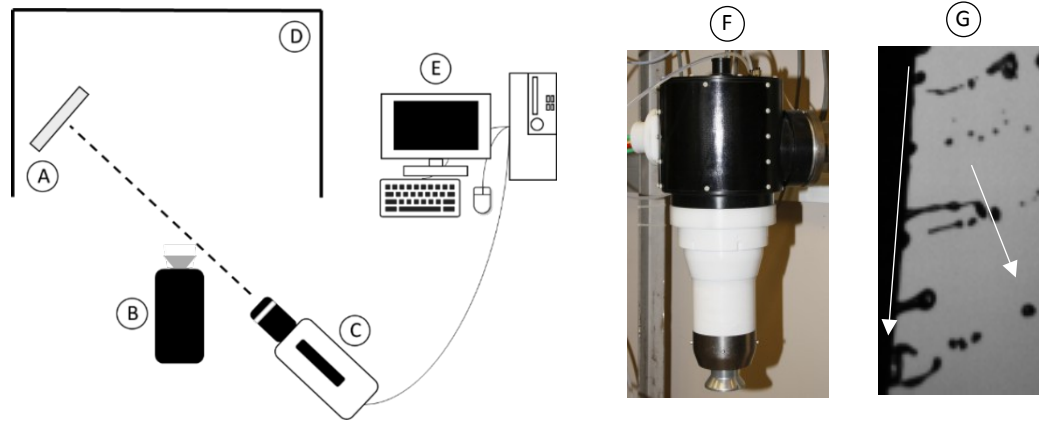
Figure 1.2. Experimental diagram (left) with lamp (A), rotary bell (B), camera (C), hood (D) and computer (E). Also pictured are the rotary bell (F) and an experimental image (G) with direction of cup rotation (left arrow) and the general fluid flow direction (right arrow) indicated.

An ASEA Brown Boveri Ltd. (ABB) rotary bell atomizer, seen in Fig. 1.2, equipped with a 65 mm diameter serrated bell-cup was used in this experiment. The rotary bell was operated at speeds of 5,000 to 12,000 RPM in intervals of 1,000 RPM. Only rotational speed was varied in this experiment due it being the dominant parameter in producing different droplet diameters for rotary bell atomizers utilizing water at the speeds conducted here[10]. Additionally, in other experimental data that can be found in Chapter 2 of this thesis in Table 2.2, which was conducted at higher rotational speeds and with multiple flowrates considered, a 96% dependence of droplet diameter on rotational speed was found with a two-way ANOVA analysis. Given these results, significant changes were only expected to be seen with variation in rotational rate.

Liquid water (paint surrogate) was used as the atomization fluid and was supplied to the bell at a flowrate of 250 ccm. The water released from the bell was contained within a

side-draft paint booth. The use of water, instead of paint, still allows for results that are

relevant for automotive paint spray systems due to the similarity in typical dimensionless

numbers used in studying droplet dynamics, seen in Table 1.1.

Table 1.1. Properties of water at parameters tested in this experiment with properties of paint at parameters used in the automotive industry. Dimensionless parameters associated with fluid breakup given in ranges based on those properties.

Property (Units)	Variable	Water		Paint	
Density (kg/m^3)	ρ	1000		1222	
Frequency (1/s)	f_0	83.33	200.0	333.3	1333
Velocity (m/s)	V	1.354	3.250	2.500	10.00
Length (m)	R	0.0650		0.0150	0.0400
Surface Tension (N/m)	σ	0.0728		0.0640	
Dynamic Viscosity (kg/(m·s))	μ	0.0089		0.1000	
Dimensionless Parameter	**Equation**	**Range**		**Range**	
Reynolds Number	$\dfrac{\rho V R}{\mu}$	4.95×10^3	1.19×10^4	4.58×10^2	4.89×10^3
Weber Number	$\dfrac{\rho(2\pi f_0)^2 R^3}{\sigma}$	1.62×10^4	9.31×10^4	3.53×10^4	1.07×10^7
Ohnesorge Number	$\dfrac{\sqrt{We}}{Re}$	2.57×10^{-2}	2.57×10^{-2}	4.10×10^{-1}	6.70×10^{-1}
Ekman Number	$\dfrac{\mu}{2\pi f_0 \rho R^2}$	6.71×10^{-6}	1.61×10^{-5}	6.11×10^{-6}	1.74×10^{-4}

Table 1.1 shows the typical physical properties of water at room temperature and

those of a glycerol-water mixture [40] meant to represent a water-borne paint mixture.

The velocities and frequencies (or rotational rates) depicted in the table represent those

used in the experiment, for water, and those for the automotive industry, for the paint.

The resulting dimensionless parameters from the given properties are also given, along

with their definitions. In jet breakup of liquid filaments, surface tension is considered a

promoting force, while inertial and viscous forces act as impeding forces. Likewise, these

forces are important in the breakup of liquid films, like a rotary atomizer. Thus, the

Reynolds (which relates inertial force to viscous force), Weber (which relates inertial

force to surface tension force), Ohnesorge (which relates viscous force to surface tension force), and Ekman (which relates viscous force to Coriolis force) numbers were calculated, using the equations provided by Bizjan et al.[17], to ensure similarity between systems. As can be seen from the dimensionless number ranges, there is overlap between the Weber number ranges, and similarity in the other number ranges, for the operational parameters used in this experiment with water, and those used for a waterborne paint at industrial rotational speeds. One way to close the gap in the other dimensionless parameters would be to increase the rotational speed of the bell in the experiment. This proved difficult to accomplish, given the tradeoff between pixel resolution and frame acquisition rate in the optical setup of this experiment. In summary, the automotive industry operates at very high rotational speeds (20-80kRPM), and with paint at viscosities higher than that of water at the rotational speeds used. This is proportionally compensated for in this experiment with the choice of reduced rotational speeds on the same order as the reduction in viscosity. More specifically, this experiment was meant to simulate a range of paint atomization of low rotational speeds and small diameter cups that often accompany clear coat application, which have a smaller bell diameter (30 – 40mm) and operate at lower rotational speeds (20-30kRPM).

A 500 W lamp was used as the illumination source for shadowgraph imaging. A Phantom V611 CMOS camera equipped with an f = 105 mm Sigma lens was used to image the liquid. The illumination source and the camera were placed on opposing sides (transmission mode) of the rotary bell as shown in Fig. 1.2. The acquisition rate of the camera was set to 340 kHz using 64×128 pixels with a spatial resolution of 26.22 μm/pixel, resulting in an overall field of view of 1.68×3.36 mm.

High-speed shadowgraph imaging was performed at the near field of the cup edge with the camera placed at an angle behind the cup to capture the ligament formation. The angle was chosen such that the entirety of the ligaments would be approximately perpendicular to the camera and most of the fluid in the image would be in this single plane, thus allowing the shadowgraph images to give more accurate sizes of the fluid particles. Shadowgraph imaging allowed the approximate edges of the water droplets to be identified. For each bell speed case, 150,000 consecutive images were taken, which amounts to approximately 441 ms of real-time acquisition, or nearly 37 full cup rotations for the 5,000 RPM case. The images were then processed to determine size and velocity distributions.

The use of water as a paint surrogate also gives an indication of the overall effectiveness of this method because of the fact that it is easier to image paint using shadowgraph than it is with water for a couple of reasons. Those reasons being that paint is more opaque and much more viscous than water. Therefore, the droplets have clearer edges in the images and much slower breakup times, assuming all operational parameters are equal. It can be assumed that the resulting shadowgraph data would also be easier for the image processing method presented as well.

1.2.2 Image Processing
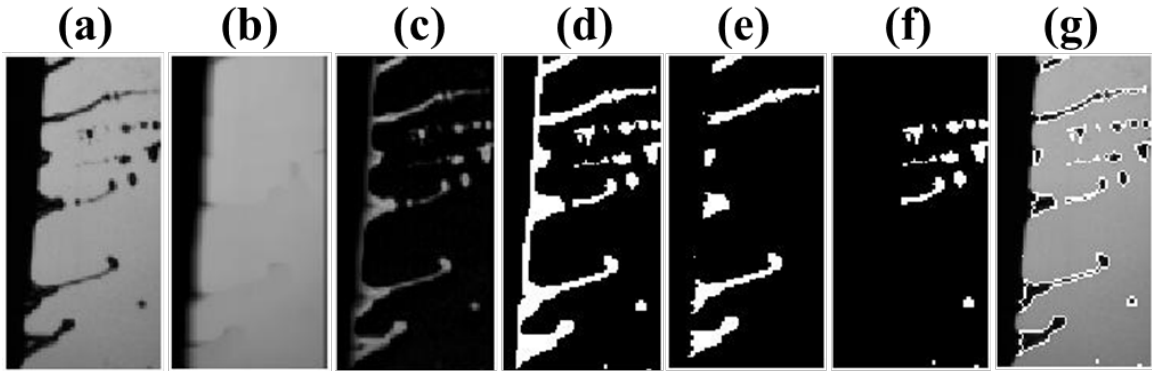
Figure 1.3. Image processing steps visualization, which includes the original image (a), dilated image (b), subtraction (c), binarization (d), ligaments-only image (e), droplets-only image (f), and edges of binarization imposed on the original image (g).

In order to process the images for both droplet and ligament size statistics, a

processing algorithm was used to first identify liquid by binarizing the image, then

connected liquid pixels were formed into groups, and finally segmented into either

ligaments or droplets. A visual representation of the image processing is shown in Fig.

1.3. Typically, background images are needed to distinguish between signal and

background noise levels. Unfortunately, the background signal differed image-to-image

since the light source traveled through the droplet cloud, which varied between cases,

before illuminating the near cup liquid, therefore an approximation for the background

light signal was needed. Using MATLAB, a pseudo-background image was calculated as

shown in Fig. 1.3b (with the original raw image in Fig. 1.3a). The background was

computed by dilating[41] the original image with a horizontal line structuring element to

suppress the individual liquid droplets that occur on small spatial scales and accentuate

any larger scale variation in background light that varies frame-to-frame. Additionally,

the geometry, orientation, and size of the structuring element was chosen due to the fact

11

that it produced the most uniform background images while still maintaining the approximate profile of the cup in the image. Maintaining the approximate cup profile was important for the later image subtraction. It is also worth noting that the reason the background light varied from image to image in the raw data was due to innate difference in the amounts of particles passing between the focus plane of the camera and the illumination source.

Once the background image was calculated, it was then subtracted from the original image to show only light that was impacted by the fluid, and therefore showing only the liquid, shown in Fig. 1.3c. Finally, this image was binarized using a static thresholding method after determining that adaptive thresholding methods, such as Otsu's method[42], did not accurately predict the threshold necessary to yield an image containing only fluid elements. Otsu's method, when applied to the image data, would often include too much of the background noise. Ultimately, the thresholding point that did yield the isolated fluid element images did not significantly change across images, and so a static threshold was chosen that gave an image of only liquid consisting of both ligaments and droplets, as shown in Fig. 1.3d. Afterwards, the outline of the processed image was superimposed on the original to check the accuracy of the processing, shown in Fig. 1.3g. Once it was determined that the edges were sufficiently captured, the method was used for the remaining images.

The images were further processed to separate the ligaments from droplets. To do this, ligaments were defined as connected fluid elements attached to the cup and droplets as any other identified liquid in the image. Connected components, with eight-neighbor connectivity, were identified in the binarized image. The eight-neighbor connectivity, in

12

this case, referring to the inclusion of the eight pixels that surround or "neighbor" every pixel in a 3×3 block through horizontal, vertical and diagonal connection. This identification meant that the ligaments and the cup from the binarized image would be taken as a single object. The largest connected component was removed from the image, since it was always the combination of the cup and ligaments attached to the cup, leaving only the droplets in the image. The largest component was then placed in its own separate image, isolating the ligaments and cup edge, and the cup edge was subsequently removed from the new image using a circular fit from the original image. All of the pixels on the edge of and inside of the arc fit were set to zero, eliminating the entirety of the cup from the image. Following the cup removal, two images that could be used to determine size statistics remained, one with ligaments only (Fig. 1.3e) and the other with droplets only (Fig. 1.3f). The combination of the statistics gained from these two images was also considered and is henceforth referred to as "combined" or "overall" statistics.

Additionally, the length and width of ligaments were calculated from the processed images. Ligament widths were calculated by taking the width of each ligament at the cup edge. Ligament lengths were calculated by using a skeleton operation[39] that approximated the ligaments as a line with a width of one pixel, and then obtaining the length of the resulting lines. Thus, the widths can be thought of as ligament base widths and the lengths can be thought of as the length of the ligament beginning at the cup. The ligament lengths and widths were calculated to further investigate general changes in ligament geometry with rotational speed.

1.2.3 Size Measurements

Once the liquid was identified, fluid size statistics were next calculated. Fluid size was measured in terms of hydraulic diameter, calculated using (2),

$$D_h = \frac{4A}{P} \qquad\qquad (2)$$

Where D_h is the hydraulic diameter, A is the area of the object and P is the perimeter. The area of each droplet was defined as the pixel count of that group, and the perimeter as the number of pixels bordering the inscribing area for each individual droplet. The area and perimeter in pixels were converted into physical distance using a calibration to characterize the optical resolution. In order to get statistically different images of the liquid flowing from the bell, every 100th frame of the data was used, as this approximated a single flow time through the field of view in the 5,000 RPM case. 1500 images were then used to determine the size statistics. Number distributions were then tabulated based on the resulting hydraulic diameter measurements. Volume distributions were also calculated by cubing the hydraulic diameters, which created a more size-weighted interpretation of the data.

To ensure that this sample size was adequate, convergence tests were performed. This was done by calculating a size distribution, from a subset of the total 1500 measurements, and computing the percent difference between this subset statistic and that for all of the 1500 measurements. A subset, as used here, refers to taking the distribution from only a portion of the 1500 images, starting with one image. Progressively more data, in increments of one image, are added until the distribution of the collective subset of the original 1500 images is approximately that of the distribution when all of the images are

included. At this point, the distribution requires no more data to better represent the process, and the distribution can be said to have converged. Fig. 1.4 shows the evolution of a single size distribution as more data is included and Fig. 1.5 represents the percent difference evolution for three cases to illustrate the convergence of the distributions further. In the case of Fig. 1.5 data, percent difference refers to the percent difference between the normalized distribution of the sum of all of the data from the first image to every image and the normalized distribution that includes all of the data. Ultimately, in the worst-case scenario, the distributions converged to less than 5 percent difference from the final distribution after approximately 700 frames were included in the dataset. Thus, the distributions are taken as statistically converged. The frames at which each of the cases converged to less than 5 percent difference can be seen in Table 1.2a.
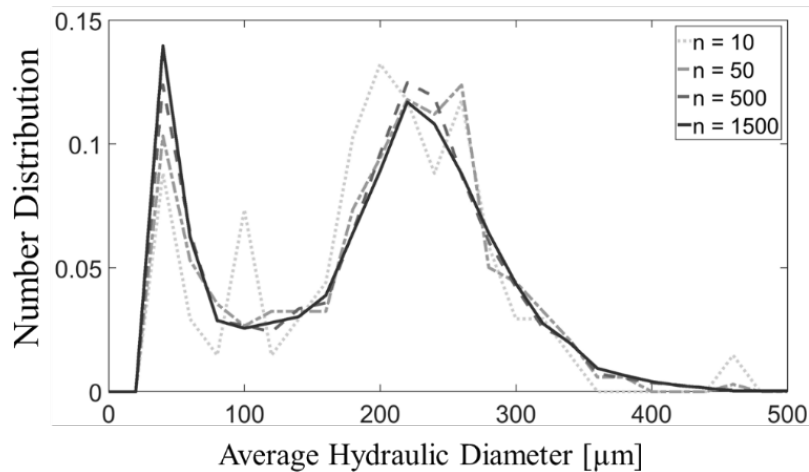
Figure 1.4. Number distributions of ligament size for the 6,000 RPM case after the inclusion of the data from varying amounts of frames, n.
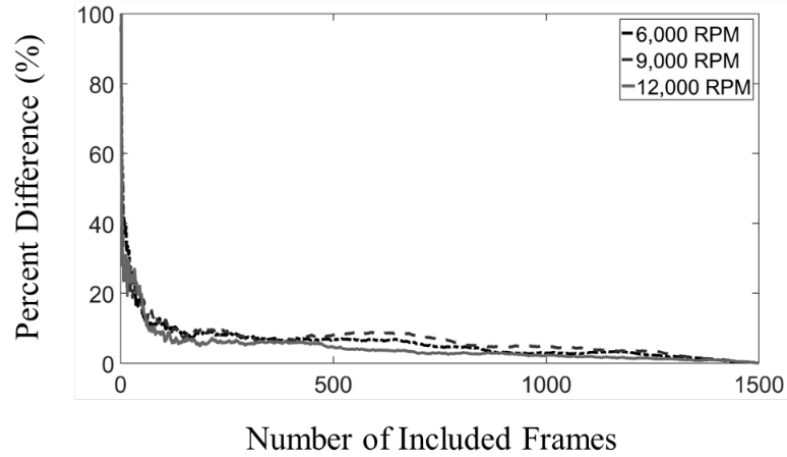
Figure 1.5. Convergence of percent difference compared to the inclusion the entire data set, of the number distributions of ligament size by including varying amounts of frames for three different bell speeds.

Table 1.2. The percentage of data (out of 1500 frames) at which the number distributions for (a) size and (b) velocity reach less than 5 percent difference compared to the final distribution (which includes the data from all 1500 images) for ligaments, droplets, and their combined statistics at each bell speed tested.

		Bell Speed [kRPM]							
		5	**6**	**7**	**8**	**9**	**10**	**11**	**12**
(a)									
	Ligaments	31.8	48.9	33.3	5.87	56.5	25.3	23.9	32.1
Size	Droplets	3.67	5.13	1.73	8.33	1.47	2.13	1.87	2.40
	Combined	3.87	7.40	5.67	8.00	4.07	3.13	1.87	2.53
(b)									
	Ligaments	25.9	21.6	22.6	38.0	45.8	44.9	35.1	47.4
Velocity	Droplets	25.8	27.5	21.2	12.6	10.5	14.9	9.47	7.53
	Combined	17.4	17.1	14.9	6.07	7.80	13.0	5.13	6.60

16

1.2.4 Velocity Measurements

LaVision Davis 8.3 was used to obtain velocity information of the individual

ligaments and droplets using combined PIV and PTV. The PIV algorithm utilized a

multi-pass cross-correlation algorithm that successively worked down from 64×64 to 4×4

pixel interrogation window sizes with 50% overlap. The results from this process were

velocity vector fields for the entire frame. The PTV option subsequently detected droplets

in the image and reoriented the interrogation window to obtain a single vector for each

droplet, discarding the remaining vectors in the velocity field. When post processing the

data, if there were multiple vectors on a single droplet, the average of the velocity vectors

was taken, and that data was subsequently used in the resulting velocity statistics. Using

the combination of PIV and PTV, not only were droplet and ligament velocities able to be

obtained, but the velocity vectors could also be correlated to the droplet and ligament

sizes.

1500 evenly spaced sets of two sequential images in time were used for velocity

calculations.   Statistical comparisons were done on one case to verify how many images

were needed for the velocity distributions to converge, in the same manner as for the

sizes, and it was found that the distributions converged to a less than a five percent

difference from the final distribution after, in the worst case, 700 frames. This result can

be found in Table 1.2b, which shows the frames at which the velocity distributions

converge to less than 5 percent difference. Thus, the 1500 sets of images are statistically

converged for both size and velocity. The spacing between image sets was the exact

same as for the size statistics, with the first image in each velocity image set

corresponding to the same image used to determine sizes. This was done so that the velocity and size statistics could be directly correlated.

1.3 Results and Discussion

1.3.1 Ligament Breakup Observations
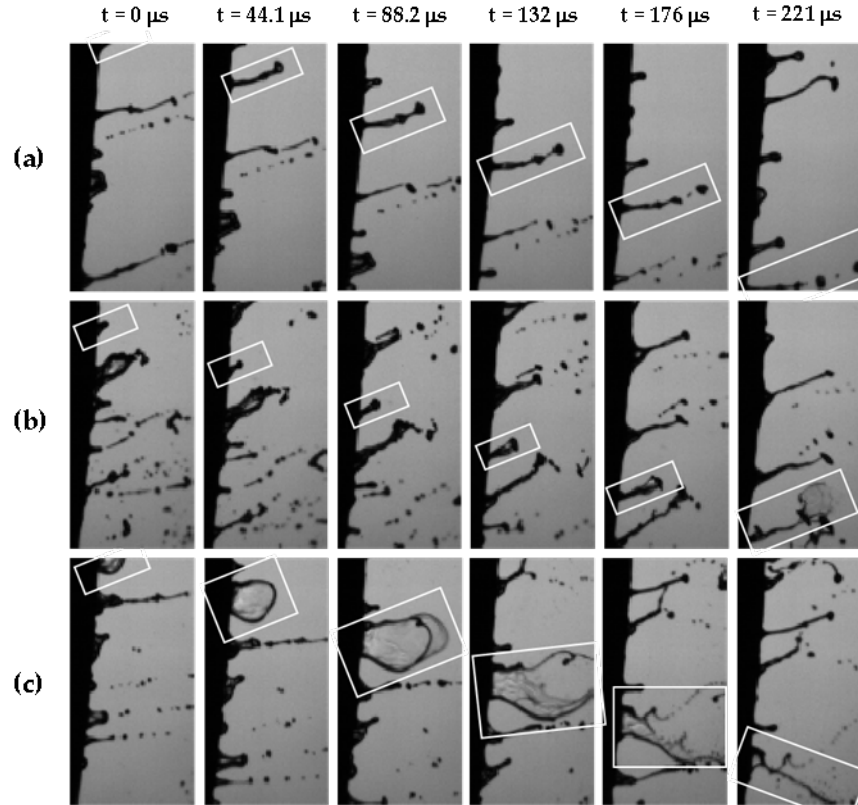
Figure 1.6. Image sequences of three different ligaments in the 5kRPM case over time (moving from left to right in the respective row): elongated ligament into droplet (top row), ligament into bag breakup (middle row) and bag breakup off of the cup (bottom row). These images within each sequence were taken 15 frames, or 44.1 μs, apart. The boxed liquid structure is the liquid of interest.

Unprocessed, consecutive experimental images were examined prior to any image processing to examine the ligament breakups for the various speeds. The raw image data was able to give information about the various fluid structures and ligament geometries that form at the edge of the cup. Combined with the high-speed camera capability,

18

detailed evolution of these structures over time was observed, as well as various fluid breakup and droplet formation mechanisms. Given that multiple rotational speeds were tested, the change in these mechanisms under additional shearing force was also observed. The observations of the ligament breakups at the 5kRPM, 8kRPM and 12kRPM are detailed in this study.

For the lowest rotational speed tested, 5kRPM, there appear to be three typical regimes of fluid breakup, which can be seen in Fig. 1.6. The first regime (shown on the row a of Fig. 1.6) appears as an elongated ligament that holds a large volume of fluid at its unstable, mushroom-tip that subsequently breaks off into a droplet. The ligament, in this case, forms a wave along its length, likely due to Kelvin-Helmholtz and Rayleigh-Taylor instabilities, and then breaks up into smaller satellite droplets along its length in addition to the droplet it forms at the tip. The necking or pinching is typical of a Rayleigh-Taylor breakup and indicates that another force, in this case, the centrifugal force, has exceeded the surface tension force. This regime closely resembles the low momentum, thick ligament growth with multiple sequential breakups in Rao et al. [43]

A second regime that often appears is shown in the row b of Fig. 1.6. The sequence begins with a standard long and thin ligament that initially forms with a larger fluid structure at the tip of the ligament, which subsequently breaks up into smaller droplets. The fluid structure at the tip rapidly expands similar to a bag breakup[44,45], as opposed to the first regime which separates the entire fluid element. Less frequently, a third regime, shown in row c of Fig. 1.6, appears which forms a ligament off the cup with a different structure. The ligament appears to be a translucent ring shape in the view of the camera, and is likely a thin-filmed ligament. The structure expands until the end of the

liquid structure bursts into much finer droplets. Both the second and third observed

breakup regimes resemble similarities to the standard bag breakup regime.
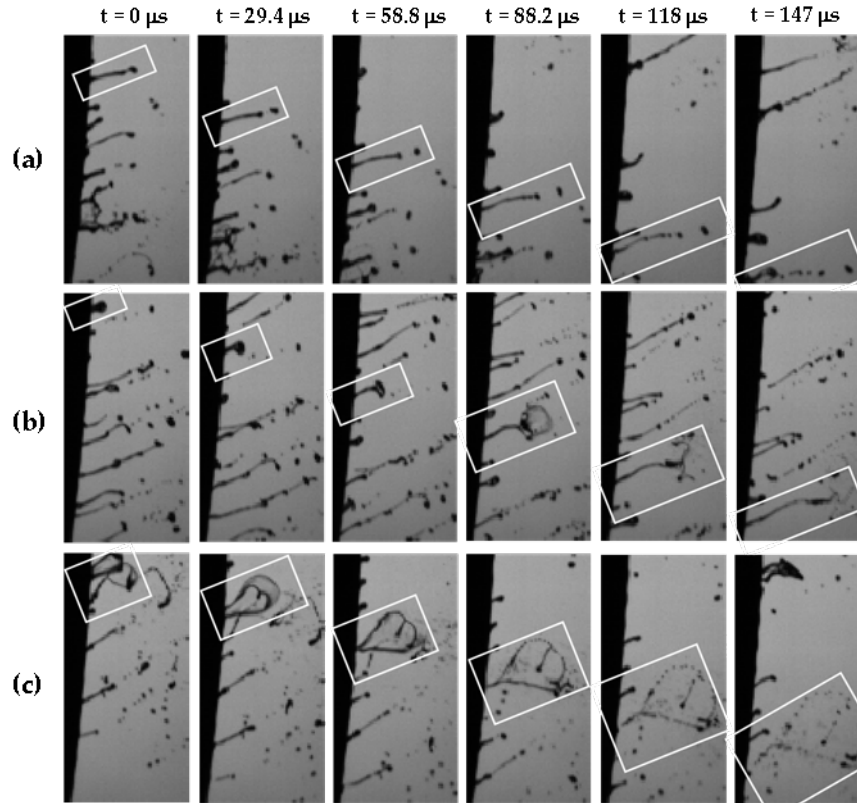
Figure 1.7. Image sequences of three different ligaments in the 8kRPM case over time (moving from left to right in the respective row): elongated ligament into droplet (top row), ligament into bag breakup (middle row) and bag breakup off of the cup (bottom row). These images within each sequence were taken 10 frames, or 29.4 μs, apart. The boxed liquid structure is the liquid of interest.

In the 8kRPM case, seen in Fig. 1.7, the ligaments are shorter and the droplets formed

have smaller diameters than in the 5kRPM case, as expected. The breakup, as a result,

occurs closer to the edge of the cup, which indicates shorter breakup times. The ligament

angle in relation to the cup also experiences a notable increase, which then translates into

a change in the projection angle at which the droplets are ejected from the ligaments. This

result is expected as well since the only change was rotational speed, which would thus

increase the shearing force on the ligaments. Additionally, the same regimes that

appeared in the previous case are observed to appear in this case. However, the elongated

ligament to droplet breakup (row a of Fig. 1.7) appears more prevalent and breaks up into

more droplets along its length. The other notable difference is that the breakup in the row

c of Fig. 1.7 also resembles the bag-stamen type of breakup[44] as opposed to only a bag

breakup.
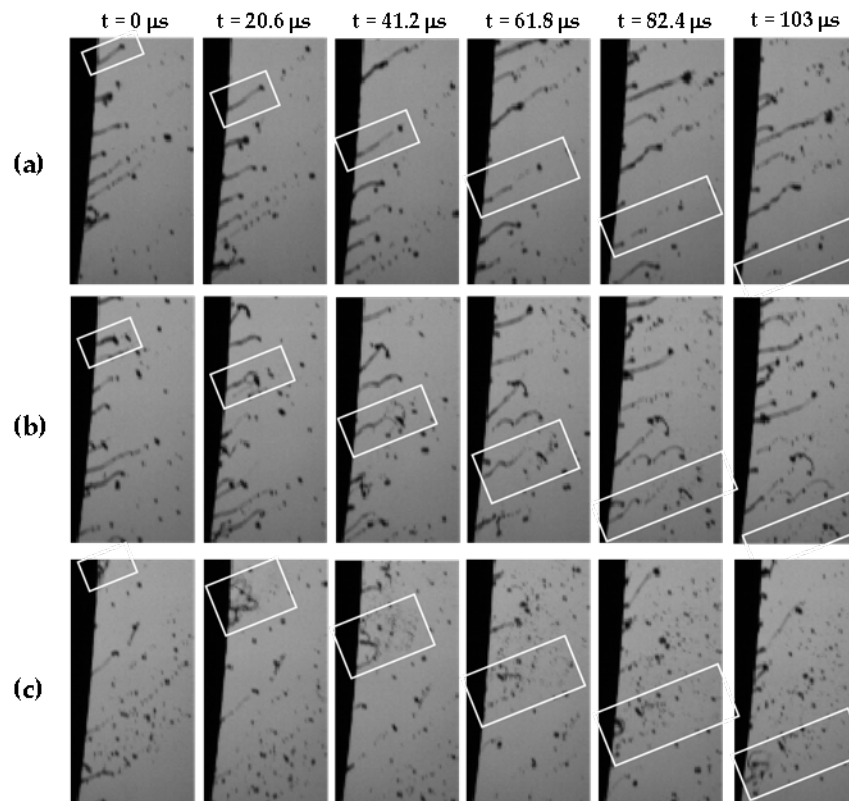
Figure 1.8. Image sequences of three different ligaments in the 12kRPM case over time (moving from left to right in the respective row): elongated ligament into droplet (top row), ligament into bag breakup (middle row) and bag breakup off of the cup (bottom row). These images within each sequence were taken 7 frames, or 20.6 μs, apart. The liquid structure of interest is boxed for convenience.

Finally, in the 12kRPM case, seen in Fig. 1.8, the ligaments and droplets again become even smaller and disintegrate faster. The angle between the ligaments and the cup increases further still, and all of the mentioned regimes are still present. Additionally, the two forms of bag breakup (row b and c of Fig. 1.8) appear even less frequently as the elongated ligament into droplet breakup (row a of Fig. 1.8) becomes more dominant. The elongated ligaments also break into even more droplets along the ligament length than in the 8kRPM case. Another observation is that the second type of breakup, seen in the row b of Fig. 1.8, possibly transitions to a dual-bag breakup[46] and that the breakup sequence in row c may transition from bag-stamen to shear-stripping breakup[44]. Such results indicate that droplet formation modes which normally occur in secondary breakup regions are occurring in the primary breakup region in this process. They also indicate that the increasing difference in shearing force versus surface tension forces is advancing the type of breakup to smaller droplet sizes. All of these trends are continuations of the changes from the 5kRPM to 8kRPM case and can be said to be trends of the system as a whole under the conditions tested.

1.3.2 Size Statistics

The number and volume distributions for the ligaments and droplets, both separately and combined, are shown in Fig. 1.9. These distributions were calculated by binning the hydraulic diameter statistics in 20 μm intervals and then normalizing the curves by the sum of the distribution. For the ligaments-only and droplets-only data, it is worth noting that the sum of overall distribution, which includes the data for both, was used instead of their respective sums. This normalization was done to show the relative contribution of

the ligaments and droplets to the overall distribution. The droplets dominate the shape of the overall number distribution curve, which is expected since on average there are considerably more droplets in a given image than ligaments. Thus, an expanded version of the ligament number distribution was inset to better display its shape.

The number distributions show a shift for the droplets-only (Fig. 1.9b), ligaments-only (Fig. 1.9c) and overall (Fig. 1.9a) distributions to smaller hydraulic diameters with increasing rotational speed. This trend is accentuated in the respective volume distribution graphs for the ligaments-only (Fig. 1.9f), droplets-only (Fig. 1.9e) and in the overall case (Fig. 1.9d). The ligaments-only number distribution, shown in Fig. 1.9c, is bimodal with a peak at larger hydraulic diameters shifting towards lower hydraulic diameters with higher rotational speed. The droplet-only distribution, shown in Fig. 1.9b, shares a similar peak-shift to lower hydraulic diameters, but is not bimodal. These results collectively indicate that there are two regimes of ligament size in the near-cup field of view that lead to a single distribution of droplet sizes. Both ligament and droplet sizes decrease with increasing rotational speed.

It is worth noting that the peak at smaller hydraulic diameters for this data occurs near the resolution limit of the optical setup; thus, any change in the diameters of these small particles with rotational speed is not resolved. The percentage of particles in this peak increases, without shifting, until the 12,000 RPM case where the particles are small enough to avoid being detected by the image processing. Such a result can be seen in Fig. 1.9c where the ligament distribution experienced a large reduction in small particle data.

23
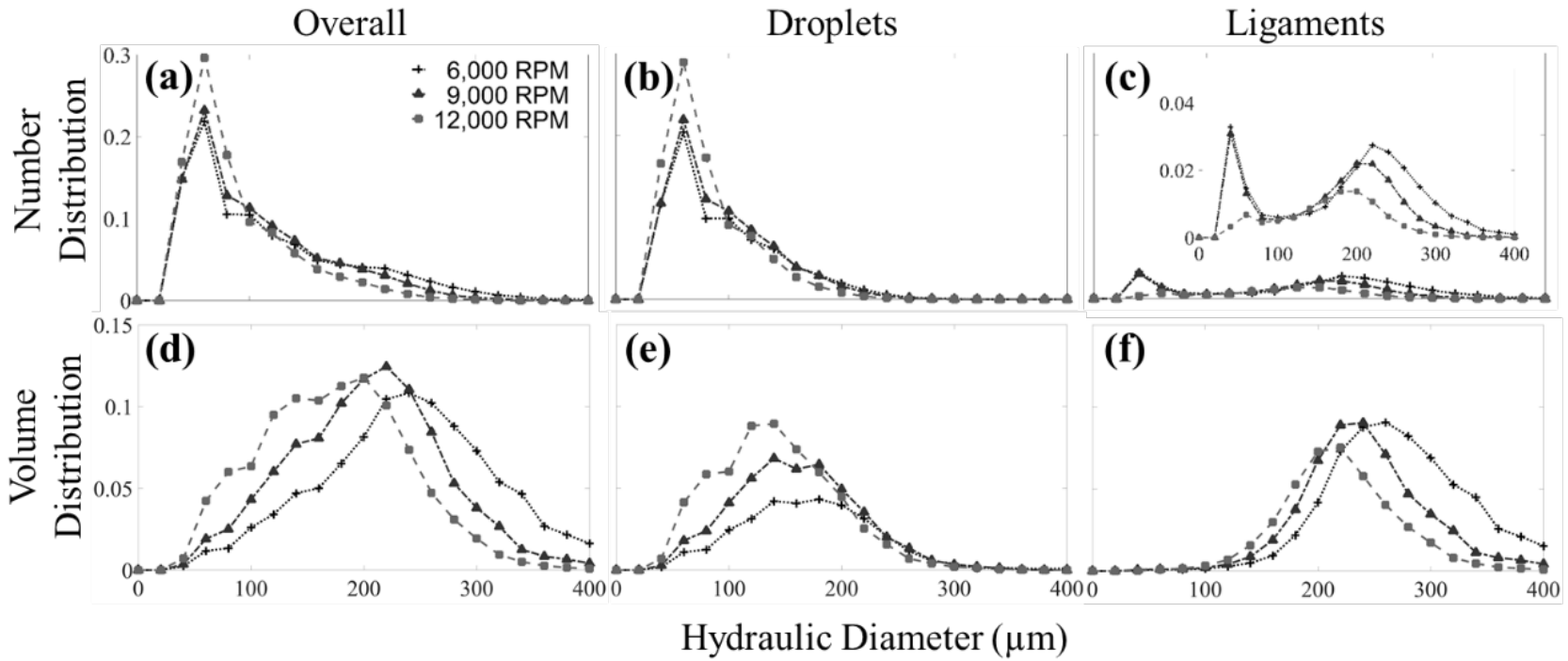
Figure 1.9. Number (a-c) and volumetric (d-f) distributions of droplets (b,e), ligaments (c,f) and overall (a,d) for the 6,000 RPM, 9,000 RPM and 12,000 RPM bell speed cases.in 20 ▢m intervals and then normalizing the curves by the sum of the distribution.

Additionally, despite the exclusion of electrostatic forces, the bimodality of the distributions is a result that matches what is found in the literature for electrostatic droplet size distributions[6].

The shapes of these droplet distributions are consistent to what is reported in the literature. However, the ligaments have never been measured in this way, with a hydraulic diameter approximation. With the documented shrinking of ligament width in this rotational rate regime[35], it can be assumed that the hydraulic diameter that has been calculated should also decrease. The ligament length and width number distributions, shown in Fig. 1.10, illustrate this expected trend of decreasing size with increasing bell speed. These distributions were calculated in the same way as in Fig. 1.9, except the ligament lengths were binned for every 300 μm and the ligament widths were binned for every 40 μm. It can be seen that with increasing rotational speed, the lengths and widths of the ligaments both decrease. The ligament lengths and width results are more directly analogous to what has been found in literature than the hydraulic diameter approximation, and the trends in the values are the same.
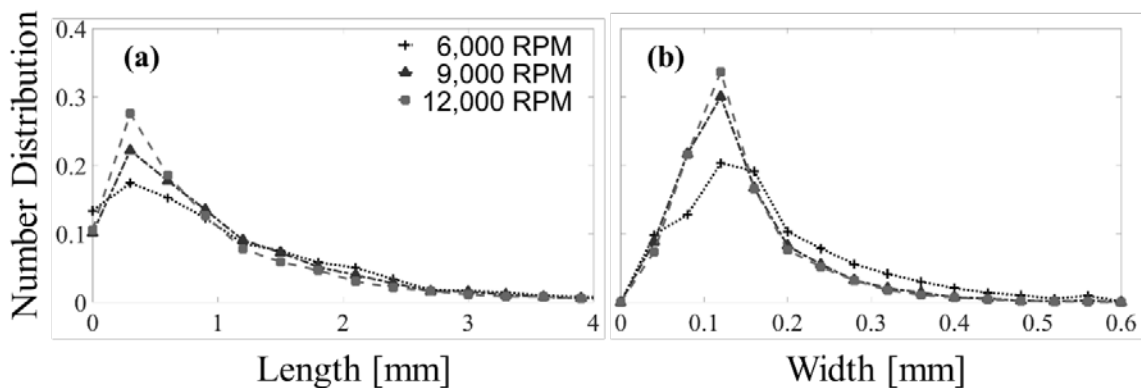
Figure 1.10. Ligament length (a) and width (b) number distributions for the 6,000 RPM, 9,000 RPM and 12,000 RPM bell speed cases.

The span of each distribution was calculated to give a measure of the variability for each case that could be compared. Sauter mean diameters (or D_{32}) values, defined in (1), which can give an estimate of average particle size when only a surface diameter is known, were calculated to assign a single, characteristic value to each size distribution that could be compared across cases. The respective spans and D_{32} values for the droplet, ligament, and overall distributions are given in Table 1.3. The droplet spans are calculated using (3),

$$\Delta_v = \frac{D_{.9} - D_{.1}}{D_{.5}} \qquad (3)$$

where Δ_v is the relative span factor and $\boldsymbol{D_P}$ is the hydraulic diameter at which the cumulative distribution is equal to P for each respective value. The results from Table 1.3a show that the total span did not significantly change with increasing rotational speed for the ligaments and overall statistics, but increased by 15.9% for the droplets from the lowest to highest rotational speed case. An increase in the span for the droplets suggests greater droplet size variability in the spray when flowrate remains constant but rotational speed is increased. The D_{32} calculations, given in Table 1.3b, also further display the trend of decreasing fluid particle size with increasing rotational speed. This trend for the Sauter mean diameters is expected for this system since only the rotational speed is changing.

Table 1.3. Fluid size spans (a) and D32 [µm] values (b) for ligaments, droplets, and their combined statistics for each tested bell speed.

		Bell Speed [kRPM]							
		5	**6**	**7**	**8**	**9**	**10**	**11**	**12**
(a)									
	Ligaments	0.61	0.60	0.57	0.56	0.56	0.56	0.58	0.58
Span	Droplets	0.84	0.86	0.90	0.93	0.87	0.94	0.95	0.99
	Combined	0.87	0.86	0.86	0.88	0.86	0.89	0.92	0.96
(b)									
	Ligaments	274	252	234	223	221	209	205	201
D_{32} [µm]	Droplets	153	144	136	132	137	124	123	119
	Combined	228	207	187	175	175	159	153	146

Overall, the respective trends of the various size statistics presented match what is found in the literature for similar systems, but at different locations farther downstream. These comparisons were made to demonstrate that this imaging and post-processing method could be effective at both capturing and analyzing the data typically studied in this field, but with the added ability to determine simultaneous size-dependent velocities.

1.3.3 Velocity Statistics

The fluid velocity distributions for the magnitude of the velocity vectors and both the tangential components of those vectors with respect to the cup are shown in Fig. 1.11. These distributions were calculated in the same manner as the size distributions, but with bin intervals of 2 m/s. Clearly, for each case, as the rotational speed increases, the velocity magnitude also increases. This result is expected since the bell is rotating at higher rotational speeds; however, the ligaments and droplets peak at different velocities. The vertical lines in Fig. 1.11 indicate the magnitude of the cup tangential speed for each case. As the bell speed increases, the peak ligament velocity approaches the tangential

cup velocity, but is greater than the tangential cup velocity for low rotational speed. In contrast, the peaks for the droplet distributions are centered approximately at the tangential cup velocity across all cases. An interesting result, however, is the apparent broadening of the tangential velocity distributions to the left of their peaks across all cases as the rotational speed increases in Fig. 1.11. Such a result means that the fluid distributions begin to increasingly favor smaller velocity vectors as rotational speed is increased. This could be indicative of more collisions happening or increased interference from air recirculation, which would result in greater numbers of fluid particles being slowed.

The mean velocity was calculated for both the velocity vectors and the tangential component of the velocity vectors for their respective ligaments-only, droplets-only and overall data sets. The results of these calculations can be seen in Table 1.4, compared to the calculated tangential cup speed, based on the rotational speed and cup diameter. These calculated values further show that as bell speed is increased, droplet and ligament velocities also increase, as expected.
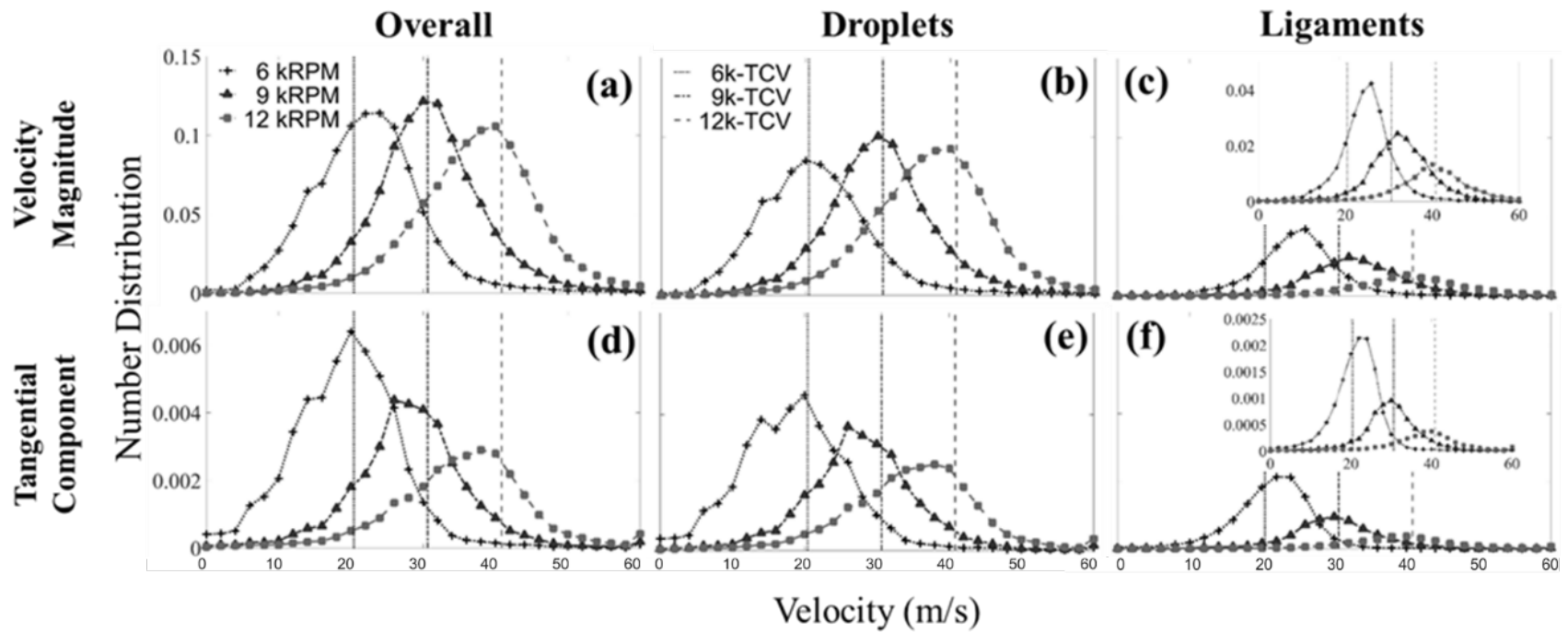
Figure 1.11. Velocity number distributions of ligaments (c,f), droplets (b,e), both (a,d) and associated tangential cup velocity (TCV) plotted as vertical lines for the 6,000 RPM, 9,000 RPM and 12,000 RPM bell speed cases.

Table 1.4. Comparison of the mean velocity values for the original velocity vectors and the tangential component velocity vectors at each bell speed tested to the calculated tangential cup speed.

				Bell Speed [kRPM]				
	5	**6**	**7**	**8**	**9**	**10**	**11**	**12**
Tangential Cup Speed [m/s]								
	17.0	20.4	23.8	27.2	30.6	34.0	37.4	40.8
V_{avg} – **Total [m/s]**								
Ligaments	20.3	24.9	26.7	28.9	32.9	36.3	38.7	40.9
Droplets	18.5	21.7	24.8	27.3	30.8	32.9	35.6	37.9
Combined	19.0	22.5	25.2	27.6	31.2	33.4	36.0	38.2
V_{avg} – **Tangential [m/s]**								
Ligaments	16.9	21.5	25.2	27.1	30.0	33.7	36.6	38.5
Droplets	15.6	18.7	21.9	24.5	27.9	29.9	32.8	35.0
Combined	16.0	19.4	22.6	25.0	28.3	30.5	33.3	35.4

Additionally, the average tangential component of velocity for the ligaments, across all cases, is almost exactly that of the calculated tangential cup speed. This result makes sense given that the ligaments were defined as fluid elements still attached to the cup, and therefore their velocity should essentially match. Notably, the values show that despite the locations of the peaks of the droplets-only velocity distributions approximating the tangential cup speed, the ligaments-only data is the case that has a mean closest to the tangential cup speed. This implies that the detached droplets are experiencing acceleration or deceleration likely due to the shaping airflow, even at such a close proximity to the cup.

Most of these results are expected, though they have not been explicitly found in literature for the near-field region of this type of atomizer. The average velocity conditioned on particle size was next computed as shown in Fig. 1.12, to study the effect of particle size on these velocity vectors. These values were calculated by conditionally

averaging the velocities of fluid particles within specified diameter bins. The results

again show the expected result that the ligaments are moving faster than the droplets in

the flow, independent of size. However, they also demonstrate that the larger fluid

particles, both ligaments, and droplets, move at higher velocities at larger sizes. Thus, the

combined optical setup and image processing performed allowed for size and velocity

data for all fluid particles in the images, from a single data set. It is worth noting that

recent work showed that larger droplets tend to have slower impact velocities closer to

target in high-speed rotary bells[47]. Further investigation is needed to understand the

trend transition in the spray flowfield (plume).
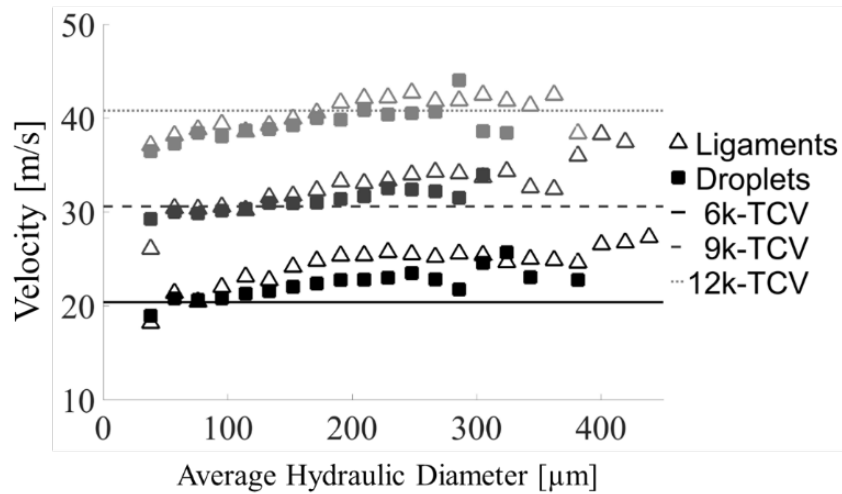
Figure 1.12. Velocity vs. size distributions of ligaments (triangles) and droplets (squares) and the associated tangential cup velocity (horizontal lines) for the 6,000 RPM (solid), 9,000 RPM (dashed) and 12,000 RPM (dotted) tangential cup velocities.

1.4 Conclusion

Using high-speed shadowgraph imaging, qualitative ligament breakup mechanisms

were observed, and quantitative droplet and ligament sizes were measured for a rotary

bell atomizer, with the inclusion of shaping air, near its cup edge for eight operational

bell speeds. In regards to the qualitative observations of the ligament to droplet breakup for the conditions tested, several notable trends were found. First was that there were multiple ligament breakup regimes for a given rotational speed. The first of these regimes was that of a ligament forming an unstable, mushroom-tip as it grows, and then having that fluid mass eject as a droplet while the rest of the ligament forms into satellite droplets along its length. The next two regimes were different forms of bag breakup where a bag of fluid is formed at the end of a ligament and eventually explodes into satellite droplets. As rotational speed was increased, the dominance of the first type of regime also increased. The two bag breakup regimes were also seen to evolve and become more catastrophic in their breakup. Visually, the ligaments in the images can also be seen to become shorter, and breakup faster, with higher rotational speed. Other changes with increasing rotational speed are an increase in ligament angle to the cup and an increase in the number of satellite droplets in a given fluid disintegration. Further investigation into modeling or predicting these ligament structures and behaviors under these conditions is necessary.

The imaging technique used also allowed for a large quantitative sampling of both droplet and ligament sizes. An image post-processing method was utilized to distinguish between the fluid particles and background illumination accounting directly for frame-to-frame variations in background signal. Once the images were binarized, the fluid sizes were calculated. In addition, images of only the droplets, with very little background noise were used to calculate velocity vectors and to correlate these velocities to individual particles.

This method was demonstrated on water as opposed to paint. However, it is easier to image paint using shadowgraph than it is with water for a couple of reasons. First, paint is more opaque and much more viscous than water. Therefore, the droplets have clearer edges in the images, much slower breakup times, and larger sizes, assuming all operational parameters are equal. It can be assumed that the resulting shadowgraph data would also be applicable for the image processing of paint experiments.

The resulting size distributions showed that both ligament and droplet hydraulic diameters, as well as overall ligament length and width, decrease with increased rotational speed. The distributions also illustrated that ligaments have a bimodal size distribution, indicating two separate regimes of ligament size in the images. The droplets, however, appeared to have a singular mode size distribution with a slight skew towards larger droplets that began to narrow with increasing rotational speed. This result suggests that the range of droplet sizes, in the field of view, imaged and within the parameter ranges tested, narrows with increasing rotational speed.

The post-processed images were examined using PIV and PTV to determine droplet and ligament velocities. The raw velocity magnitude distributions indicate that the droplet velocities center on the tangential cup velocity, while the ligament velocities center near a velocity that is slightly higher than the tangential cup speed, but maintains an average velocity very close to the cup speed. This result could be an artifact of the effect of the liquid flow velocity or shaping airflow in the system. The velocity magnitude distributions show that as cup speed increases, the ligament velocity distribution begins to approach the tangential cup speed. This indicates the peaks are more closely approaching the numerical average of the ligament data and that other forces in the

system become less important if bell speed is sufficiently increased at these parameters. These results are also reaffirmed by the hydraulic diameter relation to average velocity that show the same trend for ligament and droplet velocities with respect to the tangential cup speed.

To conclude, an image processing method was developed to gather relevant data from a rotary bell atomization system operating at relevant parameters to that of an assembly plant, all from a single set of image data that was captured continuously. The method demonstrated both that it could produce data that matched results found in literature, and could provide some new insight into fluid interactions and trends within the rotary bell atomization process. Future application of this tool could be in the monitoring of in-use bell applicators to allow for feedback on potential changes in specified, relevant flow parameters. Such development would be even more relevant to possible paint application in assembly plants.

CHAPTER TWO: INVESTIGATION OF EFFECT OF SERRATIONS IN ROTARY

BELL ATOMIZERS THROUGH NEAR FIELD PULSED LASER SHADOWGRAPHY

2.1 Introduction

As mentioned previously, automotive rotary bells operate at very high rotational

speeds. Additionally, not much work has been done to characterize the region of the

spray prior to the secondary atomization of the shaping air of the system directing the

spray towards the substrate. This region is where the liquid undergoes the primary

atomization of ligament formation to droplet formation at the edge of the cup at speeds

applicable to the automotive industry. Therefore, there is a need to both image and

characterize this near field region and fluid dynamics and interactions change as

operational parameters like bell rotational speed and liquid flowrate are altered.

This work also attempts to investigate the differences between a rotary bell that has

serrations and one that is unserrated. Serrations on the edge of the bell cup help to form

ligaments [48] and are designed to artificially control the spacing between ligaments

during the atomization process [49]. At higher flowrates, ligaments merge into a sheet of

liquid, which implies they have flooded the serrations. At high bell speeds, multiple

ligaments can be seen between the serrations and droplet size in the spray decreases [49].

Some work has already been done to characterize the effects of serrations on rotary bells.

Corbeels [10] found that, in studying only a serrated bell cup, high viscosity fluid filmed

the bell evenly and produced regular, long ligaments, whereas low viscosity fluid could

film incompletely and produce irregular ligaments at the bell edge. They also found that

their particle size data, which was measured at a single location 35 mm from the bell

edge, was not sensitive to large changes in viscosity or flowrate at bell speeds higher than

20,000 RPM. This work will be using a low viscosity fluid operating with rotational speeds of at and above 20,000 RPM.

Im et al. [6], in reference to only a serrated bell, found a few interesting results relevant to serrated bell characterization as well. One finding was that liquid sheet atomization was seen to link ligaments at the bell edge if the flowrate was greater than 250 ccm. This work will show results for flowrates at and above this value. Another finding was that bimodal droplet size distributions appear at 7.62 cm from the target plane at 20,000 RPM, but mostly disappear at around 50,000 RPM, and that at 40,000 RPM, the formation of multiple ligaments could be observed between serrations. This work will attempt to show distributions, albeit in a different regime of the spray, that are at these speeds and aim to confirm the finding that drop size decreases with increase in bell speed found in the study. They concluded noting that the exact cause of the bimodal distribution was unclear and that more study would be required to find the cause, but speculated that it could be due to a dual mode of coexisting ligament and film breakup inherent to ESRB atomization.

Later, Domnick et al. [50] found that serrated bells yield a bimodal size distribution that could be a result of imperfections in the geometry of the serrations. In follow-up work [51], they tested three different cup geometries consisting of an unserrated bell, a serrated bell, and a cross-serrated bell at flowrates of 200 ccm and 500 ccm. They found that the serrations, which have the purpose of narrowing size distributions to give an advantage over an unserrated bell, did not actually narrow the droplet size distributions. This was evidenced by their span data comparisons from their volume distributions, where it was found that span values remained fairly constant for the unserrated bell, but

36

the two serrated bells experienced increasing span factors at increasing bell speeds due to the formation of bimodal distributions. Ultimately, they found that the unserrated bell produced smaller droplet sizes at lower bell speeds, but that the differences between the unserrated and serrated bells diminished in this respect at rotational speeds above 50,000 RPM. The following work aims to find if such trends exist for a low viscosity liquid operating at similar parameters, but in a region much closer to the bell edge.

Previously, in Chapter 1 of this thesis, high-speed imaging was used with a lamp backlight for rotational speeds of 5,000-12,000 RPM. Beyond these speeds, the images became somewhat blurred and therefore unreliable for deriving size statistics. Another problem with the high-speed imaging experiment, detailed in the previous chapter, included the reduced resolution that was inherent to the optical setup. To reach such high image acquisition speeds as 340,000 Hz, the image needed to use less and less of the chip, which resulted in smaller and smaller frame and thus image resolutions. As rotational speed was increased, the fluid sizes in the images became smaller. This meant the method could not go to higher speeds unless both image resolution was increased to compensate for the smaller fluid particle sizes and the image acquisition speed was increased. In order to resolve these issues, a different optical setup was devised.

High-speed imaging was chosen originally to obtain size and velocity statistics simultaneously since the images would be correlated in time. By abandoning the time correlation, and therefore ability to gather fluid particle velocities, laser pulsed imaging could be adopted, thereby resolving both the image resolution and image acquisition rate issues of the high-speed method. The use of lasers, including Nd:YAG as the light source for shadowgraphy certainly has precedence [52,53]. However, laser speckle is often a

problem in imaging with this method as the signal-to-noise ratio in the background can be very high [54]. A fluorescent material can be used to reduce this signal-to-noise ratio, which is a measure of laser speckle, by providing an intermediary fluorescence with a more incoherent, and thus uniform, light profile. Though light reflection off optical components, like the glass surface used in the following experiment, can have the consequence of energy loss, there are ways to circumvent that problem. One such solution has been to use antireflection coatings [55]. These coatings often incorporate optically active materials that enhance spectral transmission.

Rhodamine, in particular, is a dye used in in a variety of filter applications and can be used as a laser diffuser to produce a more uniform light background [56]. It also has an absorption spectrum in the correct range for Nd:YAG lasers as well as a suitable fluorescence lifetime when used in a methanol solution [57].

Using this information collectively, in the following experiment, a pulsed laser is used in combination with a fluorescent material, Rhodamine 6G, in a glass cuvette to create adequate background illumination for shadowgraphy of a rotary bell atomizer with both a serrated and unserrated bell-cup. The region being imaged is small enough and the image resolution high enough that the primary atomization of the water is both captured in the frame, and well resolved. Such a setup will help to characterize the primary atomization, or ligament breakup into droplets, for a low viscosity fluid in both serrated and unserrated cases across high flowrates and rotational speeds to add to the work that has already been done. This method is also being introduced as a potential additional measurement method to effectively capture relevant size statistics at very high rotational

speeds and a way to numerically differentiate ligament and droplet statistics in a similar

manner as to what was done in the previous section, but at higher speeds.

2.2 Materials and Methods

2.2.1 Experimental Setup

A Dürr Ecobell2 rotary bell atomizer equipped with 65 mm diameter serrated bell-

cup, and later the same cup but without serrations on the cup edge, both pictured in Fig.

2.1, was used in this experiment. The rotary bell was operated at speeds of 20kRPM,

35kRPM and 50kRPM with flowrates of 250ccm (low) and 750ccm (high) for the

20kRPM and 35kRPM cases. For the 50kRPM rotational speed, 250ccm (low) and

500ccm (high) was used due to a limitation in the rotary bell system preventing the

flowrate from reaching 750ccm at the 50kRPM case. Additionally, during operation, the

water released from the bell was contained within a side-draft paint booth.

Figure 2.1. Unserrated (left) and serrated (right) 65mm bell-cups.

The camera used to capture the images in the experiment was a Mightex Monochrome 1.3 MP 1/3" CCD camera (model number CGN-B013-U) equipped with Navitar lens system consisting of a 1-6010 C-mount coupler, a 1-6232 lens body tube and a 1-60112 lens attachment. The camera used was chosen to maximize resolution, with 1280×960 pixels, and the lens system used was chosen to narrow the field of view. The result was a spatial resolution of 1.785 μm/pixel, resulting in an overall field of view of 2.285×1.714 mm. A 3.5mL glass cuvette filled with a solution of less than 0.01 grams of Rhodamine 6G and pure ethanol served as the illumination source for shadowgraph imaging through a Q-switched 532 pulsed Nd:YAG laser firing at 15 Hz at the cuvette. This allowed some optical filtering which eliminated much of the speckle pattern of the captured background images, without the bell running, as seen in Fig. 2.2. As can be seen from the figure, the addition of the rhodamine solution increased the incoherence of the light source such that the pixel intensity distribution of the background speckle moved to much higher intensity values and the distribution width narrowed. The camera and illumination source were placed on opposing sides of the rotary bell, acting as the transmission mode, as shown in Fig. 2.3. Additionally, the acquisition rate of the camera was equal to the fire rate of the laser, as the camera was synced to the laser to capture the illuminated shadowgraph image that occurred after the laser fired during a one-millisecond exposure time.
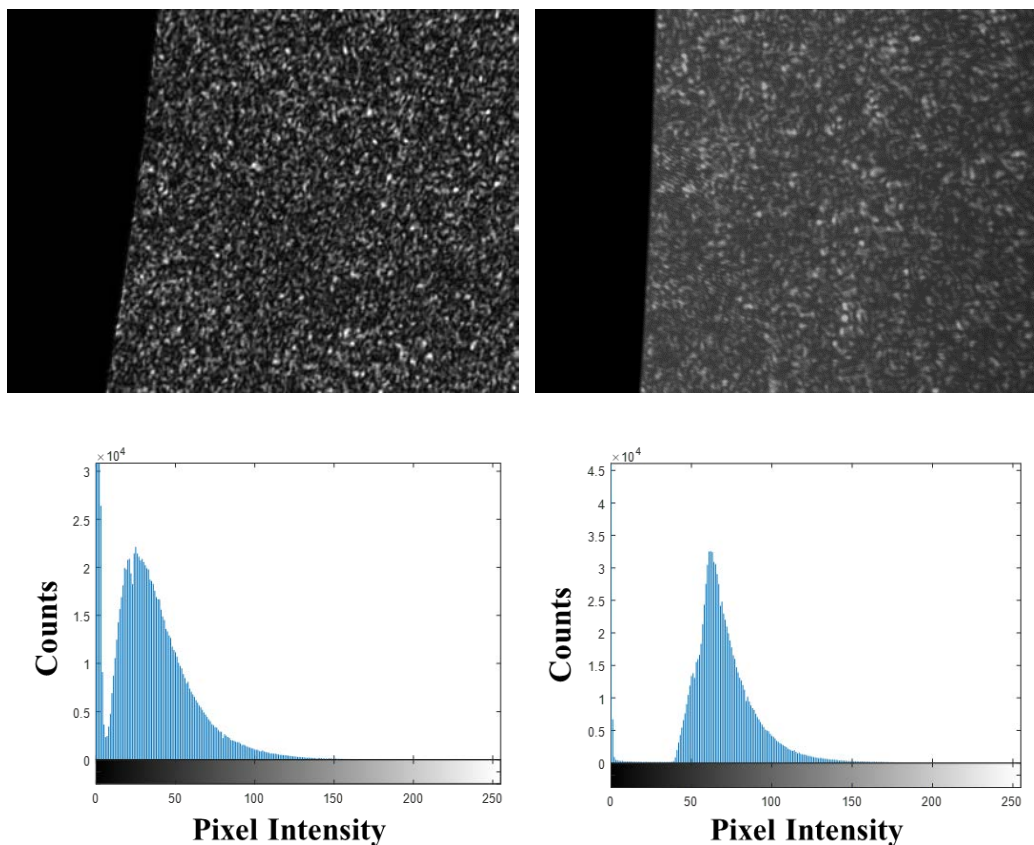
Figure 2.2. Original laser backlight (top-left) compared to the rhodamine illuminated laser backlight (top-right). Pixel intensity histograms of the original laser backlight image (bottom-left) and the rhodamine illuminated laser backlight (bottom-right).
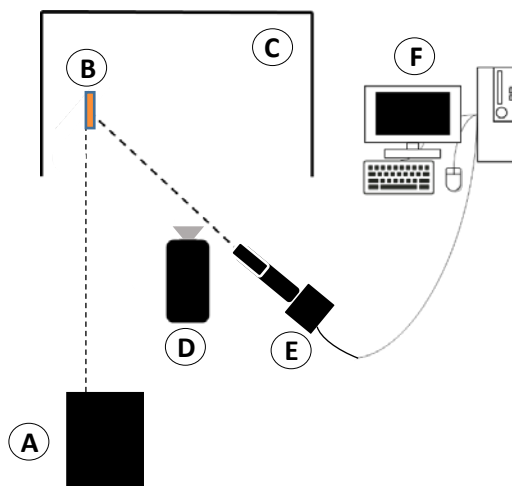
Figure 2.3. Experimental diagram with Nd:YAG laser (A), rhodamine and methanol solution filled cuvette (B), hood (C), rotary bell (D), camera and lens setup (E) and computer (F).

41

The near field of the cup edge was the area being imaged, so that the ligament size evolution across different conditions could be effectively captured and compared. Due to this aim, the angle behind the cup relative to the camera was chosen such that the ligaments would be in a single plane, meaning that the ligaments would be approximately perpendicular. This positioning aspect of the experimental setup was similar to the one discussed in the previous chapter with the high-speed camera. Shadowgraph imaging was again used to allow the approximate edges of the ligaments and droplets in the images to be identified. For each bell rotational speed tested, 1500 consecutive images were taken over a 100-second period. The images were then put through a similar image processing technique as before, but with some altered thresholds unique to the image sets taken.

2.2.2 Image Processing

The method of processing images was very similar to the one used before, however, the image resolution was much higher, so some alterations were made. As before, the creation of a pseudo-background was necessary to enhance the contrast between objects and make the image thresholding much easier. First, using MATLAB, a histogram was made of the intensity values of the pixels of the raw image. It was found that there were two peaks in the image, seen in Fig. 2.4. After some investigation, it was found that a large portion of the second peak was background noise. Therefore, the maximum value of that peak was found for each image and the image was thresholded such that any pixel intensities greater than that were deemed background noise and assigned the maximum intensity value so that they would later be automatically filtered out of the image. An example of this can be seen in Fig. 2.5.

42
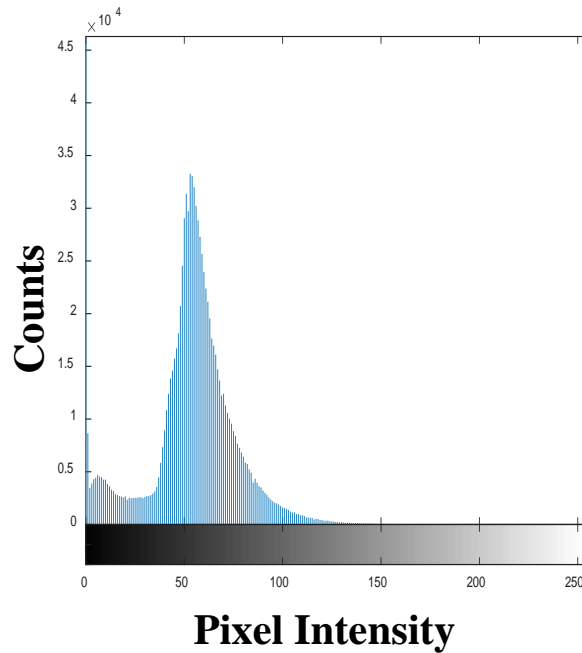
Figure 2.4. Representative example of intensity value histogram of one of the raw images.
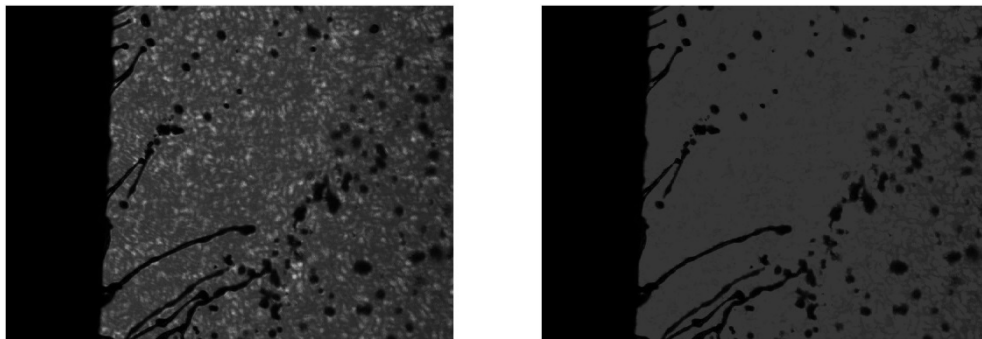
Figure 2.5. Example image of pre-filtering of thresholded intensity (left) and post-filtering (right).

Following this initial thresholding, an averaging filter followed by an image

dilation (which can be seen in the HS_Img_Processing.mat script of section A.1 in the

Appendix) was used to finalize the pseudo-background image. Next, the image was

binarized using an adaptive MATLAB binarization function to account for the small

variations in background light intensity that occur when different experimental conditions

are run. In the binarization, some of the smaller droplets' full shapes were not being

effectively captured, so holes in small objects in the image were filled in using imfill,

another built-in MATLAB function. The function, imfill, in the way that it was used for

this image processing, fills holes in the input binary image. Finally, very small objects in
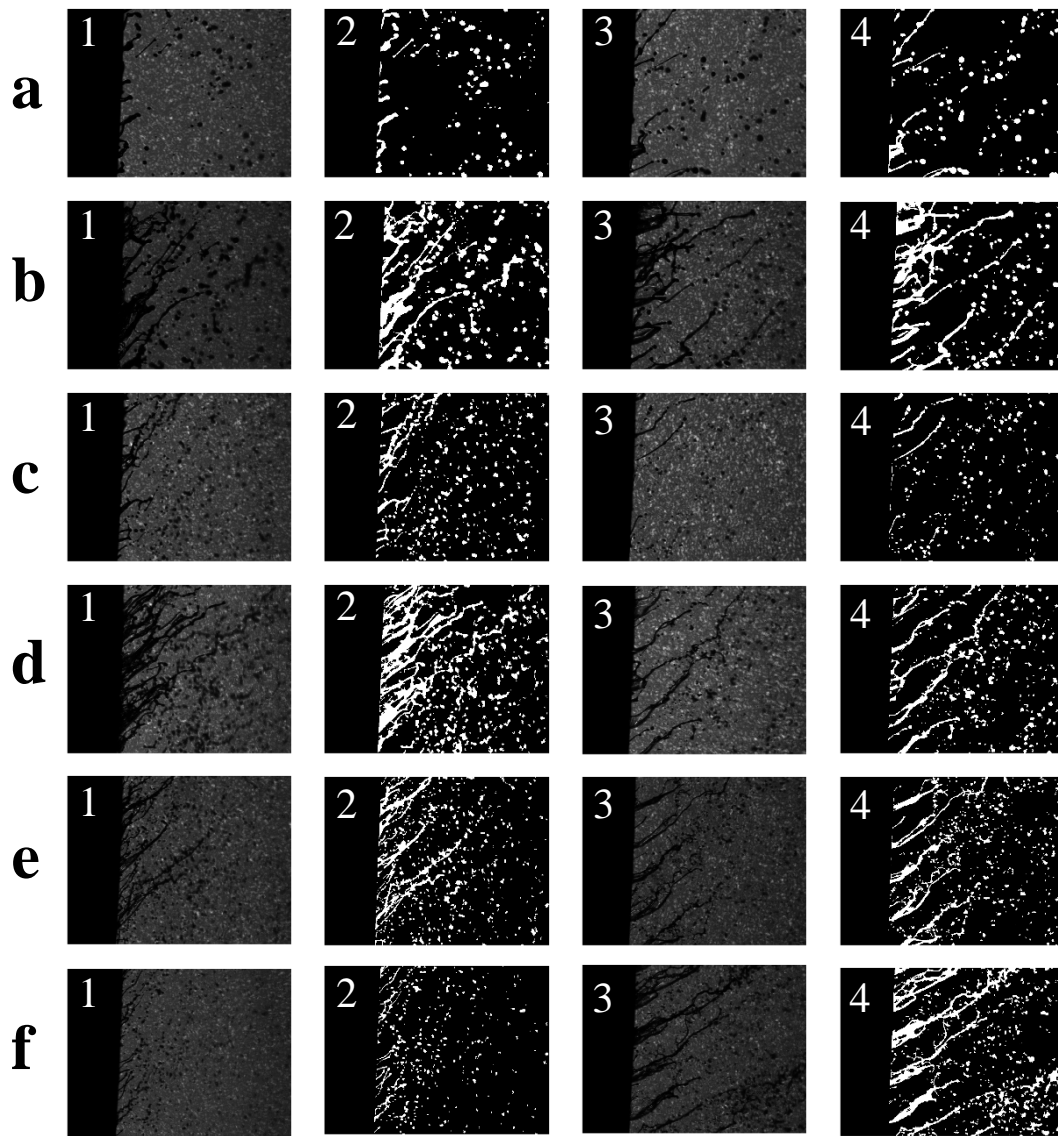
Figure 2.6. Unserrated raw (column 1) and processed (column 2) and serrated raw (column 3) and processed (column 4) examples from the (row a) 20kRPM, 250ccm, (row b) 20kRPM, 750ccm, (row c) 35kRPM, 250ccm, (row d) 35kRPM, 750ccm, (row e) 50kRPM, 250ccm, (row f) 50kRPM, 500ccm cases.

the image (<25 pixel areas) were considered too small to be ligaments, so they were added to the droplet statistics. An example of the resulting raw and processed images for the serrated and unserrated cups can be seen in Fig. 2.6.

Finally, the ligaments and droplets were separated in the image and the cup edge was removed so that the fluid elements could be isolated and size statistics could be obtained. This was done by first identifying all connected components in the image. The largest of these connected components was always the cup edge and any connected ligaments. Due to this, ligaments in the image were identified as fluid elements attached to the cup. This largest component was then subtracted from the binarized image. With the cup edge and ligaments subtracted, only the droplets remained in the image. Thus, this would be the image from which droplet-only statistics would be derived. Then that largest component was placed in its own image and the cup edge was subtracted. The portion of the cup edge being captured in the image was small enough that the curvature of the cup could be approximated as a straight line, and therefore a straight line fit was applied to the edge to subtract off the edge of the cup and leave only the ligaments in the image. This image would be the one that the ligaments-only statistics were derived from.

2.2.3 Size Statistics

Once the images were finished processing, fluid size statistics were calculated in the same manner as the previous chapter, such that hydraulic diameters were calculated from areas and perimeters of objects determined from the processed images. Convergence was again checked to ensure that the sample size of 1500 images was adequate. Table 2.1 shows the image, out of the 1500, at which the sum of each of the distributions for the serrated and unserrated statistics converged to less than 5 percent difference from the

final distribution. As evidenced from the data, the droplet and combined data sets for both the serrated and unserrated bells converged quickly. The ligament data converged after a noticeably longer amount of images, but still before even half of the data had been used in even the slowest convergence case. Thus, all of the data can be said to have converged.

Table 2.1. The frame number for convergence of less than five percent for ligaments, droplets, and their combined statistics for each of the (a) serrated and (b) unserrated bell cases.

| | | Bell Speed [kRPM] / Flowrate (ccm) | | | | | |
		20/250	20/750	35/250	35/750	50/250	50/500
(a)							
Serrated	Ligaments	572	482	500	301	399	590
	Droplets	92	85	35	39	42	17
Image #	Combined	89	85	33	38	43	29
(b)							
Unserrated	Ligaments	406	737	279	494	254	174
	Droplets	71	137	21	44	17	23
Image #	Combined	75	130	22	42	17	23

2.3 Results and Discussion

2.3.1 Number Distributions

The number distribution for the ligaments in the serrated bell data showed two trends. The first trend was that as the flowrate was increased, hydraulic diameter increased. As rotational speed increased, hydraulic diameter decreased and a distinct bimodality in ligament size arises. Domnick et al.[51] also found these trends, albeit in a different region of the flow. In the ligament data for the unserrated bell cases, the trends of hydraulic diameter increasing with increasing flowrate and hydraulic diameters decreasing with increasing rotational speed also hold true. However, the bimodality is not present in any of the cases, which is also what was found previously [51], as well as the fact that the distributions become much narrower with increasing rotational speed. Such a

46

result implies that in this region as well, the dual mode of ligament and film formation, or whatever the explanation may be, exists. Furthermore, because this region is so close to the cup, it is unlikely that any flowfield recirculation effects or significant interference from the shaping air is present and affecting the data.

The droplet-only and combined number distributions in the serrated bell cases can be described concurrently due to their high similarity, which is a result of the bulk of the objects in an image being droplets. Depicted in Fig. 2.7 and Fig. 2.8, these distributions show the similar trends that as rotational speed is increased, the hydraulic diameters decrease and the distributions narrow. A distinct difference between these distributions and the ligament distributions is that change in flowrate does not appear to significantly influence the size of the droplets in this region. The hydraulic diameters appear, though somewhat weakly, to decrease with increasing flowrate, but such a result would need to be confirmed by the volume weighted size distributions to know for sure. As for the droplet-only and combined number distributions in the unserrated bell cases, which can also be concurrently discussed, the trend of decreasing hydraulic diameters with increasing rotational speed again appears. However, the flowrate trend, which is again fairly weak, is that as flowrate is increased, hydraulic diameter increases.
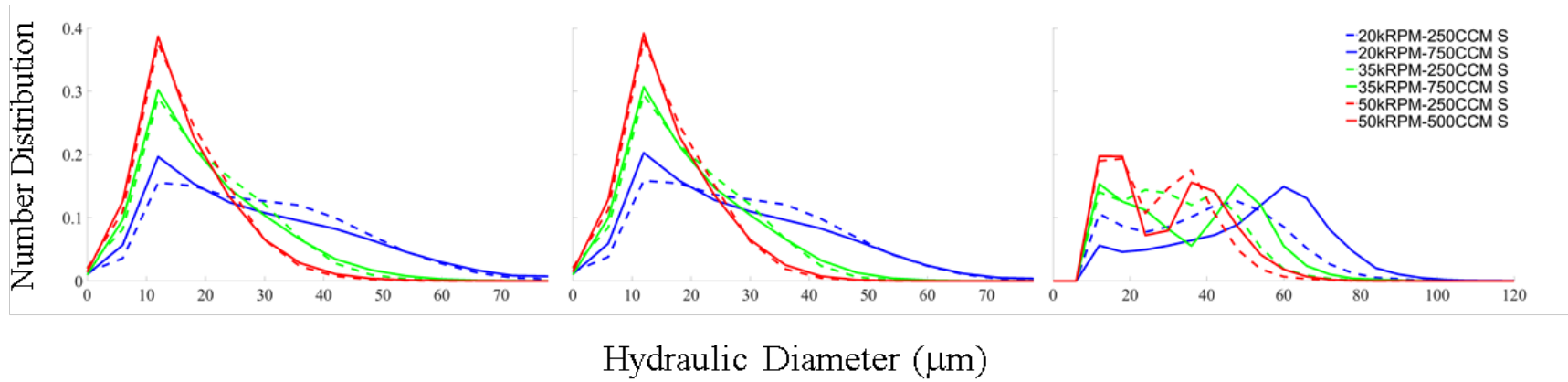
Figure 2.7. Number distributions, for the serrated bell, of the hydraulic diameters for all fluids (left) in an image, just the droplets (center), and just the ligaments (right).
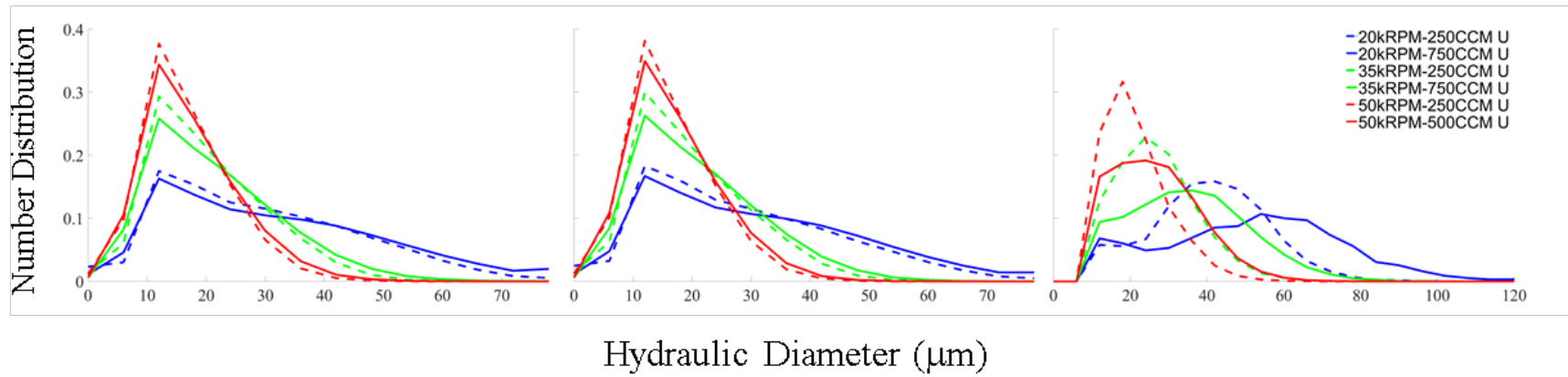
Figure 2.8. Number distributions, for the unserrated bell, of the hydraulic diameters for all fluids (left) in an image, just the droplets (center), and just the ligaments (right).

2.3.2 Volume Distributions

The volume distributions, depicted in Fig. 2.9 and Fig. 2.10, again reflect the trend of decreasing hydraulic diameter with increasing rotational speed. The information gained from these distributions, though, is that the increase in flowrate results in increased hydraulic diameter across for both the serrated and unserrated bells. Overall, these distributions also indicate that for droplet size, rotational speed is clearly the more dominant operational parameter, another result found previously [6,51]. Conversely, for ligaments, hydraulic diameter appears just as dependent on flowrate as on rotational speed, which to our knowledge has not been found previously.

2.3.3 Sauter Mean Diameters and Spans

The SMD data, as seen in Table 2.2, confirms the trends previously discussed of increasing hydraulic diameter with increasing flowrate and decreasing rotational speed. What this data now shows, however, is that the SMD for the unserrated bell cases are consistently higher than the serrated bell cases at equivalent operational parameters. Additionally, it shows that changes in flowrate affect the unserrated bell cases much more than the serrated cases. For example, the 20kRPM, serrated bell, droplet SMD increase between the high and low flowrate cases is 3.94% while for the identical unserrated bell case the increase is 9.08%. The percent differences, as well as the gap between percent differences, between same rotational speed, but differing flowrate, cases for the serrated and unserrated bells are even greater for the ligament data.
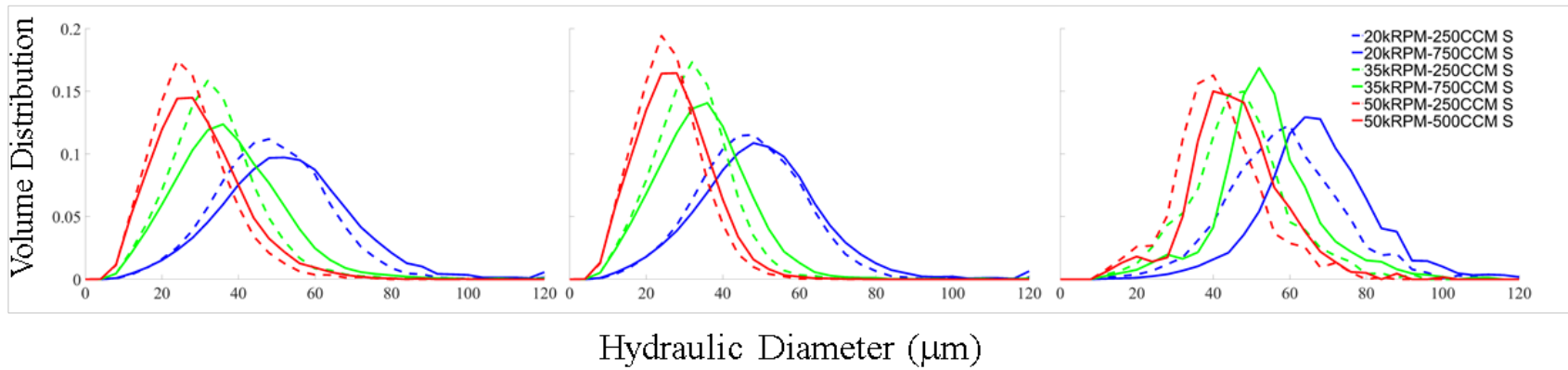
Figure 2.9. Volume distributions, for the serrated bell, of the hydraulic diameters for all fluids (left) in an image, just the droplets (center), and just the ligaments (right).
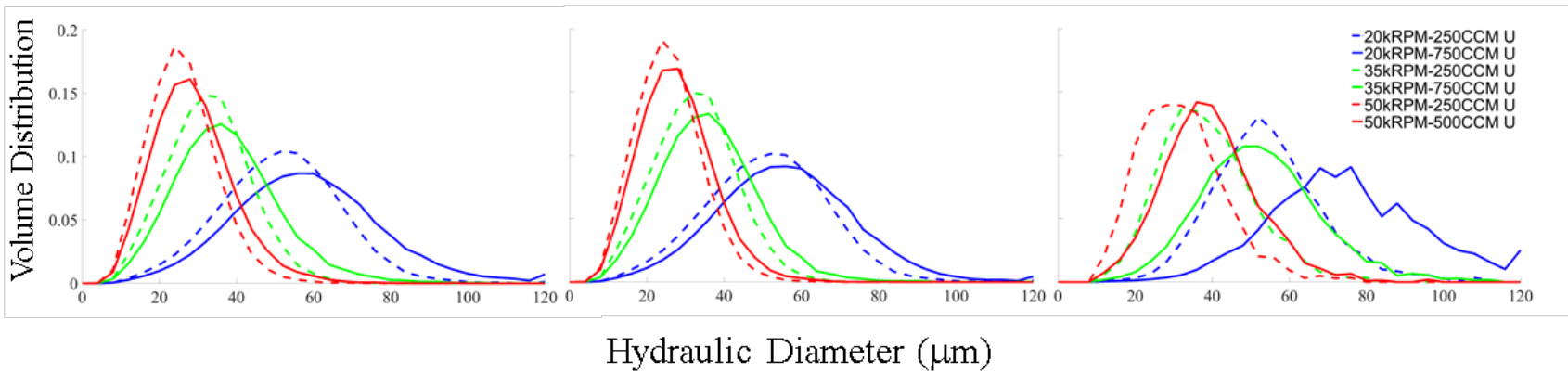
Figure 2.10. Volume distributions, for the unserrated bell, of the hydraulic diameters for all fluids (left) in an image, just the droplets (center), and just the ligaments (right).

Table 2.2. Fluid size D32 [μm] values for ligaments, droplets, and their combined statistics for each of the (a) serrated and (b) unserrated bell cases.

| | | Bell Speed [kRPM] / Flowrate (ccm) | | | | | |
		20/250	20/750	35/250	35/750	50/250	50/500
(a)							
	Ligaments	53.9	63.5	42.8	49.8	37.6	41.9
Serrated	Droplets	42.3	44.0	28.1	30.0	22.7	23.6
D_{32} **[μm]**	Combined	43.6	46.3	29.4	31.8	23.8	25.0
(b)							
Unserrated	Ligaments	50.4	69.3	34.7	47.6	28.3	35.5
D_{32} **[μm]**	Droplets	45.2	49.5	28.7	31.5	22.6	24.2
	Combined	45.8	51.5	29.1	32.6	22.9	25.0

The changes in rotational speed also affect the serrated bell ligament data more than the unserrated bell data. As an example, when increasing the bell speed from 35kRPM to 50kRPM at the 250ccm flowrate, the ligament SMD decrease is 37.6% for the serrated bell, but is only 28.3% for the identical unserrated cases. The differences for the droplet and combined SMD data in these cases is minimal, though. Such a result implies that the serrations are producing smaller ligaments than the atomization process would otherwise produce without them. However, a more complete description would include the information from the number distribution data where it is clear that there are two regimes of ligament sizes in the serrated bell cases; only one of which appears to change significantly with rotational speed.

The span data, used to numerically confirm relative distribution widths and seen in Table 2.3, displays trends that are not so definitive. First, when it comes to the droplet and combined fluid statistics in this near-field region, the spans do not vary significantly between the serrated and unserrated bell cases. Additionally, both the serrated and unserrated data for these cases shows an increase in span as flowrate is increased and as

rotational speed is increased, despite the fact that the distributions would appear to indicate the opposite.

When it comes to the ligament data, the trends are different for the serrated and unserrated bell cases. For the serrated ligament distribution widths, there is an increase with increasing rotational speed, followed by a slight decrease. Conversely, for the unserrated ligament distribution span, there is a steady increase. This resulting difference may be due to the bimodality of the ligament sizes for the serrated case. Additionally, for the serrated bell cases, the ligament span decreases with increasing flowrate. This, while for the unserrated bell cases, the ligament span increases with increasing flowrate for the 20,000 RPM case and then decreases in the higher rotational speed cases. These results again contradict what the distributions appear to indicate, and would seem to show that there may be a regime transition, namely ligament to direct drop or film formation, within these operational parameters that effects the uniformity of ligament size for the unserrated case that may be counteracted somewhat by the serrations.

Table 2.3. Fluid size span values determined from the volume weighted size statistics for ligaments, droplets, and their combined data for each of the (a) serrated and (b) unserrated bell cases.

		Bell Speed [kRPM] / Flowrate (CCM)					
		20/250	20/750	35/250	35/750	50/250	50/500
(a)							
Serrated Spans	Ligaments	.628	.532	.698	.573	.689	.627
	Droplets	.748	.808	.779	.869	.868	.920
	Combined	.750	.829	.850	.950	.961	1.04
(b)							
Unserrated Spans	Ligaments	.653	.697	.813	.743	.883	.802
	Droplets	.774	.806	.826	.867	.861	.886
	Combined	.759	.833	.829	.915	.875	.927

2.3.4 Ligament Lengths and Widths

The final size parameters measured were the ligament lengths and widths. As can be seen in Fig. 2.11 (lengths) and Fig. 2.12 (widths) for the unserrated and serrated bell, a few trends can be observed. In the ligament lengths data, it can be seen that as rotational speed is increased, the distributions become narrower and shift towards smaller ligament lengths. This trend is true for both the serrated and unserrated bells. In the unserrated bell ligament data, decreasing flowrate also shifts the distributions towards smaller ligament lengths. These results, as has been previously discussed with the hydraulic diameter data, are expected. However, a notable result is that for the serrated bell data, change in flowrate, while shifting towards smaller ligament lengths with lower flowrates for the 20kRPM case, does not affect the distributions for the 35kRPM and 50kRPM rotational speed cases. Such a result suggests that the serrations, the only parameter that changes between the two data sets, limit the natural size evolution of the ligaments by channeling the flow near the edge of the bell. It also suggests that the channeling of the flow directly influences the effect of flowrate changes on the ligament size distributions.

In regards to the ligament widths, there exists the similar trend to the ligament lengths, in the unserrated case, that increasing rotational rate results in a shift to smaller ligament widths. Likewise, for the unserrated case, decrease in flowrate results in a decrease in ligament widths. However, for the serrated bell data, while an increase in rotational rate results in a shift to smaller ligament widths, decreasing rotational rate has negligible effect at all rotational speeds. This result supports the ligament length result, which suggests that serrations make the overall ligament sizes more uniform than they otherwise would be at these operational parameters.
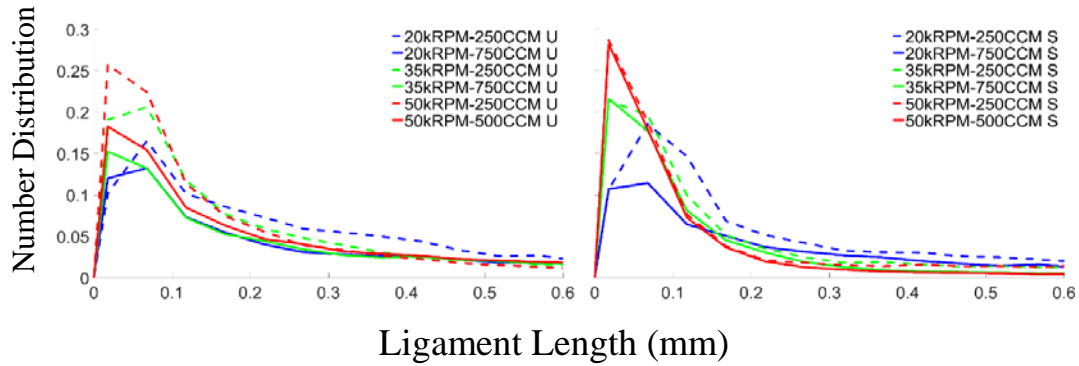
Figure 2.11. Ligament length number distributions for the unserrated (left) and serrated (right) rotary bells. Each color corresponds to a particular rotational speed with blue for 20kRPM, green for 35kRPM, and red for 50kRPM. Within the rotational speeds, the dashed line corresponds to the lower flowrate case, while the solid line data corresponds to the higher flowrate case.
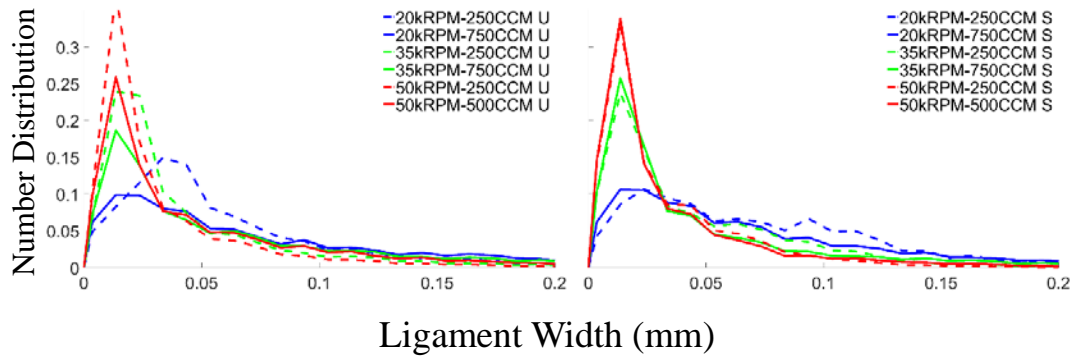
Figure 2.12. Ligament width number distributions for the unserrated (left) and serrated (right) rotary bells. Each color corresponds to a particular rotational speed with blue for 20kRPM, green for 35kRPM, and red for 50kRPM. Within the rotational speeds, the dashed line corresponds to the lower flowrate case, while the solid line data corresponds to the higher flowrate case.

2.4 Conclusion

A shadowgraph imaging experiment, which utilized laser pulse background light to minimize the exposure time and gain clearly resolved fluid particle profiles, was conducted as a follow-up to the high-speed imaging in Chapter 1. This alternative method

was necessary to capture clearer images at higher rotational speeds possible with a different rotary bell atomizer. This method could be used in future experiments as a means for studying this region of a rotary bell atomizer at such high rotational speeds. Three different rotational speeds and a high and low liquid flowrate were tested for two nearly identical bell-cups that varied only in the fact that one had a serrated edge and the other did not. Approximate, and typical for droplet research, size statistics on the near-field region just off the cup-edge of a rotary bell atomizer, just as before, were obtained to study any effects of the different operational parameters and of serrations. These size statistics consisted of histograms of the hydraulic diameters, comprising of number and volume distributions, SMDs, and spans. Combined, these statistical representations of the processed image data aided in providing a comprehensive description of various trends arising from the variation of the parameters in the experiment.

The results from the processed image data revealed both expected results and helped to confirm other previously seen trends, in that they matched what had been found further downstream in this atomization process. Ultimately, what was found was that, for both the serrated and unserrated bells, hydraulic diameters of the both the ligaments and droplets in the still images increased with increasing flowrate and decreasing rotational speed. However, though the direction of the trends for both of the bells is similar, the rate of change for the same variation of operational parameters was not. The effect of rotational speed is more impactful on the serrated bell cases. Both bells also showed rotational speed as the more dominant parameter for droplets, though, despite using high flowrate parameters. Conversely, ligament sizes where much more dependent, relative to the droplets, on flowrate.

The volume distributions show a general decrease in distribution width with increasing rotational speed and with increasing flowrate across all cases. However, the span data shows a more complex story. For the serrated ligament distribution widths, there was an increase with increasing rotational speed, followed by a slight decrease, while for the unserrated ligament distribution span, there is a steady increase. The cause is uncertain for this difference. For the serrated bell cases, the ligament span also decreases with increasing flowrate, while for the unserrated bell cases, the ligament span increases with increasing flowrate and then decreases in the higher rotational speed cases. These results contradict what the distributions appear to indicate, and would seem to show that there may be a regime transition that may be subdued by the serrations, or the conflicting results may indicate that the span may not be a suitable parameter to summarize the hydraulic diameter distributions presented numerically.

Finally, the ligament length and width data aid in confirming the trends that arise in the number and volume distribution data. The ligament lengths and widths for the unserrated bell show the expected result of a decrease in ligament length and width with decreasing flowrate and increasing rotational speed. However, they also show that for the serrated bell, the ligament lengths and widths do not vary significantly with changes in flowrate, though changes in rotational speed. These results, in combination with the hydraulic diameter distribution data, collectively show that the serrations make ligament sizes more uniform for variations in flowrate. They also show that they may be creating an unintended bimodal distribution in ligament formation. Further investigation is needed into the downstream consequences of this result.

CHAPTER THREE: DEFECT INVESTIGATION OF ROTARY BELL ATOMIZER
THROUGH PROPER ORTHOGONAL DECOMPOSITION OF HIGH-SPEED IMAGE
DATA

3.1 Introduction

Proper orthogonal decomposition is a mathematical technique that reduces the order
of the model that it is applied to. The origin of POD as a mathematical tool dates back to
Kosambi[58], who found that various processes could be expressed in terms of a small
number of Fourier coefficients[59]. Later, Lumley[60] would be the first to apply the
technique to turbulent flows in a study of fluid motion. Subsequent study would be done
in computational fluid dynamics to reduce the order of models[61] and find coherent
structures in turbulent flows[62]. A comprehensive explanation of the technique has been
published many times over, and the reader is referred to Tabib and Joshi[63] for a
thorough background on various fluid flow studies that the technique and its derivatives
have been applied to. Additionally, Walton et al.[64] presents a detailed explanation of
the purpose, structure, implementation and history of POD in fluid dynamics.

This thesis will give a very brief explanation of the fundamentals of the technique as
it relates to how it was applied in this study. Two-dimensional experimental image data
was deconstructed by POD into spatial modes. The total solution set of modes represents
the set of basis functions. When applied to a problem, the goal is to find the smallest
possible set of these functions or modes which, when combined, reconstruct most of the
flow or a specific aspect of it that is being investigated. Because the process uses singular
value decomposition (SVD), the eigenfunctions, or modes, are pre-ordered. That is to

say, the modes are automatically output based on modal energy, or relative importance/contribution to the entire data set. This means that the most dominant aspects of the flow will be the first few modes. The numerical average of the image data is often the first mode, and due to this fact, is typically ignored unless relevant. Mathematically, this can be represented in the following way, from Kopp-Vaughan et al. [65]. Given an original temporal dataset (sequence of images), OD_j^t, which denotes pixel intensity values at spatial location j and time t, an SVD is performed to get an orthogonal bases set. This allows the dataset to be described by (4)

$$OD_j^t = \sum_{i=1}^{M} a_j^i v_i^t + \langle OD_j^t \rangle \tag{4}$$

where a_j^i represents the bases (or modes) and v_i^t represent the eigenvectors (or constants), which serve as a weighting value to indicate the relative contribution of the associated mode to the dataset as a whole at each time step.

The constants demonstrate how dominant a mode is in each image, and when plotted temporally, demonstrate the fluctuation of that mode's importance. This information can be used to identify the specific points in time, assuming a mode represents a flow feature, that the flow is experiencing said feature. The fluctuations of the constants over time themselves also provide some information about the flow process. By performing a Fourier analysis on the constants data, dominant frequencies can present themselves and give information about periodicity of flow features and the modes that represent them. This study mainly focuses on this element of POD analysis, due to the cyclical nature of the rotary bell.

POD has often been used on less dynamical fluid systems such as the flow field of a plane jet[66], a liquid jet in crossflow[67], a co-axial jet[68], and even a laminar separation bubble[69]. POD has also been used on many swirling/rotating fluid systems to identify dominant features in those processes. This has been the case for swirling systems in the combustion field in attempts to extract data on flame dynamics that might be lost through other approaches[65,70,71], occasionally in combination with other techniques like Large Eddy Simulation (LES)[72]. In other non-combustion systems, the vortex dynamics of a circular cylinder[73] and the instabilities of decelerated swirling flows have also been investigated.

Due to its usefulness in identifying the dominant features of a dynamic process, it was chosen as a method of analysis for examining changes in rotary bell atomization under varying conditions in the following experiment. Presumably, such a decomposition would be able to reveal the modal changes in the process, both near the cup and in the flow field (plume) during the atomization process. However, rotary bell atomization is a process that occurs very quickly with tens and hundreds of thousands of complete rotations of the bell-cup per minute. To capture time-correlated data, like that which is necessary to utilize proper orthogonal decomposition, equipment with the high data acquisition speed is necessary. In the following experiment, a high-speed camera is used to capture the detailed flow processes of the atomization in combination with the modal decomposition technique to find the dominant changes across different operational parameters and different types of cups.

In order to test this, a few methods of variation were tested to see what kinds of differences could be captured by this technique. Two bell-cups, identical except that one

59

was given some external damage, were tested across varying rotational speeds and flowrates. Doing so reveals the effectiveness of the modal decomposition to identify such changes in a production context. The frequency data gained from the constants of the principal modes should change with changing parameters, and the investigation of what changes arise is the aim of this thesis. Results that reflect clear differences in the image data would mean that POD could be used as an effective tool to define whether or not a rotary cup in a paint booth is performing efficiently or has been damaged/worn to the point that it should be removed from production. This method is also performed very quickly and does not require expensive equipment, meaning that testing would also be fast and cheap or could even be performed on bells during their regular operation.

3.2 Methods and Materials

3.2.1 Experimental Setup

A diagram of the experimental setup can be seen in Fig. 3.1. A Dürr Ecobell2 rotary bell atomizer was used along with water as the fluid being fed through and transported by the system. Two different 55 mm bell cups were utilized and interchanged throughout the experimentation to observe any changes in the Fourier analysis of the mode constants with changing parameters. The cups were identical in geometry and material, except that one was externally damaged, seen in Fig. 3.2. Using a hammer, external damage was given to both the side of the cup, as well as at the cup edge, flattening a portion of it somewhat, seen in the bottom right image of Fig. 3.2. The level of damage imparted was done such that it would be comparable to the condition that would result from someone accidentally dropping a cup or if the cup hit an object during operation. The variation in

condition was done to observe any flow differences that could be attributed to cup

damage and show that POD analysis could be used to capture those differences. Three

rotational speeds (20,000 RPM, 35,000 RPM, and 50,000 RPM) and two flowrates (250

ccm and 750 ccm) were varied for each of the different cups as well. This would allow

for differences caused by fluctuations in operational parameters to also be observed.

Additionally, a case without the bell operating and a case with the bell rotating, but no

fluid being sent through the system were run to identify any background frequencies, so

that they could be discerned from meaningful data,. The no-fluid case, which was only

run at the 20kRPM rotational rate, was run to identify vibrational mode data independent

of flowrate, and to see if the method could be useful in identifying analyzing a cup with

no paint running through it.
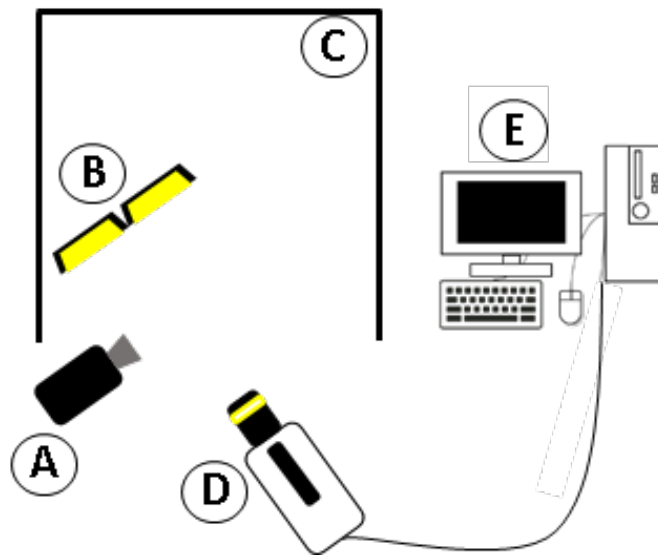
Figure 3.1. POD experimental setup with rotary bell atomizer (A), LED illumination source (B), hood (C), camera and lens setup (D), and computer (E).
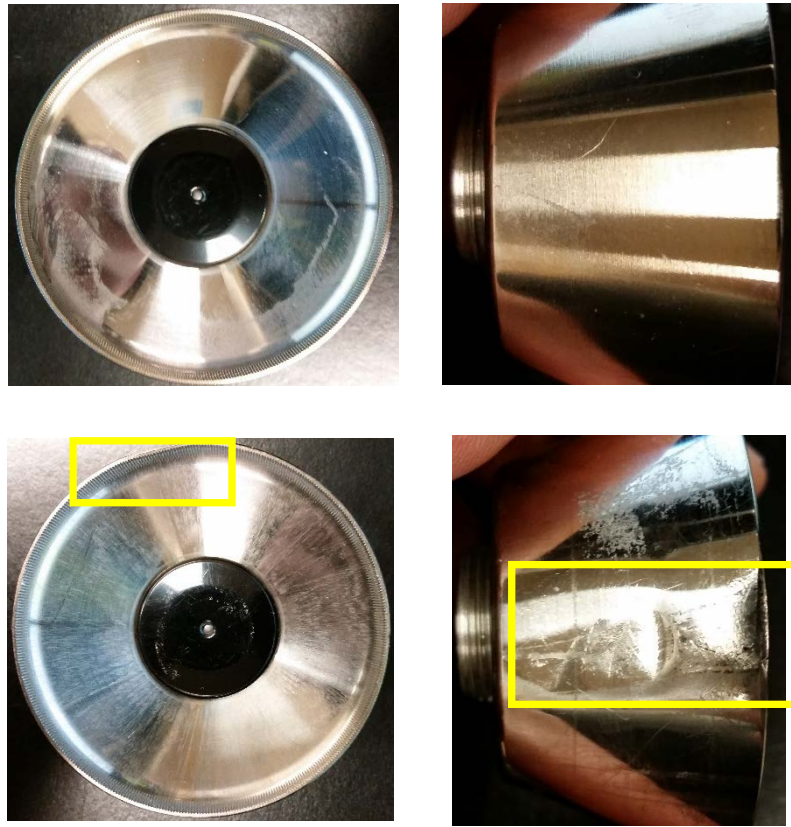
Figure 3.2. Undamaged cup from (top left) front and (top right) side view along with damaged cup from (bottom left) front and (bottom right) side view for comparison.

As for the optical setup, two 12 VDC output LED lamps were covered with a diffuser and were used as the light source and a Phantom V611 CMOS camera equipped with an f = 105 mm Sigma lens was used to image the atomization process. Seen in Fig. 3.1, the camera was placed normal to the direction of the flow, since the transient characteristics of the flow in this direction were of interest. The acquisition rate of the camera was set to 6022 Hz, which is a double of a prime number, so that aliasing could be more readily identified in the Fourier analysis. The frame size utilized was 1200×800 pixels and the exposure time was 160 μs. 3011 frames, which is .5 seconds or 333-833 full cup rotations (depending on rotational rate) of data was captured.

3.2.2 Image Decomposition

The POD analysis consisted of running a MATLAB script that utilized matrix reshaping and the built-in SVD script on the image data sets. The particular description of the formulation used in this experiment of the eigenvectors and eigenvalues derived from the image data is described succinctly in Kopp-Vaughan and Renfro[65]. The convention referenced in that article about modes being considered principal modes only where the energy is greater than 1%, as suggested by Berkooz et al.[61], was also utilized as a starting convention for this study. Some of the relevant MATLAB scripts for this process can be found in the Appendix.

The data selection process influences what kinds of modes will be produced by POD. For example, in a multi-stage process, getting modes from each stage would produce the modes that describe each respective stage very well. However, taking the modes of the entire process may not reveal modes that describe any of the individual stages. Despite this possibility, what was done in this work was to take the damaged cup data in its entirety and find the modes for the whole data set. Likewise, the undamaged cup data was taken in its entirety, for each case, and modes were found for the entire data set. Following the acquisition of the modes for each data set, the constants were found. The constant data was found for not only each respective set, but across sets to the other cup. In other words, the relative importance of each mode (constants) in each frame of the damaged cup, was found for both the damaged cup data set and the undamaged cup data set. This was done to further investigate the differences in the modal data from each dataset.

Originally, the full frame data was used to attempt to find flow structures, however much of the plume mode data of the atomization process did not give distinct frequency content. In addition to giving unclear results, the full frame data was also computationally large, and would often not complete before crashing the MATLAB program if all of the frames were included in the data set. Some investigation into which aspects of the full frame data would produce more distinct frequency content was done to counter this problem so that the data set would not be as large. One aspect of the process that did produce well-defined frequency content, and that varied across cases, was some oscillatory behavior near the bell cup. Upon recognition of this information, the frame was cut to a 220×100 pixel window that included only a small area around the cup, seen in Fig. 3.3. Focusing on this reduced window produced modes with more distinct frequency spectra, seen in Fig. 3.4. Finally, the frequency spectra data was plotted as normalized power spectral density data, using (5)

$$PSD * (f) = \left| \mathcal{F}\big(u(t)\big) \right|^2 \tag{5}$$

which calculates the power spectral density given a time series $u(t)$ [74]. The data was then normalized by the sampling rate, S (or 6022 Hz), the number of samples, N (or 3011 frames), and the signal variance, σ^2 so that the sum of the data in each mode's PSD would be a value of one.

$$PSD(f) = \frac{1}{N \cdot S} \frac{\left| \mathcal{F}\big(u(t)\big) \right|^2}{\sigma^2} \tag{6}$$

This was done because the Fourier plots of the constant data had amplitudes dependent on the modal energies. This meant that the more dominant modes would have considerably higher amplitudes and lesser modes would be difficult to accurately

64

compare at the same scale. Normalizing this data allowed for direct comparison,

regardless of original modal energies.
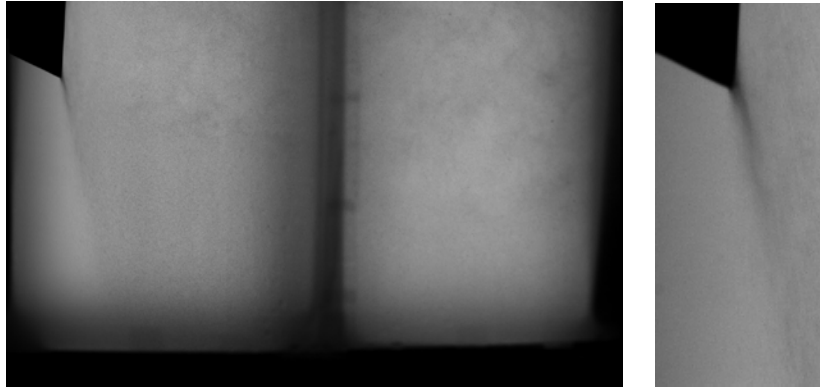
Figure 3.3. Full-frame image (left) and its resulting near-cup image (right) after an imposed cut of the frame for the damaged bell, 20kRPM-750CCM case.
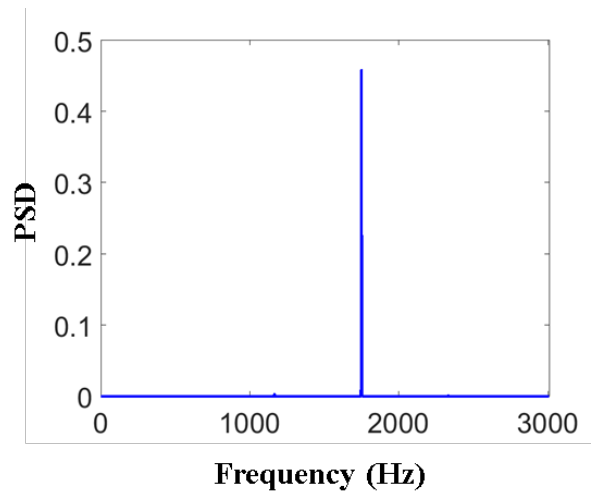
Figure 3.4. Power spectral density plot for mode 1 of the damaged bell run at 35kRPM with a 250CCM liquid flowrate. The peak located at 1750 Hz is approximately three times the bell rotational rate.

3.3 Results and Discussion

3.3.1 Modal Energies

The first aspect of the POD analysis to examine is the modal energies, or relative importance of each mode, in the overall image data set. For the undamaged and damaged bells, each of the first 10 modes and their energies were plotted in Fig. 3.5 and Fig. 3.6, respectively. As a first comparison between the undamaged and damaged bells, it is noticeable from the two figures that the approximate modal energies, when compared to the same case from the other bell, are very similar. Additionally, the modes with the lowest modal energies are the cases with no flowrate (Fig. 3.5a-b and Fig. 3.6a-b). This should be expected since there are no translational dynamic processes occurring in the image data for these cases such that, with the average removed from the image, very little remains. The modes with the highest modal energies are the cases with the lower flowrate (Fig. 3.5e,g, and Fig. 3.6e,g), with the exception of the 20kRPM (Fig. 3.5c and Fig. 3.6c) case where the difference is negligible. This result indicates that too much flow in the system introduces enough turbulent data that some structures become less dominant in the image data. In the following section, the mode shapes are examined. However, to make the results more concise, a slightly different convention than the previously mentioned 0.01 modal energy value will be used.

3.3.2 Mode Images

In the following sections, only the first six modes, or modes that exceed 0.01 modal energy, whichever results in the fewest modes, will be considered in the interest of condensing the results. Using this convention, the relevant mode shapes were selected

66
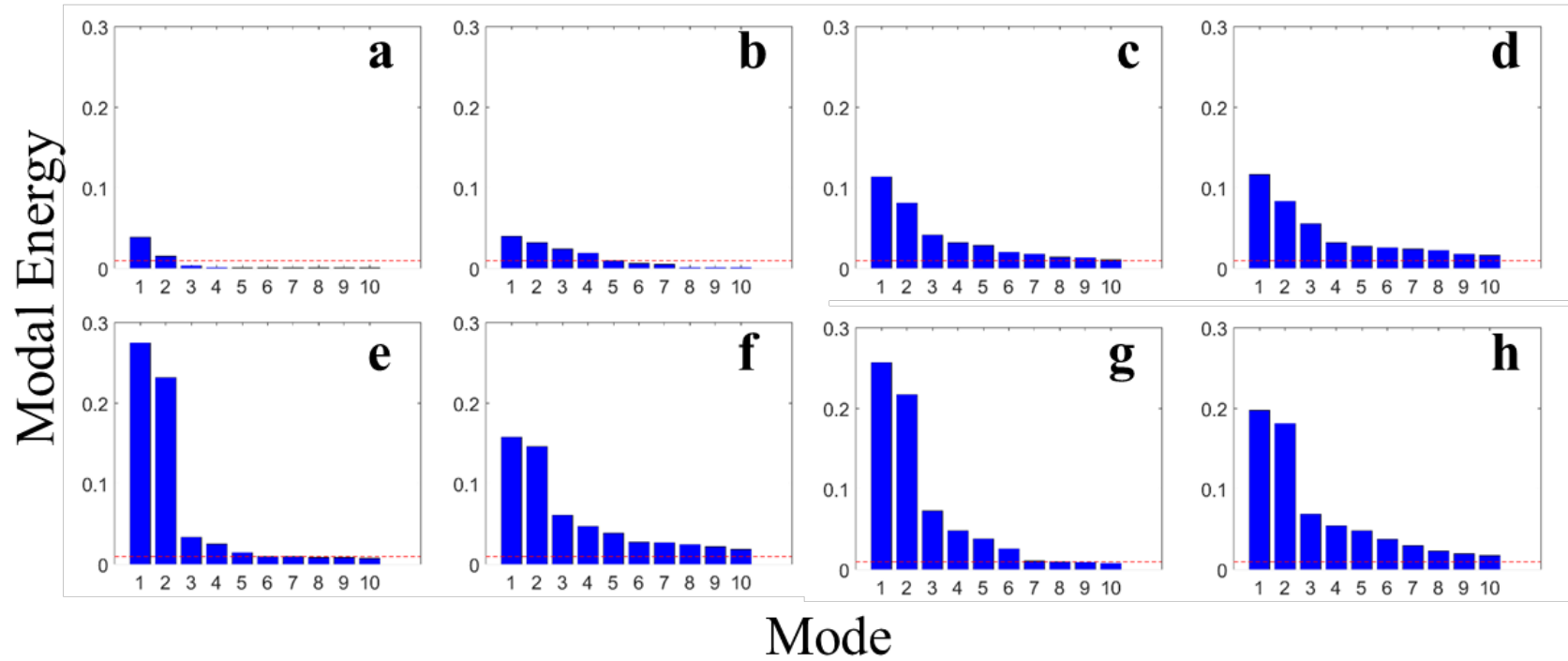
Figure 3.5. Undamaged bell modal energies for the first 10 modes in the (a) Background, (b) 20kRPM without flow, (c) 20kRPM-250CCM, (d) 20kRPM-750CCM, (e) 35kRPM-250CCM, (f) 35kRPM-750CCM, (g) 50kRPM-250CCM, and (h) 50kRPM-750CCM cases.
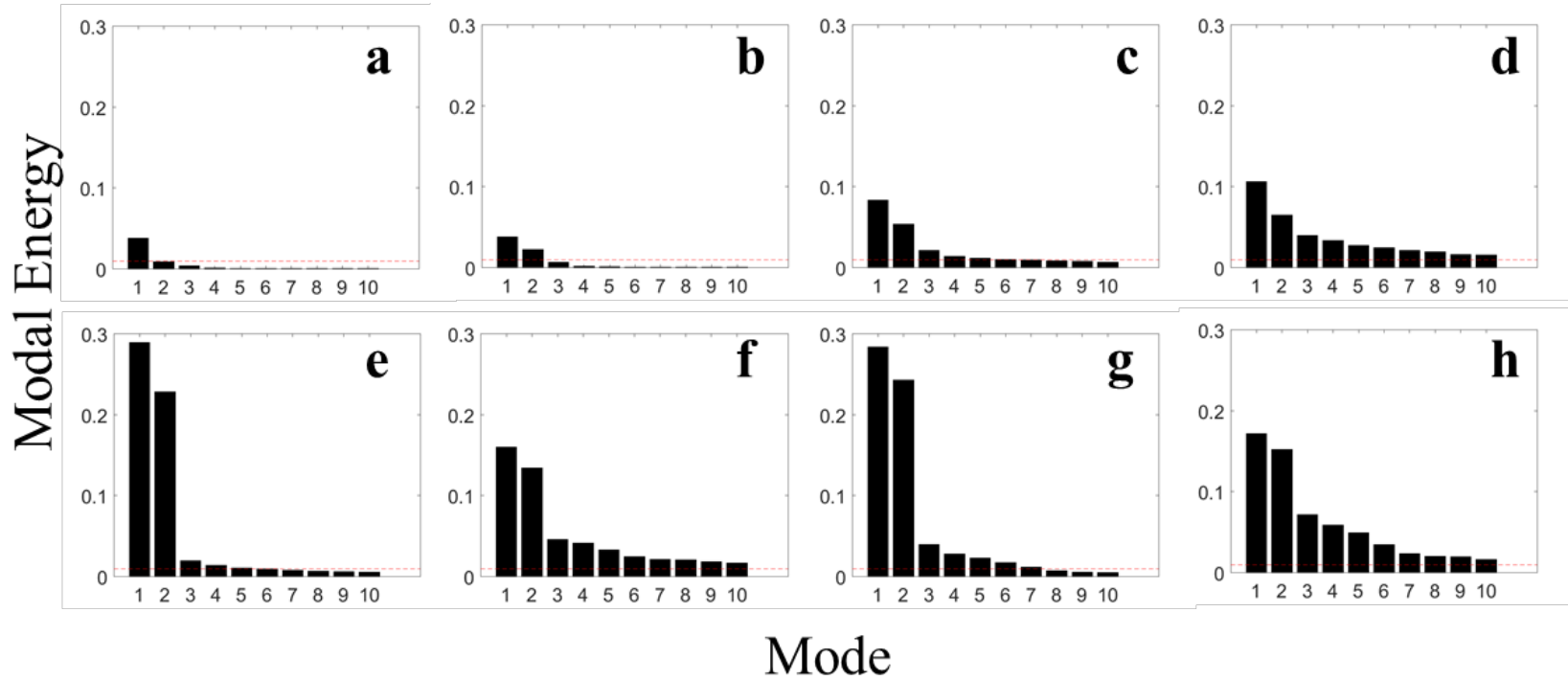
Figure 3.6. Damaged bell modal energies for the first 10 modes in the (a) Background, (b) 20kRPM without flow, (c) 20kRPM-250CCM, (d) 20kRPM-750CCM, (e) 35kRPM-250CCM, (f) 35kRPM-750CCM, (g) 50kRPM-250CCM, and (h) 50kRPM-750CCM cases.

from the data for each case and can be seen in Fig. 3.7 for the damaged bell and Fig. 3.8

for the undamaged bell. In the damaged bell data, for the background modes (Fig. 3.7a),

the data should only have the average image data be its determining mode, and any

additional modes may be from any innate frequencies of the illumination source. With the

average mode subtracted, the two modes that are shown appear to indicate that such a

background fluctuation exists, and looking into the spectral data would confirm this fact.

The 20kRPM case with no flow (Fig. 3.7b) shows sharp contrast between black and white

near the edges of the cup, indicating translation in the data set. Since the cup does not

actually move, this translation can be attributed to vibration of the cup. Looking into the

spectral data for these modes should give a clearer indication as to what exactly the

vibration is a result of. For the 20kRPM-250CCM case (Fig. 3.7c), the modes begin to

reflect the fluid dynamics around the edge of the cup during atomization. Modes 1 and 2

for this case appear to show translation from the top of the cup to the bottom, as well as

propagation of the liquid away from the cup. The frequency content of this translation

would thus be predicted to be resonant with the rotational rate of the cup. Modes 3 and 4

of this case just show the translation near the bottom of the cup, possibly representing the

transition of the fluid from going in the downward direction to moving back up or some

fluid shedding at the bottom of the cup. Modes 5 and 6 appear to show more of the

translation/propagation, but seem to be much closer to noise in the image data. All of the
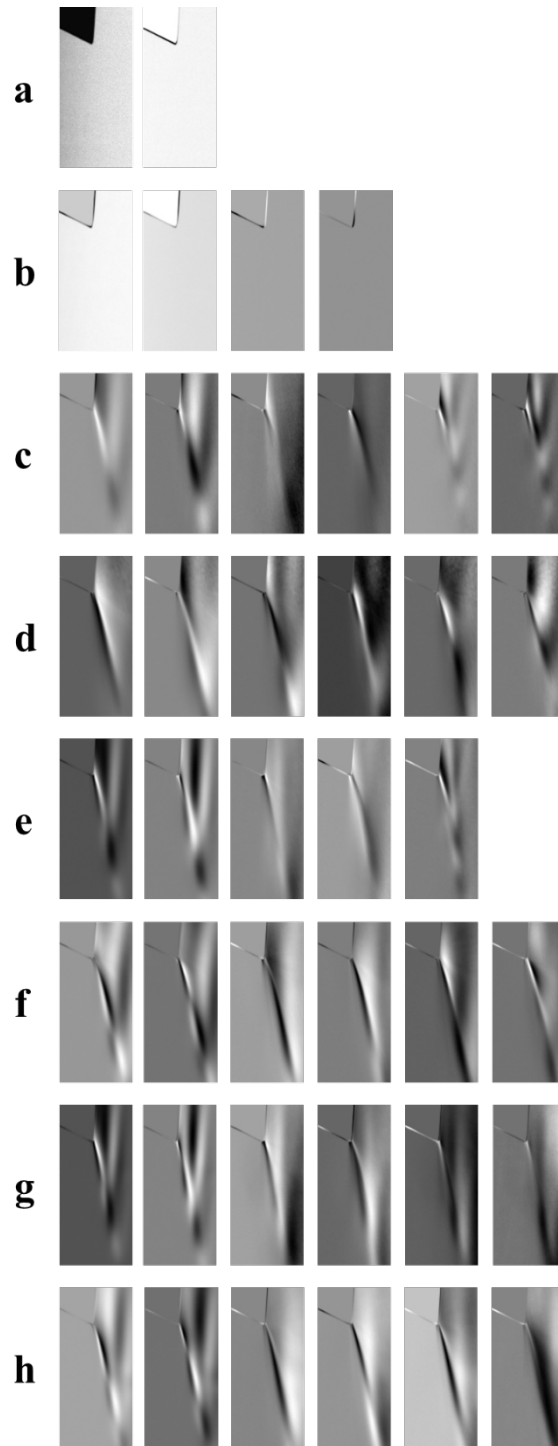
Figure 3.7. Damaged bell mode images for relevant modes in the (a) Background, (b) 20kRPM without flow, (c) 20kRPM-250CCM, (d) 20kRPM-750CCM, (e) 35kRPM-250CCM, (f) 35kRPM-750CCM, (g) 50kRPM-250CCM, and (h) 50kRPM-750CCM cases.
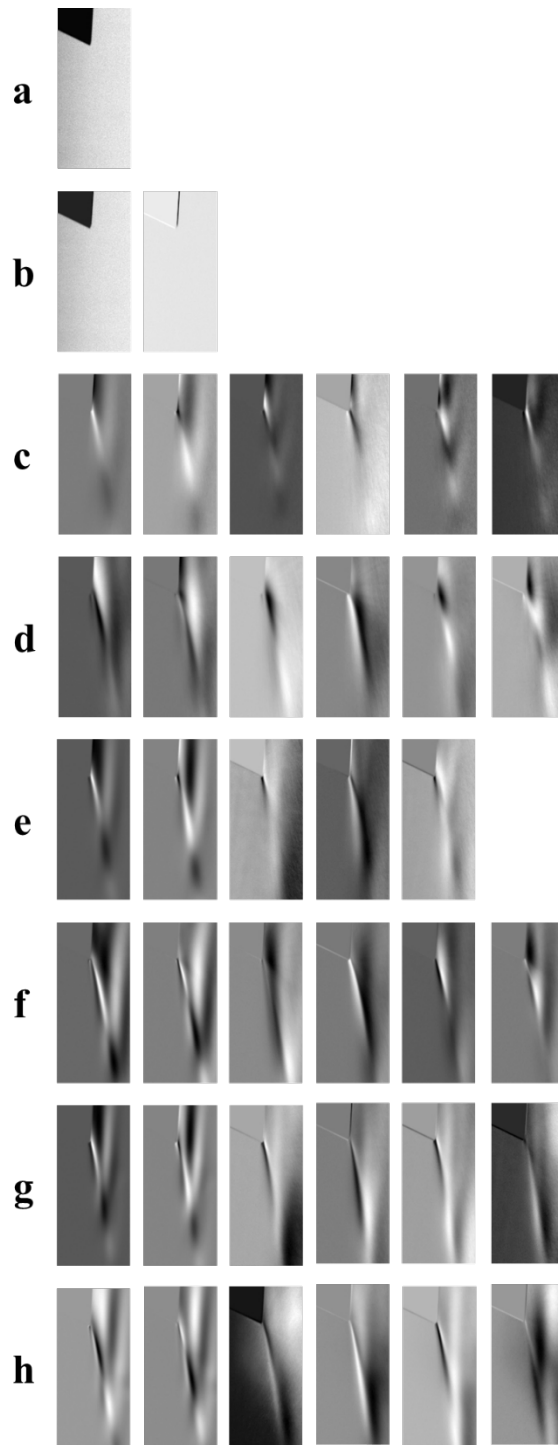
Figure 3.8. Undamaged bell mode images for relevant modes in the (a) Background, (b) 20kRPM without flow, (c) 20kRPM-250CCM, (d) 20kRPM-750CCM, (e) 35kRPM-250CCM, (f) 35kRPM-750CCM, (g) 50kRPM-250CCM, and (h) 50kRPM-750CCM cases.

modes, however, appear to show some vibration underneath of the cup. For the 20kRPM-750CCM case (Fig. 3.7d), the modes are slightly different. The first five modes of this data set appear to show the translation, but less of the propagation of the fluid. The propagation, however, is prominently featured in the sixth mode of this case and all of the modes have some inclusion of cup vibration. The 35kRPM-250CCM case (Fig. 3.7e) has its first two modes featuring the propagation as a dominant feature, and the subsequent next two modes featuring the translation at the transitional point of the cup. The fifth mode of this case appears to just be noise and all of the modes again show some cup vibration. In the next mode series depicted, or the 35kRPM-750CCM case (Fig. 3.7f), the first two modes again show a combination of the translation and propagation of fluid. Modes 3-6 just reflect the translation, and the cup vibration is present throughout all of the modes. For the 50kRPM-250CCM case (Fig. 3.7g) and the 50kRPM-750CCM case (Fig. 3.7h), the modal data can abstractly be described as very similar to the 35kRPM-750CCM case (Fig. 3.7f).

Overall, the undamaged bell cup data is very similar to the damaged cup mode data, with a few subtle differences. First, the 20kRPM with no flow case (Fig. 3.8b) has fewer relevant modes than for the damaged case, and the damaged case relevant modes were all cup vibration, whereas the background mode is the dominant mode in the undamaged mode data. Additionally, many of the modes look very similar in the damaged and undamaged data sets (see Fig. 3.7e,g and Fig. 3.8e,g modes) when the flowrate is lower. There are several differences that can be seen, though. The modes dominated by translational movement near the transition point of the cup show much sharper edges of the translation for the damaged data set over the undamaged data sets. An example of this

is the difference between the modes for the 35kRPM-750CCM cases (Fig. 3.7f and Fig. 3.8f). In the 50kRPM-750CCM case (Fig. 3.8h) for the undamaged data set, a mode appears (Mode 3) that appears to show background noise as it is the only mode that has any considerable variation underneath of the cup that is not vibration. The final noticeable difference in the mode shapes is that the undamaged data does not have nearly as much vibrational contribution. For many cases, the first two modes show no cup edge, indicating no contribution from cup vibration in the mode.

Therefore, in reference to the goal of this study, there are a few preliminary indications that could be given just from the modal data that a cup may have experienced adequate damage to impair its functionality. The damaged cup in this study appears to show more vibrational modes around the cup, and has sharper translational modes across operational parameters. Additionally, if tested without any flow, the dominant modes will be vibrational modes for the damaged cup, but not for the undamaged cup. Due to the vibrational contribution to the modes, background modes will not appear in the first few modes for the damaged cup, but may appear for an undamaged cup. Investigation into the frequency data should give further preliminary indications.

3.3.3 Power Spectral Density Data

The corresponding power spectral density (PSD) data was calculated for the constants of the modes previously presented in this work. The results of the calculations are plotted for the damaged bell in Fig. 3.9 and the undamaged bell in Fig. 3.10 and laid out such that the plots can be easily compared to their modal shape counterparts for the equivalent cases. It is also worth noting that the y-axis is the amplitude of the normalized PSD and

Frequency (Hz)
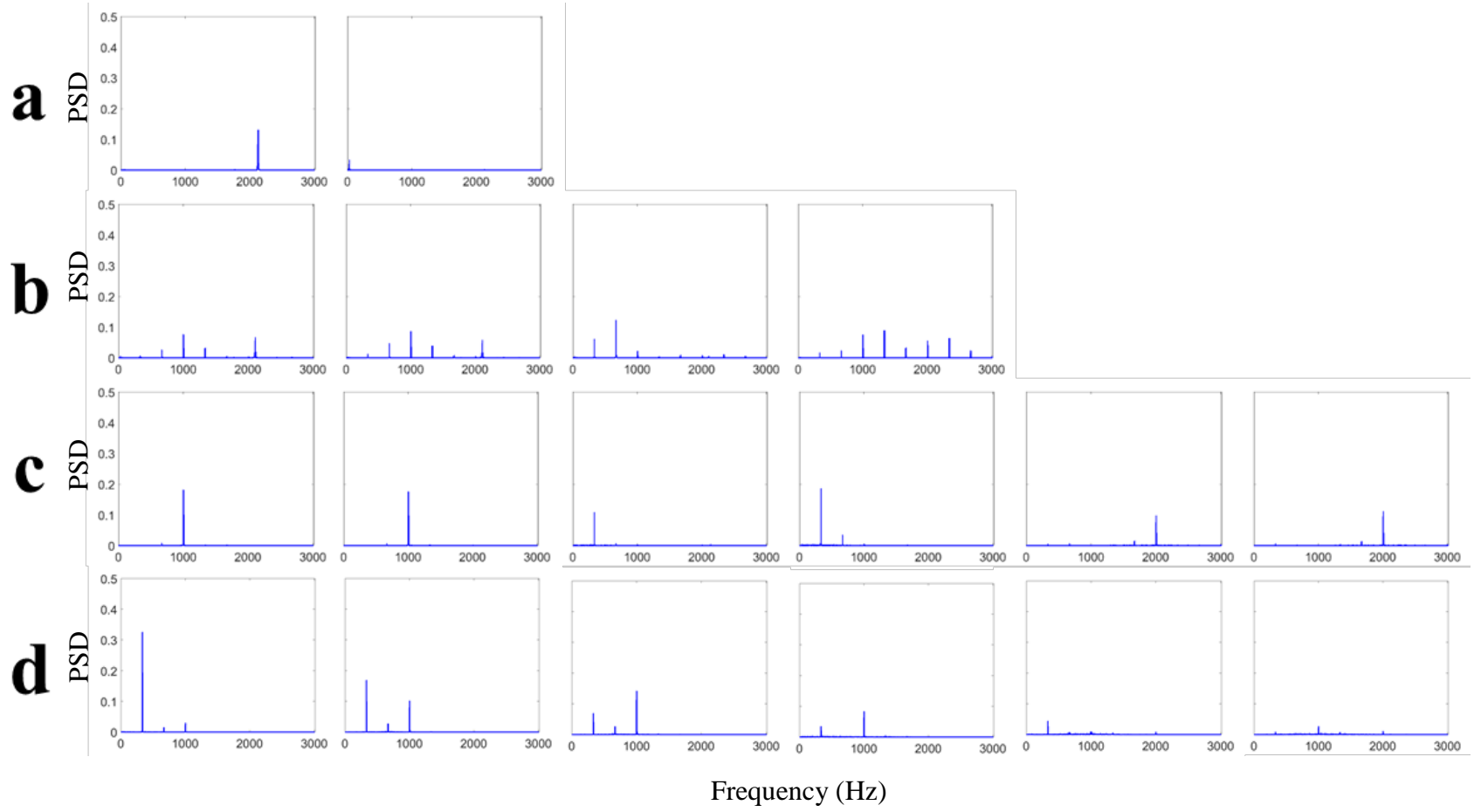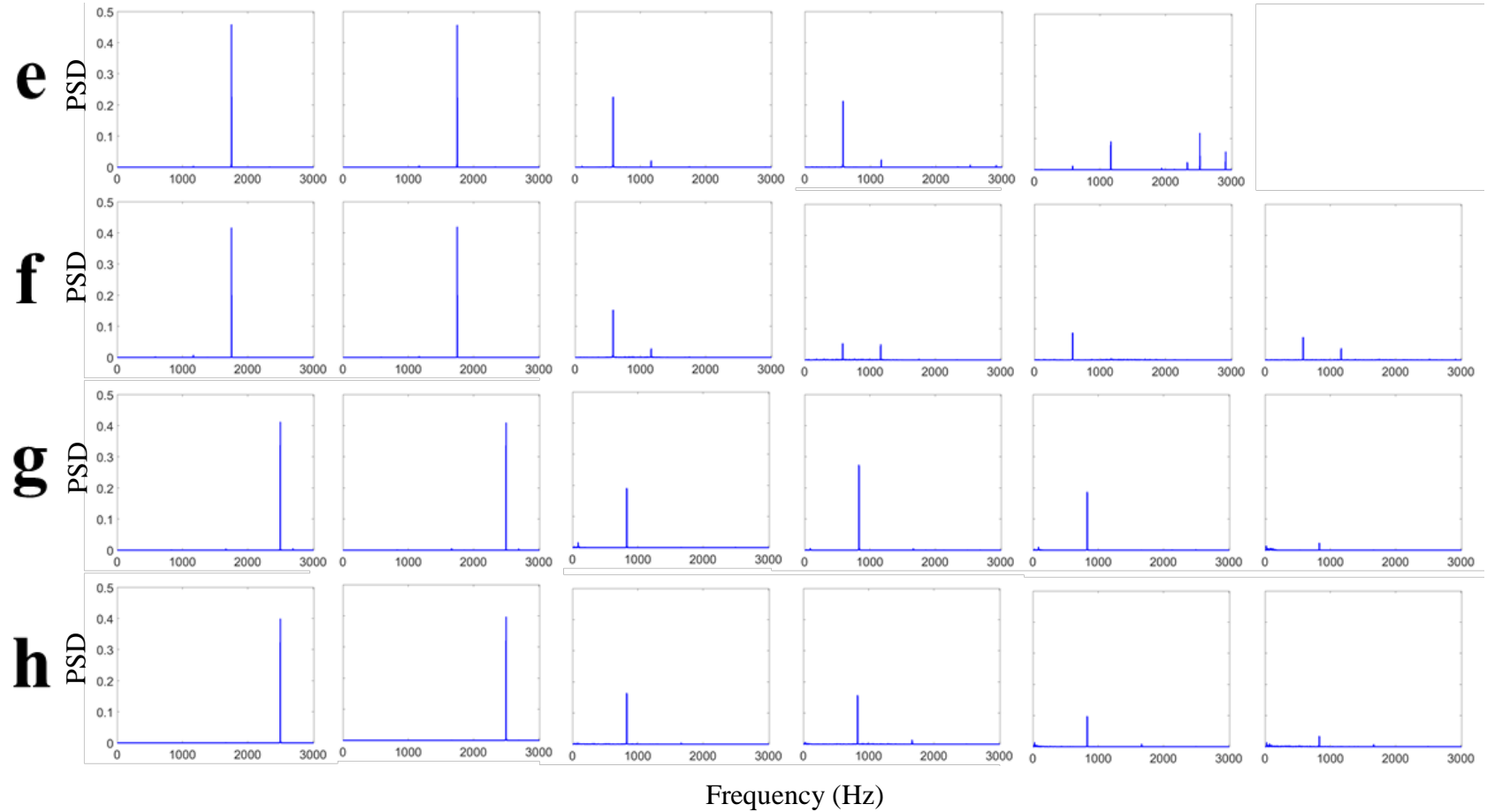
Figure 3.9. Damaged bell power spectral density plots of the constants data of relevant damaged bell modes in the (a) Background, (b) 20kRPM without flow, (c) 20kRPM-250CCM, (d) 20kRPM-750CCM, (e) 35kRPM-250CCM, (f) 35kRPM-750CCM, (g) 50kRPM-250CCM, and (h) 50kRPM-750CCM cases.
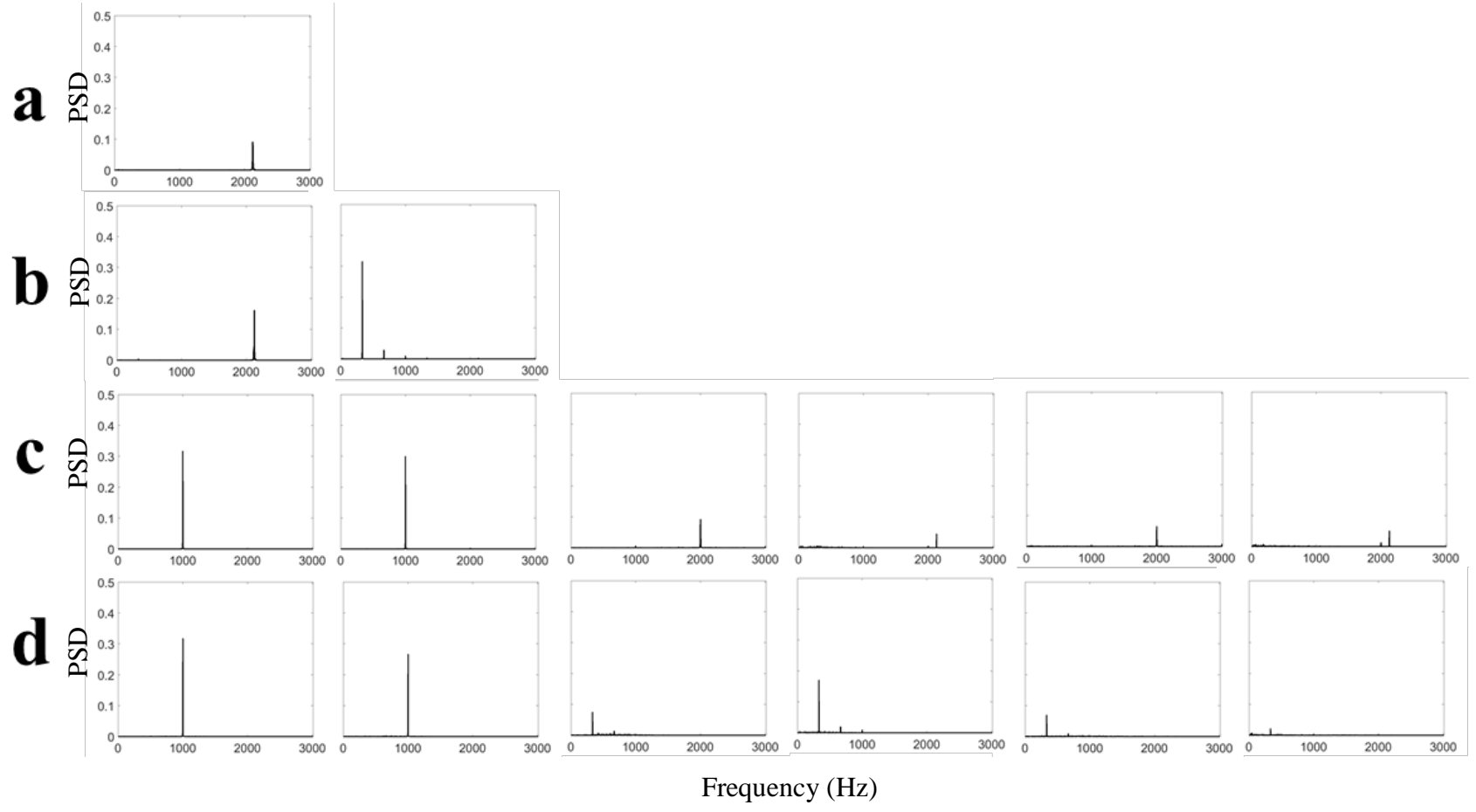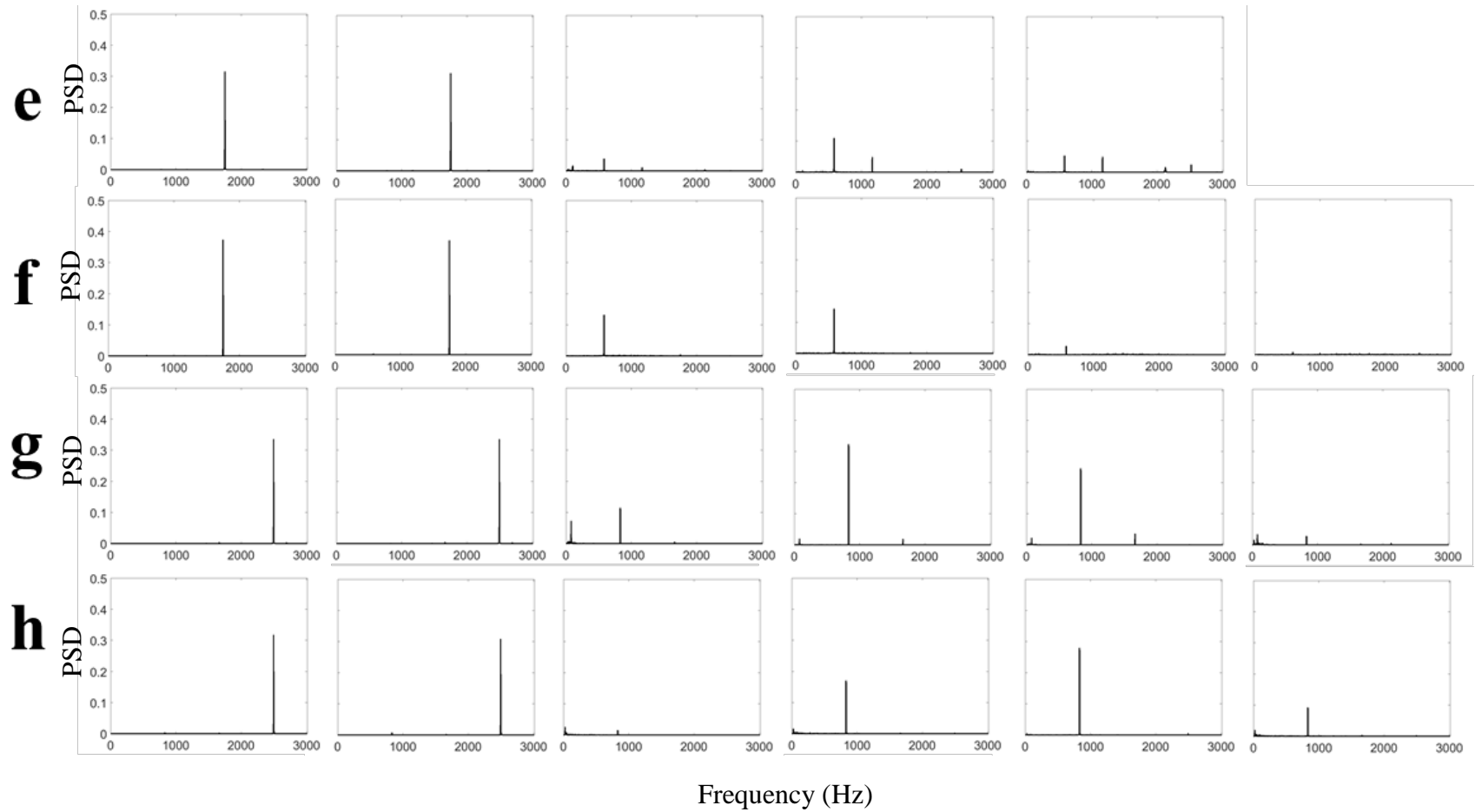
Figure 3.10. Undamaged bell power spectral density plots of the constants data of relevant undamaged bell modes in the (a) Background, (b) 20kRPM without flow, (c) 20kRPM-250CCM, (d) 20kRPM-750CCM, (e) 35kRPM-250CCM, (f) 35kRPM-750CCM, (g) 50kRPM-250CCM, and (h) 50kRPM-750CCM cases.

the x-axis values are the frequencies (in Hz) and that all plots should be comparable

because they are normalized by the same parameters. There are a few observations that

can be made from this data.

First, in the background data (Fig. 3.9a and Fig. 3.10a) a background frequency does

show up around 2.2kHz. This frequency was found to not be consistent across different

framerates and is therefore unlikely to be attributable to the background illumination and

could be an artifact of the electronics of the camera. However, since it does not make a

noticeable appearance in the other relevant modes, it can be ignored. Next, an overall

trend of more frequencies being present in the spectral data for the damaged modes

appears. The frequencies that show up appear to be harmonics as well, since they are

multiples of other frequencies in the spectra. This trend is especially noticeable in the

20kRPM no flow case (Fig. 3.9b), meaning that it can be attributed to the vibration of the

cup. Since the damaged cup is displaying these harmonic frequencies more often, this

could serve as a good parameter for judging whether or not a cup is damaged. If it is,

more harmonics should appear in the vibrational mode data near the cup and to

accentuate this fact during testing, perhaps no flow should be run through the system.

However, it should be noted that just because a cup has been damaged, and that damage

can be detected, that does not mean that it has sufficient impact on the droplets to be a

problem. Another observation is that for the first two modes of the cases with flow (Fig.

3.9c-h and Fig. 3.10c-h), the dominant frequency increases at a regular interval.

Upon further investigation of this fact, the frequency scales with every 1/3 cup

rotation. For the 20kRPM cases it is 1000 Hz, for the 35kRPM cases it is 1750 Hz (see

Fig. 3.4), and for the 50kRPM cases it is 2500 Hz. Therefore, this dominant frequency is

scaling with rotational rate, though it curiously is scaling with every third rotation. This might be attributable to the cup damage, if it weren't for the fact that both data sets display this frequency. The cup geometry was examined for any possible mechanisms that would cause this and the probable answer was found. The rotary bells send out the fluid over the inside of the bell through three channels as it rotates. An image of a bell with the center cap removed is shown in Fig. 3.11 to illustrate this finding through the glue residue left behind from the cap removal.

Figure 3.11. Rotary bell with center cap removed to display fluid outlets (indicated by arrows) to the interior of the bell, through the glue residue of the cap.

The constant data of the modes in their own image data does give some insight into changes between the two bells. However, comparing the modes to the other opposite

image data set would give even greater comparison data. With this in mind, the damaged bell modes were compared against the undamaged bell image data for constants of that data set in Fig. 3.12. In a manufacturing setting, this would serve as finding the modes for a bell of concern (damaged bell), and comparing it against an established healthy data set (undamaged bell). If certain modes show vastly different frequency content, then that difference could point to potential damage in the cup. The PSD results of the damaged bell modes substituted into the undamaged data set are displayed in Fig. 3.12. For direct comparison to what the PSD data should look similar to, see Fig. 3.10 for the undamaged bell against its own data set. If the damaged bell was identical to the undamaged bell, the frequency spectra should be nearly identical. While it is very similar, some higher order frequencies, associated with the third harmonic of bell rotational speed, appear for the substitution data. When compared to its old data set, where the constants were found for the damaged bell data set from the damaged bell modes, another interesting trend appears. Much of the excess harmonic activity from in the frequency data disappears. This is most evident in the comparison of the 20kRPM no flow cases (Fig. 3.9b and Fig. 3.12b). Such a trend indicates that while the vibrational modes of the damaged bell do exist in the undamaged bell data set, they do not appear with the same frequencies.

Frequency (Hz)
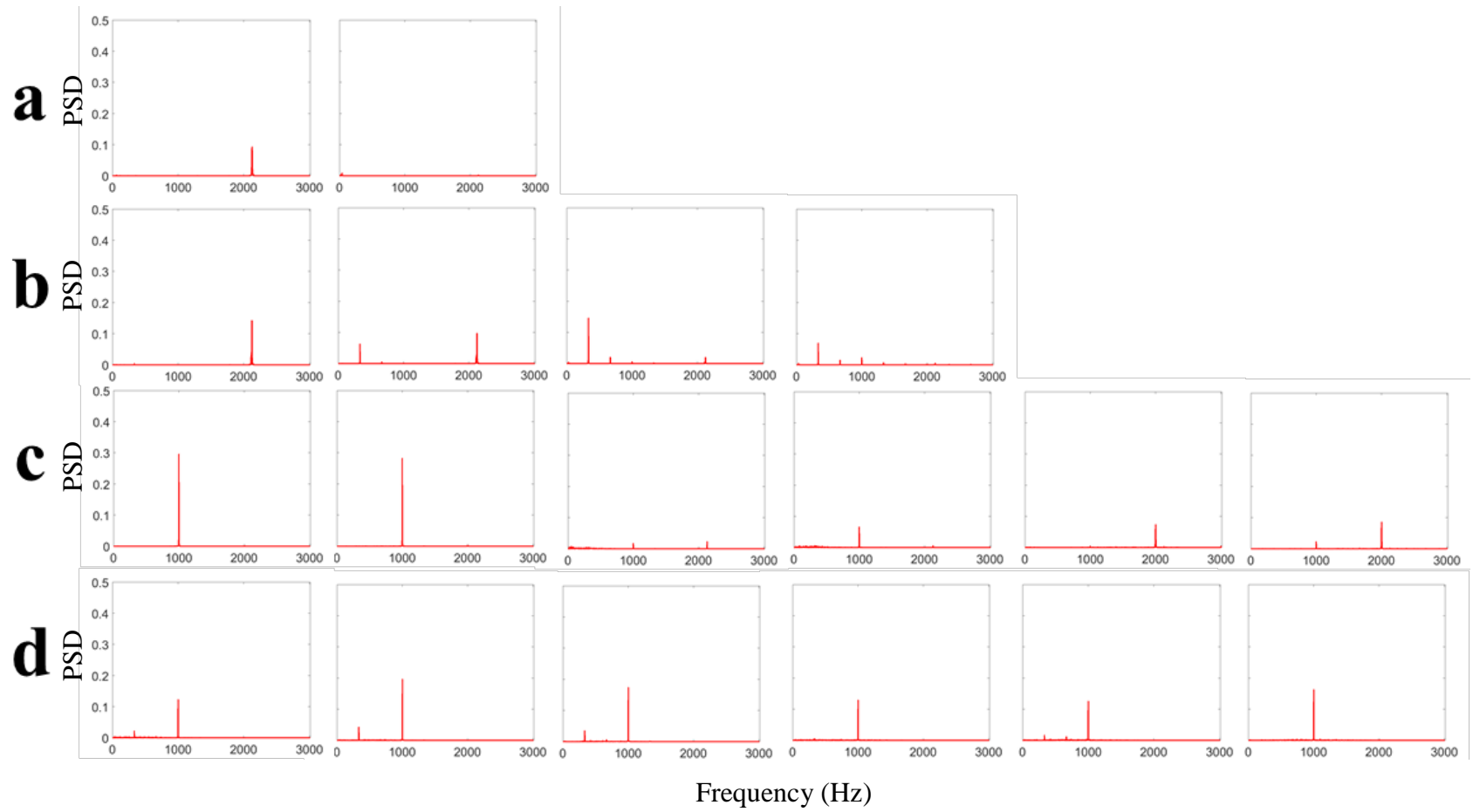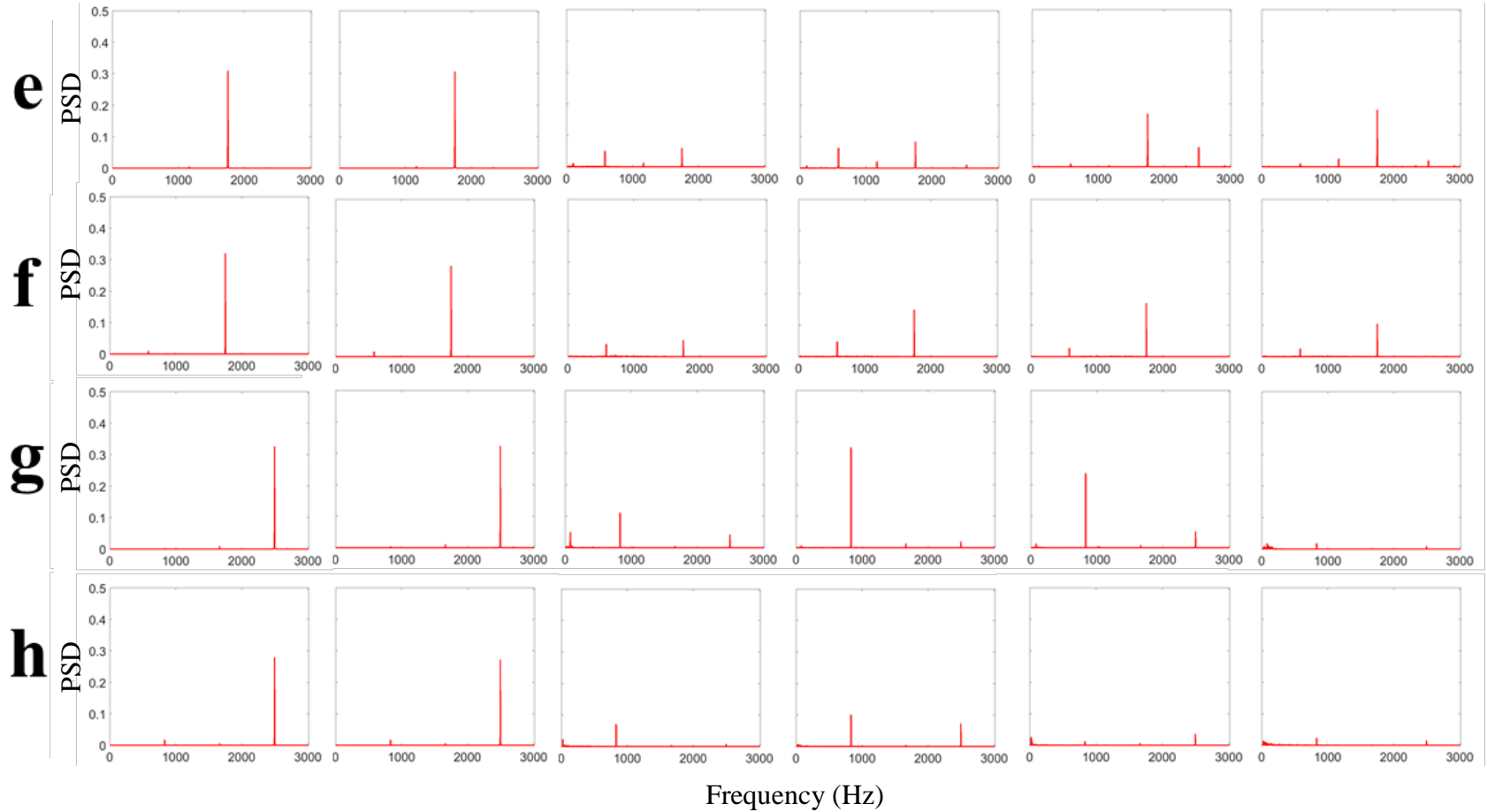
Figure 3.12. Damaged bell power spectral density plots of the constants data of relevant undamaged bell modes in the (a) Background, (b) 20kRPM without flow, (c) 20kRPM-250CCM, (d) 20kRPM-750CCM, (e) 35kRPM-250CCM, (f) 35kRPM-750CCM, (g) 50kRPM-250CCM, and (h) 50kRPM-750CCM cases.

3.4 Conclusion

POD can be a useful tool in identifying cyclical structures in a variety of flows. In this study, it was applied to a rotary bell atomizer at various operational parameters to see if differences in the flow could be identified between a damaged and undamaged bell. The goal of such an investigation would be to use POD in a paint booth setting as a tool for identifying if equipment has become faulty with a quick, simple test on typical image data. A high-speed camera was used to capture the image data of the cup during operation and some of the downstream flowfield. After examination of the flowfield yielded complicated results, further examination of the area near the cup was done since the vibrational modes present in that region yielded clearer frequency data.

Once the modes were output for both bells across a variety of conditions, the modal shapes and constants data were compared. The modal shapes showed that the damaged bell yielded sharper translational motion lines and had more vibrational mode data pervading through all of its cases. The mode constants data was converted into a normalized power density spectrum so that fair comparison across cases could be made. The PSD data revealed that the damaged bell modes contained more harmonic frequencies in their frequency content than the undamaged bell modes. Additionally, it was discovered that a third harmonic of the rotational rate of the bell consistently dominated many of the modes and this led to the discovery of a related aspect of the cup geometry. The damaged bell modes were then substituted into the undamaged bell data set for constants data that could reveal more about the damaged bell. What was found from this substitution was that the increase in harmonics that the damaged bell modes showed in their own data set disappeared and that some higher frequency content not

present from the undamaged bell modes appeared in the new PSD data. This led to the

conclusion that the PSD data could be used to show if a bell has become damaged, as it

should exhibit harmonics. If those harmonics disappear when compared to a healthy data

set, then it is likely to be damaged

Overall, POD was a useful tool in gathering information about the innate frequencies

of rotary bell atomization, but only when pointed at the most dominant cyclical feature of

cup vibration. It was able to find distinct differentiations between the damaged and

undamaged bells that could provide an easy diagnostic tool for equipment malfunction

inspections after more research is done. Further investigation is needed to quantify how

much impact this specific damage did to the effectiveness of the bell, as well as if POD

can be used as a tool to differentiate between different types of damage or damage

severity.

CHAPTER FOUR: SUMMARY AND FUTURE WORK

4.1 Detailed Summary

The overall theme of the work covered in this thesis is using various optical diagnostic tools and techniques, in conjunction with computational image processing, to characterize aspects of rotary bell paint atomizers. This work was mainly in the near-field region, where primary atomization occurs, as that was the region of interest. Study of the near field was lacking in contemporary literature in terms of investigation beyond taking still image data that some statistics were manually, and in terms of investigation with optical diagnostic methods common to other similar dynamic processes.

A method of investigating rotary bell atomization in the near field using a high-speed camera was developed in combination with an image processing algorithm. The high-speed capability allowed for a preliminary study of ligament and droplet breakup near the cup and the effect that increasing the primary operational parameter, rotational speed, had on those processes. The image processing algorithm was able to capture relevant size statistics for fluids in the original high-speed images, and was able to separate ligament and droplet statistics so that their independent changes with rotational speed could be captured. Using a PIV system, in combination with the image processing algorithm and consecutive high-speed image data that was correlated in time, velocity statistics were also able to be captured for these processes. These velocity vectors were also separable for the ligaments and droplets.

The qualitative findings from the investigation of the high-speed image data was that there were essentially three regimes of ligament breakup. These regimes were found to vary in probability of appearance as rotational speed was increased, and most certainly

affect the type of primary atomization that is occurring in the near field. More investigation is needed to gather quantitative data for comparison from this data. The statistical findings of the above method were in agreement with scientific literature and the trends were mostly expected. However, the primary notable finding from the use of this method was that the ligament size distributions were bimodal for a serrated bell-cup, which aids the claims of other research that has concluded a similar claim for the effect of serrations on fluid leaving the cup. A notable limitation of this method was pixel resolution, due to the frame size having to be attain the high acquisition rates necessary for the operational speeds examined.

Due to the limitations of the pixel resolution as frame rate was increased for the high-speed camera, a different setup was adopted to capture the ligament and droplet statistical changes at higher rotational speeds. Also tested with this setup was the difference between identical bells that only differed in that one bell was serrated, and the other unserrated. An Nd:YAG laser, in combination with an optical filter composed of Rhodamine 6G and ethanol to reduce background signal noise, was used to illuminate a new experimental setup. The camera of this still-image capturing setup had a much higher pixel resolution and, using the same image processing method as was used on the high-speed data with some slight alterations, much smaller fluid sizes were able to be captured for the near field region. Similar types of statistics were able to be captured regarding ligament and droplet sizes. Velocity vectors were unable to be obtained from this method due to the firing rate of the laser not being fast enough to allow light for two images that could be correlated in time. A second laser is suggested for future work to obtain this information.

86

The primary findings of the still-image method were that hydraulic diameters for both the serrated and unserrated bells increased with increasing flowrate and decreasing rotational speed. However, though the trend directions were similar for both bells, the rate of change comparisons of these trends showed that the effect of rotational speed is more impactful on the serrated bell cases. Additionally, ligament sizes were much more dependent on flowrate than droplets. Ligament lengths and widths also showed that the serrations of a bell limit the effect that flowrate has on ligament size.

Finally, a statistical method used to study cyclical, turbulent processes, known as proper orthogonal decomposition, was utilized in an attempt to identify damage on a rotary bell-cup. The goal was to ascertain differences in the POD findings from the damaged cup data and undamaged cup data via the image data captured from a side-profile view of the cup and flowfield during operation. This data was captured using a high-speed camera, and ultimately the full-frame data had to be cut to more clearly identify processes in the data sets.

The findings from the use of POD were that the damaged cup produced slightly different modal images and frequency content from the undamaged bell. The damaged modal images displayed sharper translational motion indications than the slightly curved translational motion indications in the undamaged data. Cup vibration also pervaded through most, if not all, of the damaged cup modes. The undamaged cup modes did not consistently display the cup vibrational modes. Additionally, the frequency content of the modes, through power spectral density plots, displayed the fact that the vibrational modes scaled with a third harmonic of the bell rotational speed. This finding was attributed to the effect of the bell having three outlets for the liquid during the filming of the cup

during operation. The frequency content also showed that the damaged bell displayed more harmonic frequencies, in general, than the undamaged bell for vibrational motion. After substituting the damaged modes into the undamaged image data to find how the constants in the new data set might differ, it was found that the damaged modes lost the harmonics in the frequency content. Therefore, a way to take a known undamaged data set, and substitute an unknown condition data set into it to determine its possible condition was found. Further research needs to be done to more fully understand the effects of different types of damage and different levels of severity of damage and their effect on this frequency content. The downstream effects of the damage are also unknown at this point and need to be studied.

4.2 Recommendations of Future Work

As with any scientific inquiry, there remain many unanswered questions or avenues related to this work that could be investigated further, or were not investigated at all. One such avenue was a more specific, in-depth analysis of the ligament breakup mechanisms involved in rotary bell atomization. What was done in this work was to investigate what was happening at speeds up to 12kRPM with a high-speed camera. At the frame size that was utilized, this was the approximate limit at which high-speed imaging would be able to capture discernable image data before blurring would interrupt the ability to make accurate observations of ligament breakup. Therefore, for much higher rotational speeds, like 50kRPM, the following recommendations should allow for the ability to capture the ligament breakups. First, the optics of the setup would need to be altered slightly. A different lens would need to be used that could zoom in further on the cup edge. This

would allow for a larger image of ligament breakup to be captured, since the camera was previously as close as it could be without interfering with the shaping air of the bell. Making the ligament breakup larger in the frame would also allow for less optical resolution, meaning that the frame could be cut even further, and faster acquisition rates could be reached. This would make it possible to capture the ligament breakups at much higher rotational speeds.

Additionally, in regards to ligament breakup, investigation into the effect of viscosity should be done. Adding glycerol or some other thickening agent to the water to increase the viscosity of the fluid going through the bell would be ideal to test what effects that viscosity and surface tension have on the breakup shape/method and breakup time. Using paint, ideally close to that used in actual paint booths, would also be particularly useful in gaining directly useable information for industrial application.

Filming the ligament formation, as well as the film formation inside of the bell, during the process in front of the bell would be another area to explore further. Many studies have looked at this area, but without the shaping air running, and usually at lower rotational speeds than are applicable to industry. Finding a way to film this region with the inclusion of shaping air, at higher rotational speeds, and without interrupting the flow with the optical setup or damaging the optical equipment, should provide useful information about the fluid dynamics for this process.

Finally, for ligament-related investigation suggestions, improving the ligament capturing method in the image-processing algorithm would prove very useful. One specific recommendation for this would be to improve the aspect of the algorithm that distinguishes between what is a ligament, and what is not, since the current method is

fairly rudimentary. Another specific recommendation would be to devise a way to single out a ligament, follow it through the breakup process, and classify that breakup, all automatically. Doing so would be not only useful in that it could be applied to large experimental data sets to see what and when specific breakup mechanisms occur, but it could potentially be adopted by other industries as well.

In relation to the droplet distribution data, there are a few recommendations that extend from the work done here as well. First, different liquids, with varying viscosities, should be tested to again examine the effect of material properties on the near-field droplet sizes during primary atomization. Previous works, as discussed, focus on these distributions further downstream, during and after secondary atomization. Investigation of these parameters in the near field is necessary to fully understand their influence in this region. Additionally, varying the shaping air during the conditions already tested, as well as with the addition of newly introduced parameters like viscosity, and see its influence on primary atomization would be an interesting avenue to explore. Presumably, changing the shaping air would not affect the primary atomization by directly contacting the flow in this region. However, it is conceivable that it could have an effect on the flow through changing the inherent vibrational modes of the system, changing the instabilities present and thus the ligament breakups and droplet formations. It could also influence the primary atomization through the well-documented flow recirculation through recirculating fluid contact or some other means. There does not currently appear to be a lot of literature on that specific aspect of the recirculation zone for this process.

Another improvement to the capturing of near-field droplet distribution data, would be the addition of another laser to the optical setup. Having two lasers, offset slightly in

90

time, involved in the optical setup described in part two of this thesis would allow for velocity measurements at the higher rotational speeds. This could be done using the same PIV technique described in part one of this thesis, where the binarized image is imposed on the original, and similar velocity statistics could be obtained.

Expanding upon the POD work done, further investigation could be done into how different forms of damage effect the POD data, and how those changes are reflected in the ligament/droplet distribution data in both the near field and in the spray plume. Isolating the changes that specific damages make would not only improve the understanding of the fluid formations in this area, but would provide meaningful industrial data that would further justify the use of POD for equipment checks in automotive painting booths.

Finally, there is much work that needs to be done looking at the effect of serrations on rotary bell atomization as a whole. One specific course of action that is recommended is to investigate the differences between a serrated and unserrated bell with POD analysis. Work not presented here was done in regards to this, but the preliminary results obtained showed minute differences that could not be explained in a satisfactory way. However, it is possible, that with a more in-depth analysis of different modes that appear in the flow or by examining different regions of areas not fully explored like the spray plume, quantifiable differences could be obtained.

There likely exist more areas of possible future research related to the work conducted towards this thesis. The suggestions presented here merely represent those that had been explicitly discussed or some plans had been made for. Hopefully, individuals reading this work gain some ideas concerning different, undiscussed experimental

methods or areas of investigation that would ultimately benefit the greater scientific

community.

APPENDIX

A.1 CHAPTER ONE RELEVANT MATLAB SCRIPTS

<u>HS_Img_Processing.mat</u>

```
% This script cycles through the video image files and conducts the image
% processing necessary to effectively binarize the images and to seperate
% the ligaments from the droplet. It also includes outputs for the .bmp
% files necessary to be utilized later by the Davis Lavision PIV software.
%clear workspace
clc;
close all;
clear variables;
addpath('H:\Transferred Files\Water\Water_3-24-16\4-14-16_3\')
%For cylcing of code through different rotational rates based on naming
%scheme
Case = 5:12;
for g = 1:length(Case)
    %Import video file and read image data
    imgfolder = strcat('C:\Users\jewi233\Google Drive\FordProject\HS Consecutive Ligament
Images\',num2str(Case(g)),'kRPM\');
    d=strcat(num2str(Case(g)),'0RPM_340k_L2.avi');
    case_v = strcat(num2str(Case(g)),'k');
    tic
    vidObj = VideoReader(d);
    numf = vidObj.NumberOfFrames;
    %Preallocating blank cells for later
        LL = {};
        WW = {};
        PL = {};
        AL = {};
        PD = {};
        AD = {};
        PB = {};
        AB = {};
    %Build sequential images for velocity statistics
%       rr = 1:100:152000;
%       ss = 2:100:152000;
%       q = sort(horzcat(rr,ss));
    %This is for size statistics
    q=1:100:100000;
    for pp=1:length(q)
        I = read(vidObj,[q(pp) q(pp)]);
        %Defining image
        original_img = I;
        [h,w]=size(I);
        %Setting very low intensity to zero
```

```matlab
aa = find(I>3);
adjusted_img = zeros(h,w);
adjusted_img(aa) = I(aa);
pixpmm=25.9; %defining from calibration (pixels per mm)
mm=3; %mm from cup
%% Avg Filter
ones_mat = ones(5,5)/25;
avg_filt_img = imfilter(adjusted_img,ones_mat);
%% Dilation
structuring_elem = strel('line',10,90);
Dilated_img = imdilate(avg_filt_img,structuring_elem);
%% Inversion/Back Subtraction
img_compliment_1 = imcomplement(adjusted_img);
img_compliment_2 = imcomplement(Dilated_img);
Inverted_img = img_compliment_1-img_compliment_2;
for i = 1:h
    for j = 1:w
        if Inverted_img(i,j)<0
            Inverted_img(i,j) = 0;
        else
        end
    end
end
%% Binarize and Thresholding
%Secondary filtering, if necessary
Second_filt_img=medfilt2(Inverted_img);
%Set threshold
thresh=12;
BW_img = Inverted_img>thresh;
%Filling in gaps in image
bridged_BW_img = bwmorph(BW_img,'bridge');
BW_no_cup_img=BW_img;
[h,~]=size(adjusted_img);
for i=1:h
    u(i)=find(adjusted_img(i,:)>0,1,'first');
    p(i)=u(i)+1;
    BW_no_cup_img(i,1:p(i))=0;
end
%Optional writing raw image to file
% imwrite(I(:,:,1,1),strcat(imgfolder,'Raw Images\img_',num2str(pp),'.jpg'));
%% Identify Connected Components by Attachment to Cup
CC = bwconncomp(bridged_BW_img);
numPixels = cellfun(@numel,CC.PixelIdxList);
[biggest,idx] = max(numPixels);
lig_and_cup_img = false(size(bridged_BW_img));
lig_and_cup_img(CC.PixelIdxList{idx}) = true;
%Eliminating cup from image
lig_no_cup_img = lig_and_cup_img;
[h,~]=size(adjusted_img);
for i=1:h
```

```matlab
        u(i)=find(adjusted_img(i,:)>0,1,'first');
        p(i)=u(i)+1;
        lig_no_cup_img(i,1:p(i))=0;
end
%% Counting Ligaments
%Combine close objects to get true ligament number.
lig_area_img = bwmorph(lig_no_cup_img,'bridge');
[h,w]=size(original_img);
for i=1:h
    for j=1:w
        E(i)=find(original_img(i,:)>7,1,'first');
        F(i)=E(i)+1;
        lig_area_img(i,1:F(i))=0;
    end
end
%Ligament Counts
CC2 = bwconncomp(lig_area_img);
Ligaments = CC2.NumObjects;
%% Impose Image Onto Original
%use this to check how well the process is working (with images)
BWM = bwmorph(BW_no_cup_img,'remove');
IC = imcomplement(original_img);
BWC = imcomplement(BWM);
BWC2 = imcomplement(BW_no_cup_img);
IEG = immultiply(IC,BWC);
IEG2 = immultiply(IC,BWC2);
EG = imcomplement(IEG);      %This is the image that you check
EG2 = imcomplement(IEG2);
%% Determining and Displaying Ligament Properties
if Ligaments == 0
elseif Ligaments > 0
    %Construct a struct to put data in, optional matrix data
    %           L = ligLengths(lig_area_img);
    %           LL(end+1:end+length(L))=L;
    stats(pp).LL = ligLengths(lig_area_img);
    %           W = ligWidths(lig_area_img,F);
    %           WW(end+1:end+length(W))=W;
    stats(pp).WW = ligWidths(lig_area_img,F);
    %Define Droplet Only Image
    BW_drop_only=BW_no_cup_img-lig_no_cup_img;
    BW_drop_only=im2bw(BW_drop_only,0.0039);
    %Both
    BW_both = logical(BW_drop_only + lig_no_cup_img);
    %Obtain the pixel location data of the binarized fluid in all
    %of the images.
    sL = regionprops('table',lig_no_cup_img,'Area','PixelIdxList');
    sD = regionprops('table',BW_drop_only,'Area','PixelIdxList');
    CC3 = bwconncomp(BW_both);
    sB = regionprops('table',CC3,'Area','PixelIdxList');
    %% Velocity
```

```matlab
                %Convert images to grayscale for velocity statistics
%                lig_vel_img = immultiply(lig_no_cup_img,I);
%                drop_vel_img = immultiply(BW_drop_only,I);
%                both_vel_img = immultiply(BW_both,I);
%                Output BMP images for later velocity statistics
%                bmpfile = strcat('H:\HS_Data_5-19-20\8-16-
17\BMPs\',num2str(Case(g)),'k');
%                if mod(pp,2) == 0
%                bmp =
HS_bmpout(bmpfile,pp,lig_vel_img,drop_vel_img,both_vel_img,prev_lig_img,prev_drop_img,p
rev_both_img,Case);
%                else
%                end
%
%                prev_lig_img = lig_vel_img;
%                prev_drop_img = drop_vel_img;
%                prev_both_img = both_vel_img;
            for z=1:height(sL)              %Finding Ligament Areas/Perimeters
                IZ = zeros(h,w);
                [AZ]=sL.PixelIdxList{z};
                IZ(AZ)=1;
                IZZ = cat(2, zeros(h,1), IZ, zeros(h,1));
                IZZ = cat(1, zeros(1,w+2), IZZ, zeros(1,w+2));
                stats(pp).PL(z)= Perim(IZZ);
%                PL(end+1:end+length(Perim(IZZ))) = Perim(IZZ);
                stats(pp).AL(z) = sL.Area(z,1);
%                AL(end+1:end+length(Area)) = sL.Area(z,1);
            end
            clearvars SL AZ IZ IZZ
            for z=1:height(sD)   %Finding Droplet Areas/Perimeters
                IZ = zeros(h,w);
                [AZ]=sD.PixelIdxList{z};
                IZ(AZ)=1;
                IZZ = cat(2, zeros(h,1), IZ, zeros(h,1));
                IZZ = cat(1, zeros(1,w+2), IZZ, zeros(1,w+2));
                stats(pp).PD(z)= Perim(IZZ);
%                PD(end+1:end+length(Perim(IZZ))) = Perim(IZZ);
                stats(pp).AD(z) = sD.Area(z,1);
%                AD(end+1:end+length(Area)) = sD.Area(z,1);
            end
            clearvars SD AZ IZ IZZ
            for z=1:height(sB) %Finding  ligament and droplet combined Areas/Perimeters
                IZ = zeros(h,w);
                [AZ]=sB.PixelIdxList{z};
                IZ(AZ)=1;
                IZZ = cat(2, zeros(h,1), IZ, zeros(h,1));
                IZZ = cat(1, zeros(1,w+2), IZZ, zeros(1,w+2));
                stats(pp).PB(z)= Perim(IZZ);
%                PB(end+1:end+length(Perim(IZZ))) = Perim(IZZ);
                stats(pp).AB(z) = sB.Area(z,1);
```

```matlab
%                  AB(end+1:end+length(Area)) = sB.Area(z,1);
            end
            clearvars SB AZ IZ IZZ
    end
    if mod(pp,10)==0
        pp
        toc
        tic
    else
    end
end
%Output workspace data to a file:
% outd = 'H:\HS_Data_5-19-20\8-16-17\';
% out_filename = strcat(outd,case_v,'_workspace.mat');
% save(out_filename);
clearvars -except Case
addpath('H:\Transferred Files\Water\Water_3-24-16\4-14-16_3\')
end
```

HS_bmpout.mat

```
function bmp = HS_bmpout(bmpfile,pp,lig_img,drop_img,both_img,pl,pd,pb,C)
%
%This function is designed to output the binarized ligament, droplet, and
%combined images to a specified file so that they can be imported by the Lavision
% Davis software in the correct order and in the correct orientation since Davis requires
% that you have two consecutive images stacked vertically on top of one another during the
% import process.  The function requires the following inputs:
%   bmpfile  - an output file to send the images to
%   pp       - even number frame of video
%   lig_img  - binarized ligament image
%   drop_img - binarized droplet image
%   both_img - binarized combined image
%   pl       - previous ligament image
%   pd       - previous droplet image
%   pb       - previous combined image
pp = pp/2;
LL = vertcat(pl,lig_img);   %Stacking the corresponding images vertically
DD = vertcat(pd,drop_img);
BB = vertcat(pb,both_img);
%conditionally naming and outputting the images so that they are ordered
%correctly in the file:
if pp > 0 && pp < 10
    imwrite(LL, strcat(bmpfile,'\',num2str(C),'k_All_Lig\image000',num2str(pp),'.bmp'));
    imwrite(DD, strcat(bmpfile,'\',num2str(C),'k_All_Drop\image000',num2str(pp),'.bmp'));
    imwrite(BB, strcat(bmpfile,'\',num2str(C),'k_All_Both\image000',num2str(pp),'.bmp'));
elseif pp > 9 && pp < 100
    imwrite(LL, strcat(bmpfile,'\',num2str(C),'k_All_Lig\image00',num2str(pp),'.bmp'));
    imwrite(DD, strcat(bmpfile,'\',num2str(C),'k_All_Drop\image00',num2str(pp),'.bmp'));
    imwrite(BB, strcat(bmpfile,'\',num2str(C),'k_All_Both\image00',num2str(pp),'.bmp'));
elseif pp > 99 && pp < 1000
    imwrite(LL, strcat(bmpfile,'\',num2str(C),'k_All_Lig\image0',num2str(pp),'.bmp'));
    imwrite(DD, strcat(bmpfile,'\',num2str(C),'k_All_Drop\image0',num2str(pp),'.bmp'));
    imwrite(BB, strcat(bmpfile,'\',num2str(C),'k_All_Both\image0',num2str(pp),'.bmp'));
elseif pp > 999
    imwrite(LL, strcat(bmpfile,'\',num2str(C),'k_All_Lig\image',num2str(pp),'.bmp'));
    imwrite(DD, strcat(bmpfile,'\',num2str(C),'k_All_Drop\image',num2str(pp),'.bmp'));
    imwrite(BB, strcat(bmpfile,'\',num2str(C),'k_All_Both\image',num2str(pp),'.bmp'));
end
bmp = 1; %arbitrary output
end
```

ligLengths2.mat

```matlab
function [ liglengths ] = ligLengths2( img )
%This function finds the length of ligaments given a binarized image (img)
comp=bwconncomp(img);
numcomp=comp.NumObjects;
h=comp.ImageSize;
for q=1:numcomp
   t=comp.PixelIdxList{q};
   lig=zeros(h(1),h(2));
   for p=1:length(t)
     lig(t(p))=1;
   end
   sk=bwmorph(lig,'skel',Inf);
[ligsh,ligsw]=find(sk>0);
liglengths(q)=length(ligsh);
ligss=zeros(h(1),h(2));

for i=1:length(ligsh)
   ligss(ligsh(i),ligsw(i))=1;
end
L=bwlabel(ligss,4);
LL=max(L(:));
         liglengths(q)=liglengths(q)+LL*(sqrt(2)-1);
 end
end
```

<u>ligWidths.mat</u>

```matlab
function [ ligwidth ] = ligWidths(img,u)
%This function finds the ligament width given the image (img) and pixel
%locations of the cup edge (u)
comp=bwconncomp(img);
numcomp=comp.NumObjects;
h=comp.ImageSize;
for q=1:numcomp
    t=comp.PixelIdxList{q};
    lig=zeros(h(1),h(2));
    for p=1:length(t)
        lig(t(p))=1;
    end
% sk=bwmorph(lig,'skel',Inf);
% ligs=find(sk>0);
% liglengths(q)=length(ligs);
l=zeros(length(h(1)));
for i=1:h
    if lig(i,u(i))>0 ||lig(i,u(i)+1)>0
        l(i)=1;
    end
end
ligwidth(q)=sum(l);
% comp2=bwconncomp(l);
% numcomp2=comp2.NumObjects;
% for i=1:numcomp2
%    tt=comp.PixelIdxList{i};
%    ligwidth(q)=length(tt);
% end
% end
% [h,~]=size(img);
% l=zeros(length(h));
% for i=1:h
%    if img(i,u(i))>0 ||img(i,u(i)+1)>0
%        l(i)=1;
%    end
% end
% comp=bwconncomp(l);
% numcomp=comp.NumObjects;
% for i=1:numcomp
%    t=comp.PixelIdxList{i};
%    ligwidth(i)=length(t);
% end
end
```

Perim.mat

```
function [ perimeter ] = Perim( img )
%Perim will output the perimeter of each object
%img needs to be padded with zeros on outside so boundary effects are not
%counted
[h,w]=size(img);
b=ones(3,3);
img22=imdilate(img,b);
img2=zeros(h+2,w+2);
img2(2:end-1,2:end-1)=img22;
img3=zeros(h+2,w+2);
    [i,j]=find(img2==1);
    for ii=1:length(i)
       clear pt
       pt(1)=img2(i(ii)-1,j(ii));
          pt(2)=img2(i(ii)+1,j(ii));
       pt(3)=img2(i(ii),j(ii)+1);
       pt(4)=img2(i(ii),j(ii)-1);
       if sum(pt)==2
          if (pt(1) && (pt(3) | pt(4))==1 || pt(2) && (pt(3) | pt(4))==1)
             img3(i(ii),j(ii))=1;
          end
       end
    end
img4=img2-img3;
img5=bwmorph(img4,'remove');
ij=find(img5==1);
perimeter=length(ij);
for ii=1:length(i)
if (img5(i(ii)-1,j(ii)-1) && img5(i(ii)+1,j(ii)+1))==1 || (img5(i(ii)-1,j(ii)+1) && img5(i(ii)+1,j(ii)-
1))==1
perimeter=perimeter+(sqrt(2)-1);
end
end
end
```

<u>HS_Output_Size_Stats.mat</u>

```matlab
%This script loops through the output size data acquired from
%HS_Img_Processing.mat and converts it into more immediately accessible
%data

%Clear Workspace
clear all; close all; clc;
%% SIZE STATISTICS
%Set Directory and Import Data
d ='H:\HS_Data_5-19-17\8-16-17\Size\Size Statistics\';
addpath('C:\Users\jewi233\Google Drive\FordProject\Scripts_Functions')
%Loop through all cases
for i = 5:12
    j=i-4;
    %Input Workspace
    wsfile = strcat(d,num2str(i),'k_workspace.mat');
    %Load Variables
    load(wsfile);
    %Specify Last Frame to Cycle Through
    fr = 1501;
    %Bins
    sizebins = 0:20:600;
    %Specify Normal Distributions
    ND_Dist_L{j} = Norm_Sum_histL2';
    ND_Dist_D{j} = Norm_Sum_histD2';
    ND_Dist_B{j} = Norm_Sum_histB{fr}';
    %Specify Volume Distributions
    VD_Dist_L{j} = Norm_Sum_VDL_hist2';
    VD_Dist_D{j} = Norm_Sum_VDD_hist2';
    VD_Dist_B{j} = Norm_Sum_VDB_hist{fr}';
    %Collect D32
    if i == 7
    D_32(1,j) = nanmean(cell2mat(Lig_D32));
    D_32(2,j) = nanmean(cell2mat(Drop_D32));
    D_32(3,j) = nanmean(cell2mat(Both_D32));
    else
    D_32(1,j) = Avg_L_D32{fr};
    D_32(2,j) = Avg_D_D32{fr};
    D_32(3,j) = Avg_B_D32{fr};
    end
    %Collect Spans and Ligament Lengths/Widths
    L_Diams = [];
    D_Diams = [];
    B_Diams = [];
    L_lengths = [];
    L_widths = [];
    for k = 1:fr-1
        diamsL = cell2mat(diamL(k));
        diamsD = cell2mat(diamD(k));
```

```matlab
        diamsB = cell2mat(diamB(k));
        LL = Lig_L{k}/pixpmm;
        WW = Lig_W{k}/pixpmm;
        L_Diams(1,end+1:end+length(diamsL)) = diamsL';
        D_Diams(1,end+1:end+length(diamsD)) = diamsD';
        B_Diams(1,end+1:end+length(diamsB)) = diamsB';
        L_lengths(1,end+1:end+length(LL)) = LL';
        L_widths(1,end+1:end+length(WW)) = WW';
        clearvars diamsL diamsD diamsB
    end
    L_lengths(L_lengths==0) = [];
    L_widths(L_widths==0) = [];
    xLL=[0:.3:20];
    xWW=[0:.04:1 1:2];
    hist_xLL{j} = (hist(L_lengths,xLL)/sum(hist(L_lengths,xLL)))';
    hist_xWW{j} = (hist(L_widths,xWW)/sum(hist(L_widths,xWW)))';
    Lig_D{j} = L_Diams';
    Drop_D{j} = D_Diams';
    Both_D{j} = B_Diams';
    [L_Span{j},~,~,~,~,~,~] = droplet_vspan2(Lig_D{j});
    [D_Span{j},~,~,~,~,~,~] = droplet_vspan2(Drop_D{j});
    [B_Span{j},~,~,~,~,~,~] = droplet_vspan2(Both_D{j});
    clearvars diamsL diamsD diamsB L_Diams D_Diams B_Diams L_lengths L_widths
end
```

HS_Output_Vel_Stats.mat

```
%%This script imports te data from the Davis output files and converts the
%data into useable velocity vector data and the workspace with all of the
%outputs is saved.

%clear workspace
clear;
close all;
clc;
%files location
dir='H:\MyProjects\Velocity_Statistics_5_30_17\';
addpath('C:\Users\jewi233\Google Drive\FordProject\Scripts_Functions\')
addpath('C:\Users\jewi233\Documents\DaVis-MATLAB\')
RR = 5:12;
for k = RR
% vstats = struct([]);
dirDP = strcat(dir,num2str(k),'k_All_Drop\PTV\');
disp(strcat('calculating: ',num2str(k),'k',' Droplet Statistics'))
xc = -878.4455;
yc = -10.7115;
% MVD=[];
% Vel_D = [];
% Mass_D = [];
% Diam_D = [];
% U_magD = [];
% V_magD = [];
% N_magD = [];
% T_magD = [];
pixpmm = 26.22;
mm_pix = .0381395;
Density = .000001; %kg/mm^3
tic
for idx = 1:1500
vstats.Vel_D{idx} = [];
vstats.Diam_D{idx}= [];
vstats.U_magD{idx} = [];
vstats.V_magD{idx} = [];
vstats.N_magD{idx} = [];
vstats.T_magD{idx} = [];
    if idx < 10
        name='B0000';
    elseif idx>=10 && idx<100
        name = 'B000';
    elseif idx>=100 && idx<1000
        name = 'B00';
    elseif idx>=1000
        name = 'B0';
    end
    n = [name num2str(idx)];
```

```matlab
    file=strcat(dirDP,n,'.vc7');
    %import file structure
    inst1=readimx(file);
    %extract x,y,u,v
    [xx,yy,uinst,vinst]=showimx(inst1);
    %extract information about the map

       %find how many rows and columns there are
    [xxx,yyy]=size(xx); %xx will be columns, yy will be rows
    %find the spacing in mm in the x and y direction
    xx=xx(:,1);
    yy=yy(1,:);
    u=uinst';
    v=vinst';
    magn = sqrt(v.^2+u.^2);
    magn_loc = find(magn);
close all
[x,y]=meshgrid(xx,yy);
%%
dirD = strcat(dir,num2str(k),'k_All_Drop\');
    file=strcat(dirD,n,'.im7');
    %import file structure
    inst2=readimx(file);
    %extract x,y,u,v
    [xx,yy,uinst]=showimx(inst2);
    %extract information about the map
       %find how many rows and columns there are
    [xxx,yyy]=size(xx); %xx will be columns, yy will be rows

    Int_Map = mat2gray(255*mat2gray(uinst));
    BW = Int_Map>0;
    [h,w] = size(BW);
    CC = bwconncomp(BW);
    s = regionprops('table',BW,'Area','PixelIdxList');
    Objects = CC.NumObjects;
    for component = 1:Objects
        A = CC.PixelIdxList{1,component};
        B = magn_loc;
        C = intersect(A,B,'rows');
        num_vectors = length(C');
        if num_vectors == 0
            continue
        elseif num_vectors == 1
          %Finding N and T Components
          dx = x(C) - xc;
          dy = y(C) - yc;
          phi1 = atan(dy/dx);
          phi2 = atan(abs(u(C))/v(C));
          theta = phi1 + phi2;
```

```matlab
            %Grab velocity of component
            Velocity = magn(C);
            U_mag = abs(u(C));
            V_mag = abs(v(C));
            N_mag = abs(Velocity*cos(theta));
            T_mag = abs(Velocity*sin(theta));
            %Get Perimeter and Area to Obtain Volume
            IZ = zeros(h,w);
            IZ(A) = 1;
            Perimeter = Perim(IZ);
            Area = s.Area(component,1);
            %Calculate D_32
            Diam = 4*Area/Perimeter;
%               Volume = Diam^3;
%               mass = Volume*Density;
%               mv = mass*Velocity;
%               MVD(end+1:end+length(mv)) = mv;
%               Mass_D(end+1:end+length(mass)) = mass;
            vstats.Vel_D{idx}(end+1:end+length(Velocity)) = Velocity;
            vstats.U_magD{idx}(end+1:end+length(U_mag)) = U_mag;
            vstats.V_magD{idx}(end+1:end+length(V_mag)) = V_mag;
            vstats.N_magD{idx}(end+1:end+length(N_mag)) = N_mag;
            vstats.T_magD{idx}(end+1:end+length(T_mag)) = T_mag;
            vstats.Diam_D{idx}(end+1:end+length(Diam)) = Diam;
        elseif num_vectors > 1
            %Finding N and T Components
            dx = mean(x(C) - xc);
            dy = mean(y(C) - yc);
            phi1 = atan(dy/dx);
            phi2 = atan(mean(abs(u(C)))/mean(v(C)));
            theta = phi1 + phi2;
            %Grab average velocity of component
            V = magn(C);
            Velocity = mean(V);
            U_comp = abs(u(C));
            U_mag = mean(U_comp);
            V_comp = abs(v(C));
            V_mag = mean(V_comp);
            N_mag = abs(Velocity*cos(theta));
            T_mag = abs(Velocity*sin(theta));
            %Get Perimeter and Area to Obtain Volume
            IZ = zeros(h,w);
            IZ(A) = 1;
            Perimeter = Perim(IZ);
            Area = s.Area(component,1);
            %Calculate D_32
            Diam = 4*Area/Perimeter;
%               Volume = Diam^3;
%               mass = Volume*Density;
%               mv = mass*Velocity;
```

```matlab
%           MVD(end+1:end+length(mv)) = mv;
%           Mass_D(end+1:end+length(mass)) = mass;
          vstats.Vel_D{idx}(end+1:end+length(Velocity)) = Velocity;
          vstats.U_magD{idx}(end+1:end+length(U_mag)) = U_mag;
          vstats.V_magD{idx}(end+1:end+length(V_mag)) = V_mag;
          vstats.N_magD{idx}(end+1:end+length(N_mag)) = N_mag;
          vstats.T_magD{idx}(end+1:end+length(T_mag)) = T_mag;
          vstats.Diam_D{idx}(end+1:end+length(Diam)) = Diam;
        end
    end
close all
[x_lig,y_lig]=meshgrid(xx,yy);
% handle = vfield(x,y,u,v,magn);
end
dx = abs((xx(1,2)-xx(1,1))/2);
dy = abs((yy(1,2)-yy(1,1))/2);
% mm_pix = (dx+dy);
% MVD = MVD*(mm_pix^3);
% Mass_D = Mass_D*(mm_pix^3);
% sum_D = sum(MVD);
% nMVD = MVD/sum_D;
toc
%%
clearvars -except vstats xc yc k dir dx dy mm_pix Density
% clearvars -except mm_pix k dir MVD sum_D nMVD Density Vel_D Diam_D Mass_D
U_magD V_magD xc yc N_magD T_magD
dirLP=strcat(dir,num2str(k),'k_All_Lig\PTV\');
disp(strcat('calculating: ',num2str(k),'k',' Ligament Statistics'))
tic
% MVL=[];
% Vel_L = [];
% Diam_L = [];
% Mass_L = [];
% U_magL = [];
% V_magL = [];
% N_magL = [];
% T_magL = [];
for idx = 1:1500
vstats.Vel_L{idx} = [];
vstats.Diam_L{idx}= [];
vstats.U_magL{idx} = [];
vstats.V_magL{idx} = [];
vstats.N_magL{idx} = [];
vstats.T_magL{idx} = [];
    if idx < 10
       name='B0000';
    elseif idx>=10 && idx<100
       name = 'B000';
    elseif idx>=100 && idx<1000
       name = 'B00';
```

```matlab
        elseif idx>=1000
            name = 'B0';
        end
        n = [name num2str(idx)];
        file=strcat(dirLP,n,'.vc7');
        %import file structure
        inst1=readimx(file);
        %extract x,y,u,v
        [xx,yy,uinst,vinst]=showimx(inst1);
        %extract information about the map
            %find how many rows and columns there are
        [xxx,yyy]=size(xx); %xx will be columns, yy will be rows
        %find the spacing in mm in the x and y direction
        xx=xx(:,1);
        yy=yy(1,:);
        u=uinst';
        v=vinst';
        magn = sqrt(v.^2+u.^2);
        magn_loc = find(magn);
close all
[x,y]=meshgrid(xx,yy);
%%
dirL = strcat(dir,num2str(k),'k_All_Lig\');
    file=strcat(dirL,n,'.im7');
    %import file structure
    inst2=readimx(file);
    %extract x,y,u,v
    [xx,yy,uinst]=showimx(inst2);
    %extract information about the map
        %find how many rows and columns there are
    [xxx,yyy]=size(xx); %xx will be columns, yy will be rows
    Int_Map = mat2gray(255*mat2gray(uinst));
    BW = Int_Map>0;
    [h,w] = size(BW);
    CC = bwconncomp(BW);
    s = regionprops('table',BW,'Area','PixelIdxList');
    Objects = CC.NumObjects;
    for component = 1:Objects
        A = CC.PixelIdxList{1,component};
        B = magn_loc;
        C = intersect(A,B,'rows');
        num_vectors = length(C');
        if num_vectors == 0
            continue
        elseif num_vectors == 1
            %Finding N and T Components
            dx = x(C) - xc;
            dy = y(C) - yc;
            phi1 = atan(dy/dx);
            phi2 = atan(abs(u(C))/v(C));
```
108

```matlab
            theta = phi1 + phi2;
            %Grab velocity of component
            Velocity = magn(C);
            U_mag = abs(u(C));
            V_mag = abs(v(C));
            N_mag = abs(Velocity*cos(theta));
            T_mag = abs(Velocity*sin(theta));
            %Get Perimeter and Area to Obtain Volume
            IZ = zeros(h,w);
            IZ(A) = 1;
            Perimeter = Perim(IZ);
            Area = s.Area(component,1);
            %Calculate D_32
            Diam = 4*Area/Perimeter;
%           Volume = Diam^3;
%           mass = Volume*Density;
%           mv = mass*Velocity;
%           MVL(end+1:end+length(mv)) = mv;
%           Mass_L(end+1:end+length(mass)) = mass;
            vstats.Vel_L{idx}(end+1:end+length(Velocity)) = Velocity;
            vstats.U_magL{idx}(end+1:end+length(U_mag)) = U_mag;
            vstats.V_magL{idx}(end+1:end+length(V_mag)) = V_mag;
            vstats.N_magL{idx}(end+1:end+length(N_mag)) = N_mag;
            vstats.T_magL{idx}(end+1:end+length(T_mag)) = T_mag;
            vstats.Diam_L{idx}(end+1:end+length(Diam)) = Diam;
        elseif num_vectors > 1
          %Finding N and T Components
          dx = mean(x(C) - xc);
          dy = mean(y(C) - yc);
          phi1 = atan(dy/dx);
          phi2 = atan(mean(abs(u(C)))/mean(v(C)));
          theta = phi1 + phi2;
          %Grab average velocity of component
          V = magn(C);
          Velocity = mean(V);
          U_comp = abs(u(C));
          U_mag = mean(U_comp);
          V_comp = abs(v(C));
          V_mag = mean(V_comp);
          N_mag = abs(Velocity*cos(theta));
          T_mag = abs(Velocity*sin(theta));
          %Get Perimeter and Area to Obtain Volume
          IZ = zeros(h,w);
          IZ(A) = 1;
          Perimeter = Perim(IZ);
          Area = s.Area(component,1);
          %Calculate D_32
          Diam = 4*Area/Perimeter;
%           Volume = Diam^3;
%           mass = Volume*Density;
```

```matlab
%            mv = mass*Velocity;
%            MVL(end+1:end+length(mv)) = mv;
%            Mass_L(end+1:end+length(mass)) = mass;
          vstats.Vel_L{idx}(end+1:end+length(Velocity)) = Velocity;
          vstats.U_magL{idx}(end+1:end+length(U_mag)) = U_mag;
          vstats.V_magL{idx}(end+1:end+length(V_mag)) = V_mag;
          vstats.N_magL{idx}(end+1:end+length(N_mag)) = N_mag;
          vstats.T_magL{idx}(end+1:end+length(T_mag)) = T_mag;
          vstats.Diam_L{idx}(end+1:end+length(Diam)) = Diam;
        end
    end
close all
[x_lig,y_lig]=meshgrid(xx,yy);
% handle = vfield(x,y,u,v,magn);
end
dx = abs((xx(1,2)-xx(1,1))/2);
dy = abs((yy(1,2)-yy(1,1))/2);
% mm_pix = (dx+dy);
% MVL = MVL*(mm_pix^3);
% Mass_L = Mass_L*(mm_pix^3);
% max_MVL = max(MVL);
% sum_L = sum(MVL);
% nMVL = MVL/sum_L;
toc
clearvars -except vstats xc yc k dir dx dy mm_pix Density
%save workspace
disp('Saving Workspace...')
tic
outd = 'H:\HS_Data_5-19-20\8-16-17\Velocity\Workspaces\';
save(strcat(outd,num2str(k),'k_All_workspace.mat'));
toc
clearvars -except k dir
addpath('C:\Users\jewi233\Google Drive\FordProject\Scripts_Functions\')
addpath('C:\Users\jewi233\Documents\DaVis-MATLAB\')
end
```

A.2 CHAPTER TWO RELEVANT MATLAB SCRIPTS

Still_Img_Serr_Unserr_Processing.mat

```matlab
%%This script takes the serrated and unserrated still images, and binarizes
%%and determine size statistics from the ligaments and droplets in the
%%image and outputs them into excel and workspace files.
%clear workspace
close all
clear variables;
%Establish input folder
input_folder = 'F:\Near-Field\Serrated vs Unserrated\Images\';
styles{1} = cellstr('Serrated\'); styles{2} = cellstr('Unserrated\');
speed = cellstr(['20kRPM\';'35kRPM\';'50kRPM\']);
for ss = 1:2
    for s = 1:3
        if s==3
            cases = 250:250:500;
        else
            cases = 250:500:750;
        end
        img_idx = 0:1499;
        for m = 1:length(cases)
            if cases == 0
            else
            clearvars -except input_folder speed cases img_idx m s ss styles
            tic
            imgfolder =
strcat(input_folder,char(styles{ss}),speed{s},num2str(cases(m)),'CCM_200SA\');
            imgname = 'img_';
            %Establish output folder
            output_folder = strcat('F:\Near-Field\Serrated vs
Unserrated\OutputData\',char(styles{ss}),speed{s},num2str(cases(m)),'CCM_200SA\');
            LL = 0; WW = 0; PL = 0; AL = 0; PD = 0; AD = 0;
            for ii=1:length(img_idx)
                if mod(ii,10)==0
                    disp(strcat('Image Progress: ',num2str(ii),'/1500'))
                    toc
                    tic
                else
                end
                %% Read image and Establish Custom Threshold
                %Read-In Image
            I = imread(strcat(imgfolder,imgname,num2str(img_idx(ii)),'.bmp'));
                distance = 427.3; %pixels
                cal_obj = .7112; %mm from .028 in.
            pixpmm=distance/cal_obj; %defining from calibration (pixels per mm)
                %Defining image
                original_img = I;
```

111

```matlab
[h,w]=size(I);
%Image Histogram
img_hist = imhist(I)';
Fs = 1:length(img_hist);
%Find Peaks and Locations of Maxima in Histogram
[pks{ii},locs{ii}] = findpeaks(img_hist,Fs,'MinPeakDistance',20);
[max_pk,max_idx] = max(pks{ii});
%Selecting Largest Peak After Beginning
max_loc = locs{ii}(max_idx);
%Creating Thresholded Image
thresh_img = I;
thresh_img(I>max_loc)=max_loc;
% Filter, Dilate, and Binarize
%Averaging Filter
filter_size = 10;
ones_mat = ones(filter_size,filter_size)/(filter_size^2);
avg_filt_img = imfilter(thresh_img,ones_mat);
%Dilation
struct_elem = strel('square',36);
struct_elem_2 = strel('line',50,90);
dilated_img = imdilate(avg_filt_img,struct_elem);
dilated_img_2 = imdilate(dilated_img,struct_elem_2);
%Adaptive thresholding for background noise in shadowgraph
BW_adapt =
imbinarize(original_img,'adaptive','ForegroundPolarity','dark','Sensitivity',.2);
BW_adapt = imcomplement(bwareaopen(imcomplement(BW_adapt),25));
%Fill in gaps in binarized image
BW_fill = imfill(imcomplement(BW_adapt),'holes');
holes = logical(BW_fill - BW_adapt);
bigholes = bwareaopen(imcomplement(holes), 200);
BW_fill_2 = logical(BW_fill - bigholes);
%Remove small objects from image
BW_ao_img = bwareaopen(BW_fill_2,25);
% Identify Connected Components by Attachment to Cup
%Establish connected components
CC = bwconncomp(BW_ao_img);
%Get pixel IDs of components
numPixels = cellfun(@numel,CC.PixelIdxList);
%Find largets component
[biggest,idx] = max(numPixels);
%Exclude all other information besides largest component
lig_and_cup_img = false(size(BW_ao_img));
lig_and_cup_img(CC.PixelIdxList{idx}) = true;
for k = 1:h
    lig_edges(k) = find(lig_and_cup_img(k,:)==0,1,'first');
end
%          %Finding approximate cup edge
%                  orig_lig_edges = lig_edges;
%                  lig_edges(lig_edges==0) = [];
%                  xpix = 1:h;
```

```matlab
%                     xpix(lig_edges==0) = [];
%                grad_lig_edges = gradient(lig_edges);
%                  lig_edges(grad_lig_edges>0) = [];
%                  xpix(grad_lig_edges>0) = [];
%               lin_fit = polyfit(xpix,lig_edges,1);
%                   real_slope = lin_fit(1);
%                grad_lig_edges = gradient(lig_edges);
%          lig_edges(grad_lig_edges<real_slope*1.5) = [];
%             xpix(grad_lig_edges<real_slope*1.5) = [];
%          old_eqn = round(lin_fit(1)*xpix + lin_fit(2));
%                  diff_vals = lig_edges - old_eqn;
%                  lig_edges(diff_vals>0) = [];
%                  xpix(diff_vals>0) = [];
%             lin_fit_2 = polyfit(xpix,lig_edges,1);
%            if abs(lin_fit_2(1))>abs(lin_fit(1)*1.1)
%                    lin_fit_2 = lin_fit;
%                else
%                end
%                slopes(1:2,ii) = lin_fit_2;
lin_fit_2 = [-.04,312];
cup_edge_locs = round(polyval(lin_fit_2,1:h)) - 10; %8 is a manual correction
dist2edge = median(lig_edges - cup_edge_locs);
cup_edge_locs = cup_edge_locs + round(dist2edge);
BW_cup = zeros(h,w);
for d = 1:h
    BW_cup(d,1:cup_edge_locs(d)) = 1;
end
%Get image with only the ligaments,cup edge, and droplets
no_cup_img = BW_ao_img - BW_cup;
%Remove droplets from image, leaving ligaments and cup edge
lig_only_img = lig_and_cup_img - BW_cup;
lig_only_img(lig_only_img==-1)=0;
lig_only_img = logical(lig_only_img);
%The rest is just the droplets
drop_only_img = no_cup_img - lig_and_cup_img;
drop_only_img(drop_only_img==-1)=0;
drop_only_img = logical(drop_only_img);
both_no_cup_img = logical(lig_only_img + drop_only_img);
%%
%          BWM = bwmorph(both_no_cup_img,'remove');
%          IC = imcomplement(I);
%          BWC = imcomplement(BWM);
%          BWC2 = imcomplement(both_no_cup_img);
%          IEG = immultiply(IC,BWC);
%          IEG2 = immultiply(IC,BWC2);
%          EG = imcomplement(IEG);
%          EG2 = imcomplement(IEG2);
%%
% Write Processed Images to File
%      LigBMPfile = strcat(output_folder,'Ligament BMPs\img_',num2str(ii),'.bmp');
```

```matlab
%            DropBMPfile = strcat(output_folder,'Droplet BMPs\img_',num2str(ii),'.bmp');
%            BothBMPfile = strcat(output_folder,'Combined BMPs\img_',num2str(ii),'.bmp');
%            imwrite(lig_only_img,LigBMPfile);
%            imwrite(drop_only_img,DropBMPfile);
%            imwrite(both_no_cup_img,BothBMPfile);
          % Counting Ligaments
          %Identify ligament components
          CC2 = bwconncomp(lig_only_img);
          Ligaments = CC2.NumObjects;
          %Determining and Displaying Ligament Properties
          if Ligaments == 0
          elseif Ligaments > 0
            %Allocating data to struct
            L = ligLengths2(lig_only_img);
            LL(end+1:end+length(L))=L;
            stats(ii).LL = ligLengths2(lig_only_img);
            W = ligWidths(lig_only_img,cup_edge_locs);
            WW(end+1:end+length(W))=W;
            stats(ii).WW = ligWidths(lig_only_img,cup_edge_locs);
            %Establishing region properties
            sL = regionprops('table',lig_only_img,'Area','PixelIdxList');
            sD = regionprops('table',drop_only_img,'Area','PixelIdxList');
            %Finding Ligament Areas/Perimeters
            for z=1:height(sL)
              IZ = zeros(h,w);
              [AZ]=sL.PixelIdxList{z};
              IZ(AZ)=1;
              IZZ = cat(2, zeros(h,1), IZ, zeros(h,1));
              IZZ = cat(1, zeros(1,w+2), IZZ, zeros(1,w+2));
              stats(ii).PL(z)= Perim(IZZ);
              PL(end+1:end+length(Perim(IZZ))) = stats(ii).PL(z);
              stats(ii).AL(z) = sL.Area(z,1);
              AL(end+1:end+length(sL.Area(z,1))) = stats(ii).AL(z);
            end
            clearvars SL AZ IZ IZZ
            %Finding Droplet Areas/Perimeters
            for z=1:height(sD)
              IZ = zeros(h,w);
              [AZ]=sD.PixelIdxList{z};
              IZ(AZ)=1;
              IZZ = cat(2, zeros(h,1), IZ, zeros(h,1));
              IZZ = cat(1, zeros(1,w+2), IZZ, zeros(1,w+2));
              stats(ii).PD(z)= Perim(IZZ);
              PD(end+1:end+length(Perim(IZZ))) = stats(ii).PD(z);
              stats(ii).AD(z) = sD.Area(z,1);
              AD(end+1:end+length(sD.Area(z,1))) = stats(ii).AD(z);
            end
            clearvars SD AZ IZ IZZ
          end
        end
```

114

```matlab
% Output Data to Excel Files and Save Workspace Variables
struct_file = strcat(output_folder,'workspace.mat');
save(struct_file,'stats')
clearvars stats
Ligament Excel File
lig_filename = strcat(output_folder,'Ligament Data');
xlswrite(lig_filename,LL','Lengths');
xlswrite(lig_filename,WW','Widths');
xlswrite(lig_filename,PL','Perimeters');
xlswrite(lig_filename,AL','Areas');
%Droplet Excel File
PD = PD';
[prows,~] = size(PD);
pcols = round(prows/10000)+1;
PDr = vec2mat(PD,pcols);
AD = AD';
[arows,~] = size(AD);
acols = round(arows/10000)+1;
ADr = vec2mat(AD,acols);
drop_filename = strcat(output_folder,'Droplet Data');
xlswrite(drop_filename,PDr,'Perimeters');
xlswrite(drop_filename,ADr,'Areas');
toc
end
end
end
end
```

REFERENCES

1.   Khan, M. K. I.; Schutyser, M. A. I.; Schroën, K.; Boom, R. The Potential of
        Electrospraying for Hydrophobic Film Coating on Foods. *J. Food Eng.* **2012**, *108*
        (3), 410–416.

2.   Craig, I. P.; Hewitt, A.; Terry, H. Rotary Atomiser Design Requirements for
        Optimum Pesticide Application Efficiency. *Crop Prot.* **2014**, *66*, 34–39.

3.   Akafuah, N.; Poozesh, S.; Salaimeh, A.; Patrick, G.; Lawler, K.; Saito, K.
        Evolution of the Automotive Body Coating Process—A Review. *Coatings* **2016**, *6*
        (2), 24.

4.   Domnick, J., Thieme, M. Atomization Characteristics of High-Speed Rotary Bell
        Atomizers. *At. Sprays* **2006**, *16* (8), 857–874.

5.   Poozesh, S.; Akafuah, N.; Saito, K. Effects of Automotive Paint Spray Technology
        on the Paint Transfer Efficiency – a Review. *Proc. Inst. Mech. Eng. Part D J.
        Automob. Eng.* **2017**, *232* (2), 282–301.

6.   Im, K. S.; Lai, M. C.; Yi, L.; Sankagiri, N.; Loch, T.; Nivi, H. Visualization and
        Measurement of Automotive Electrostatic Rotary-Bell Paint Spray Transfer
        Processes. *J. Fluids Eng.* **2001**, *123* (2), 237–245.

7.   Bailey, A. G. Electrostatic Atomization of Liquids. *Sci. Prog. Oxford* **1974**, *61* (1),
        555–585.

8.   Balachandran, W.; Bailey, A. G. The Dispersion of Liquids Using Centrifugal and
        Electrostatic Forces. *IEEE Trans. Ind. Appl.* **1984**, *IA-20* (3), 682–686.

9.   Frost, A. R. Rotary Atomization in the Ligament Formation Mode. *J. Agric. Eng.*

Res. **1981**, *26* (1), 63–78.

10. Corbeels, P. L.; Senser, D. W.; Lefebvre, A. H. Atomization Characteristics of a Highspeed Rotary-Bell Paint Applicator. *At. Sprays* **1992**, *2* (2), 87–99.

11. Debler, W.; Yu, D. The Break-Up of Laminar Liquid Jets. *Proc. R. Soc. Lond. A. Math. Phys. Sci.* **1988**, *415* (1848), 107–119.

12. Ellwood, K. R. J. Laminar Jets of Bingham-Plastic Liquids. *J. Rheol. (N. Y. N. Y).* **1990**, *34* (6), 787.

13. Marmottant, P.; Villermaux, E. Fragmentaion of Stretched Liquid Ligaments. *Phys. Fluids* **2004**, *16* (8), 2732–2741.

14. Bizjan, B.; Širok, B.; Hočevar, M.; Orbanić, A. Liquid Ligament Formation Dynamics on a Spinning Wheel. *Chem. Eng. Sci.* **2014**, *119*, 187–198.

15. Ahmed, M.; Youssef, M. S. Characteristics of Mean Droplet Size Produced by Spinning Disk Atomizers. *J. Fluids Eng.* **2012**, *134* (7), 71103.

16. Peng, H.; Wang, N.; Wang, D.; Ling, X. Experimental Study on the Critical Characteristics of Liquid Atomization by a Spinning Disk. *Ind. Eng. Chem. Res.* **2016**, *55* (21), 6175–6185.

17. Bizjan, B.; Širok, B.; Hočevar, M.; Orbanić, A. Ligament-Type Liquid Disintegration by a Spinning Wheel. *Chem. Eng. Sci.* **2014**, *116*, 172–182.

18. Senuma, Y.; Hilborn, J. G. High Speed Imaging of Drop Formation from Low Viscosity Liquids and Polymer Melts in Spinning Disk Atomization. *Polym. Eng. Sci.* **2002**, *42* (5), 969–982.

19. Kim, T. S.; Kim, M. U. The Flow and Hydrodynamic Stability of a Liquid Film on a Rotating Disc. *Fluid Dyn. Res.* **2009**, *41* (3), 035504 (28pp).

20. Ryley, D. J. Analysis of a Polydisperse Aqueous Spray from a High-Speed Spinning Disk Atomizer. *Br. J. Appl. Phys.* **1959**, *10* (4), 180–186.

21. Ahmed, M.; Youssef, M. S. Influence of Spinning Cup and Disk Atomizer Configurations on Droplet Size and Velocity Characteristics. *Chem. Eng. Sci.* **2014**, *107*, 149–157.

22. Huang, H.; Lai, M.-C.; Meredith, W. Simulation of Spray Transport from Rotary Cup Atomizer Using KIVA-3V. In *Proceedings of ICLASS'00*; 2000; pp 1435–1437.

23. Dombrowski, N.; Lloyd, T. L. Atomisation of Liquids by Spinning Cups. *Chem. Eng. J.* **1974**, *8* (1), 63–81.

24. Ellwood, K. R. J.; Tardiff, J. L.; Alaie, S. M. A Simplified Analysis Method for Correlating Rotary Atomizer Performance on Droplet Size and Coating Appearance. *J. Coatings Technol. Res.* **2014**, *11* (3), 303–309.

25. Blaisot, J. B.; Yon, J. Droplet Size and Morphology Characterization for Dense Sprays by Image Processing: Application to the Diesel Spray. *Exp. Fluids* **2005**, *39* (6), 977–994.

26. MacIan, V.; Payri, R.; Garcia, A.; Bardi, M. Experimental Evaluation of the Best Approach for Diesel Spray Images Segmentation. *Exp. Tech.* **2012**, *36* (6), 26–34.

27. Ma, Y. J.; Huang, R. H.; Deng, P.; Huang, S. The Development and Application of an Automatic Boundary Segmentation Methodology to Evaluate the Vaporizing Characteristics of Diesel Spray under Engine-like Conditions. *Meas. Sci. Technol.* **2015**, *26* (4), 045004.

28. Cao, Z. M.; Nishino, K.; Mizuno, S.; Torii, K. PIV Measurement of Internal

Structure of Diesel Fuel Spray. *Exp. Fluids* **2000**, *29* (7), S211–S219.

29.   Hess, C. F.; L'Esperance, D. Droplet Imaging Velocimeter and Sizer: A Two-Dimensional Technique to Measure Droplet Size. *Exp. Fluids* **2009**, *47* (1), 171–182.

30.   Zhang, M.; Xu, M.; Hung, D. L. S. Simultaneous Two-Phase Flow Measurement of Spray Mixing Process by Means of High-Speed Two-Color PIV. *Meas. Sci. Technol.* **2014**, *25* (9), 095204.

31.   Stevenin, C.; Tomas, S.; Vallet, A.; Amielh, M.; Anselmet, F. Flow Characteristics of a Large-Size Pressure-Atomized Spray Using DTV. *Int. J. Multiph. Flow* **2016**, *84*, 264–278.

32.   Ryan, S. D.; Gerber, A. G.; Holloway, A. G. L.; Brunswick, N. A Computational Study of Sprays Produced by Rotary Cage Atomizers. *Trans. ASABE* **2012**, *55* (4), 1133–1148.

33.   Soumendra, B. K.; Zhou, J.; Harding, A.; Williams, C.; Moncier, J.; Baker, L.; McCreight, K. Effect of Atomization and Rheology Control Additives on Particle Size and Appearance of Automotive Coatings. In *Proceedings of the 15th International Coating Science and Technology Symposium*; St. Paul, MN, USA, 2010.

34.   Goldsworthy, L. C.; Bong, C.; Brandner, P. A. Measurements of Diesel Spray Dynamics and the Influence of Fuel Viscosity Using Piv and Shadowgraphy. *At. Sprays* **2011**, *21* (2), 167–178.

35.   Ogasawara, S.; Daikoku, M.; Shirota, M.; Inamura, T.; Saito, Y.; Yasumura, K.; Shoji, M.; Aoki, H.; Miura, T. Liquid Atomization Using a Rotary Bell Cup

Atomizer (Influence of Flow Characteristics of Liquid on Breakup Pattern)*. *J. Fluid Sci. Technol.* **2010**, *5* (3), 464–474.

36. Hatayama, Y.; Haneda, T.; Shirota, M.; Inamura, T.; Daikoku, M.; Soma, T.; Saito, Y.; Aoki, H. Formation and Breakup of Ligaments from a High Speed Rotary Bell Cup Atomizer (Part 1: Observation and Quantitative Evaluation of Formation and Breakup of Ligaments). *Trans. JAPAN Soc. Mech. Eng. Ser. B* **2013**, *79* (802), 1081–1094.

37. Majithia, A. K.; Hall, S.; Harper, L.; Bowen, P. J. Droplet Breakup Quantification and Processes in Constant and Pulsed Air Flows. In *European Conference on Liquid Atomization and Spray Systems*; 2008; pp 8–10.

38. Stevenin, C.; Béreaux, Y.; Charmeau, J.-Y.; Balcaen, J. Shaping Air Flow Characteristics of a High-Speed Rotary-Bell Sprayer for Automotive Painting Processes. *J. Fluids Eng.* **2015**, *137* (11), 111304.

39. Domnick, J.; Scheibe, A.; Ye, Q. The Simulation of Electrostatic Spray Painting Process with High-Speed Rotary Bell Atomizers. Part II: External Charging. *Part. Part. Syst. Charact.* **2007**, *23* (5), 408–416.

40. Poozesh, S. Inkjet Printing: Facing Challenges and Its New Applications in Coating Industry, University of Kentucky, 2015.

41. Gonzalez, R. C.; Woods, R. E. *Digital Image Processing*, 2nd ed.; Prentice Hall, 2002.

42. Otsu, N. A Threshold Selection Method from Gray-Level Histograms. *IEEE Trans. Syst. Man. Cybern.* **1979**, *9* (1), 62–66.

43. Rao, D. C. K.; Karmakar, S.; Basu, S. Atomization Characteristics and Instabilities

in the Combustion of Multi-Component Fuel Droplets with High Volatility Differential. *Sci. Rep.* **2017**, *7* (1).

44. Jain, M.; Prakash, R. S.; Tomar, G.; Ravikrishna, R. V. Secondary Breakup of a Drop at Moderate Weber Numbers. *Proc. R. Soc. A Math. Phys. Eng. Sci.* **2015**, *471* (2177), 20140930–20140930.

45. Zhao, H.; Liu, H. F.; Li, W. F.; Xu, J. L. Morphological Classification of Low Viscosity Drop Bag Breakup in a Continuous Air Jet Stream. *Phys. Fluids* **2010**, *22* (11).

46. Cao, X. K.; Sun, Z. G.; Li, W. F.; Liu, H. F.; Yu, Z. H. A New Breakup Regime of Liquid Drops Identified in a Continuous and Uniform Air Jet Flow. *Phys. Fluids* **2007**, *19* (5).

47. Ye, Q.; Domnick, J. Analysis of Droplet Impingement of Different Atomizers Used in Spray Coating Processes. *J. Coatings Technol. Res.* **2017**, *14* (2), 467–476.

48. Colbert, S. A. Numerical Simulations of Droplet Trajectories from an Electrostatic Rotary-Bell Atomizer, Drexel University, 2006.

49. Atkar, P. N. Constrained Controlled Coverage of Surfaces Embedded in Three Dimensions, Carnegie Melon University, 2005.

50. Domnick, J.; Yang, Z.; Ye, Q. Simulation of the Film Formation at a High-Speed Rotary Bell Atomizer Used in Automotive Spray Painting Processes. In *22nd European Conference on Liquid Atomization and Spray Systems*; Como Lake, Italy, 2008.

51. Domnick, J. Effect of Bell Geometry in High-Speed Rotary Bell Atomization. In

23rd Annual Conference on Liquid Atomization and Spray Systems; Brno, Czech Republic, 2010.

52. Sajjadi, S.; Buelna, X.; Eloranta, J. Application of Time-Resolved Shadowgraph Imaging and Computer Analysis to Study Micrometer-Scale Response of Superfluid Helium. *Rev. Sci. Instrum.* **2018**, *89* (1).

53. Settles, G. S.; Hargather, M. J. A Review of Recent Developments in Schlieren and Shadowgraph Techniques. *Measurement Science and Technology*. 2017.

54. Malone, R. M.; Flurer, R. L.; Frogget, B. C.; Sorenson, D. S.; Holmes, V. H.; Obst, A. W. Shadowgraph Illumination Techniques for Framing Cameras. In *11th IEEE International Pulsed Power Conference*; 1997; pp 454–459.

55. Meier, T.; Solares, S. D. Rhodamine-Doped Nanoporous Polymer Films as High-Performance Anti-Reflection Coatings and Optical Filters. *Nanoscale* **2016**, *8* (40), 17675–17685.

56. Jain, S.; Somasundaram, S.; Anand, T. N. C. A Fluorescent Laser-Diffuser Arrangement for Uniform Backlighting. *Meas. Sci. Technol.* **2016**, *27* (2), 025406.

57. Selanger, K. A.; Falnes, J.; Sikkeland, T. Fluorescence Lifetime Studies of Rhodamine 6G in Methanol. *J. Phys. Chem.* **1977**, *81* (20), 1960–1963.

58. Kosambi, D. D. Statistics in Function Space. *J. ofthe Indian Math. Soc.* **1943**, *7*, 76–88.

59. Narasimha, R. Kosambi and Proper Orthogonal Decomposition. *Resonance* **2011**, *16* (6), 574–581.

60. Lumley, J. L.; Yaglom, A. M.; Tatarsky, V. I. *The Structure of Inhomogeneous Turbulent Flows*; Nauka Press: Moscow, 1967.

61. Berkooz, G.; Holmes, P.; Lumley, J. J. L. J. J. L. The Proper Orthogonal Decomposition in the Analysis of Turbulent Flows. *Annu. Rev. Fluid Mech.* **1993**, *25* (1971), 539–575.

62. Holmes, P. J.; Lumley, J. L.; Berkooz, G.; Mattingly, J. C.; Wittenberg, R. W. Low-Dimensional Models of Coherent Structures in Turbulence. *Phys. Rep.* **1997**, *287* (4), 337–384.

63. Tabib, M. V.; Joshi, J. B. Analysis of Dominant Flow Structures and Their Flow Dynamics in Chemical Process Equipment Using Snapshot Proper Orthogonal Decomposition Technique. *Chem. Eng. Sci.* **2008**, *63* (14), 3695–3715.

64. Walton, S.; Hassan, O.; Morgan, K. Reduced Order Modelling for Unsteady Fluid Flow Using Proper Orthogonal Decomposition and Radial Basis Functions. *Appl. Math. Model.* **2013**, *37* (20–21), 8930–8945.

65. Kopp-Vaughan, K. M.; Renfro, M. W. Flame Shape and Spatially Resolved Rayleigh Criterion Using Proper Orthogonal Decomposition. *Int. J. Spray Combust. Dyn.* **2012**, *4* (3), 255–274.

66. Shim, Y. M.; Sharma, R. N.; Richards, P. J. Proper Orthogonal Decomposition Analysis of the Flow Field in a Plane Jet. *Exp. Therm. Fluid Sci.* **2013**, *51*, 37–55.

67. Arienti, M.; Soteriou, M. C. Time-Resolved Proper Orthogonal Decomposition of Liquid Jet Dynamics. *Phys. Fluids* **2009**, *21* (11), 1–15.

68. Charalampous, G.; Hardalupas, Y. Application of Proper Orthogonal Decomposition to the Morphological Analysis of Confined Co-Axial Jets of Immiscible Liquids with Comparable Densities. *Phys. Fluids* **2014**, *26* (11).

69. Lengani, D.; Simoni, D.; Ubaldi, M.; Zunino, P.; Bertini, F. Experimental

Investigation on the Time-Space Evolution of a Laminar Separation Bubble by Proper Orthogonal Decomposition and Dynamic Mode Decomposition. *J. Turbomach.* **2017**, *139* (3).

70. Rajasegar, R.; Mitsingas, C. M.; Mayhew, E. K.; Yoo, J.; Lee, T. Proper Orthogonal Decomposition for Analysis of Plasma-Assisted Premixed Swirl-Stabilized Flame Dynamics. *IEEE Trans. Plasma Sci.* **2016**, *44* (12), 2940–2951.

71. Duwig, C.; Ducruix, S.; Veynante, D. Studying the Stabilization Dynamics of Swirling Partially Premixed Flames by Proper Orthogonal Decomposition. *J. Eng. Gas Turbines Power* **2012**, *134* (10), 101501.

72. Kim, J.-C.; Yoo, K.-H.; Sung, H.-G. Large-Eddy Simulation and Acoustic Analysis of a Turbulent Flow Field in a Swirl-Stabilized Combustor. *J. Mech. Sci. Technol.* **2011**, *25* (10), 2703–2710.

73. Feng, L.-H.; Wang, J.-J.; Pan, C. Proper Orthogonal Decomposition Analysis of Vortex Dynamics of a Circular Cylinder under Synthetic Jet Control. *Phys. Fluids* **2011**, *23* (1), 014106.

74. Box, G. E. P.; Jenkins, G. M.; Reinsel, G. C. *Time Series Analysis: Forecasting and Control*; 2008.

Jacob Edward Wilson

Birthplace:

Louisville, KY

Education:

University of Kentucky, Lexington, KY
B.S. in Mechanical Engineering, with a Minor in Mathematics and Physics

Experience:

Graduate Teaching Assistant, University of Kentucky, August 2016 – December 2017
Graduate Research Assistant, University of Kentucky, August 2017 – May 2018

Honors and Awards:

Recipient of University of Kentucky Governor's Scholar Presidential Scholarship
Recipient of University of Kentucky College of Engineering Academic Scholarship
Recipient of UAW Ford Rouge Powerhouse Memorial Scholarship
Member of Order of the Engineer

Publications:

Conference Proceeding
Wilson, J. E.; Grib, S. W.; Renfro, M. W.; Adams, S. A.; Salaimeh, A. A. Study of
    Near-Cup Water Droplet Breakup of a Rotary Bell Atomizer Using Shadowgraph
    and High-Speed Imaging. In ILASS-Americas 29th Annual Conference on Liquid
    Atomization and Spray Systems; Atlanta, GA, 2017.

Submitted Manuscript
Wilson, J. E.; Grib, S. W.; Ahmad, A. D.; Renfro, M. W.; Adams, S. A.; Salaimeh,
    A. A. Study of Near-Cup Droplet Breakup of an Automotive Electrostatic Rotary
    Bell (ESRB) Atomizer Using High-Speed Shadowgraph Imaging. *Coatings* **2018**.

Presentations:

Wilson, J. E.; Grib, S. W.; Renfro, M. W.; Adams, S. A.; Salaimeh, A. A. Study of
    Near-Cup Water Droplet Breakup of a Rotary Bell Atomizer Using Shadowgraph
    and High-Speed Imaging. In ILASS-Americas 29th Annual Conference on Liquid
    Atomization and Spray Systems; Atlanta, GA, 2017.